DEVELOPMENT OF HIGH FILL FACTOR AND HIGH PERFORMANCE UNCOOLED INFRARED DETECTOR PIXELS

A THESIS SUBMITTED TO
THE GRADUATE SCHOOL OF NATURAL AND APPLIED SCIENCES
OF
MIDDLE EAST TECHNICAL UNIVERSITY

BY

ŞENİZ ESRA KÜÇÜK

IN PARTIAL FULFILLMENT OF THE REQUIREMENTS
FOR
THE DEGREE OF MASTER OF SCIENCE
IN
ELECTRICAL AND ELECTRONICS ENGINEERING

SEPTEMBER 2011

Approval of the thesis:

DEVELOPMENT OF HIGH FILL FACTOR UNCOOLED INFRARED DETECTOR PIXELS

submitted by **ŞENİZ ESRA KÜÇÜK** in partial fulfillment of the requirements for the degree of **Master of Science in Electrical and Electronics Engineering Department, Middle East Technical University** by,

Prof. Dr. Canan Özgen
Dean, Graduate School of **Natural and Applied Sciences** ____________

Prof. Dr. İsmet Erkmen
Head of Department, **Electrical and Electronics Engineering** ____________

Prof. Dr. Tayfun Akın
Supervisor, **Electrical and Electronics Eng. Dept., METU** ____________

Examining Committee Members:

Assoc. Prof. Dr. Haluk Külah
Electrical and Electronics Engineering Dept., METU ____________

Prof. Dr. Tayfun Akın
Electrical and Electronics Engineering Dept., METU ____________

Assist. Prof. Dr. Barış Bayram
Electrical and Electronics Engineering Dept., METU ____________

Assist. Prof. Dr. Selim Eminoğlu
Micro and Nanotechnology Dept., METU ____________

Prof. Dr. Ekmel Özbay
Electrical and Electronics Engineering Dept., Bilkent University ____________

Date: 16.09.2011

I hereby declare that all information in this document has been obtained and presented in accordance with academic rules and ethical conduct. I also declare that, as required by these rules and conduct, I have fully cited and referenced all material and results that are not original to this work.

Name, Last Name: Şeniz Esra Küçük

Signature:

ABSTRACT

DEVELOPMENT OF HIGH FILL FACTOR AND HIGH PERFORMANCE UNCOOLED INFRARED DETECTOR PIXELS

Küçük, Şeniz Esra
M. Sc., Department of Electrical and Electronics Engineering
Supervisor: Prof. Dr. Tayfun Akın

September 2011, 129 pages

This thesis presents the design, fabrication and characterization of high performance and high fill factor surface micromachined uncooled infrared resistive microbolometer detectors which can be used in large format focal plane arrays (FPAs). The detector pixels, which have a pixel pitch of 25 μm, are designed and fabricated as two-level structures using the enhanced sandwich type resistor while the active material is selected as Yttrium Barium Copper Oxide (YBCO). First level of the pixel structure is allocated for the formation of the support arms in order to obtain longer support arms hence lower thermal conductance values to get the desired high performance levels. The pixel body is built in the second level such that the fill factor and absorption of the detector is maximized. Structural and sacrificial layer thicknesses are also optimized in order to increase the absorption coefficient of the pixel in the 8-12 μm wavelength range. The thermal simulations are conducted using finite element method (FEM) by CoventorWare software. The designed pixel has a fill factor of 92 % together with the thermal conductance and thermal time constant values calculated as 16.8 nW/K and 19.3 ms in the simulations, respectively.

The pixels are fabricated at METU MEMS facilities after the design of a CMOS compatible process flow. All process steps are optimized individually to obtain the expected high performance. Characterization step of the pixels includes the

measurements of temperature coefficient of resistance (TCR), noise and thermal conductance value together with the thermal time constant. Effective TCR of the pixel is measured as -2.81 %/K for a pixel with a support arm resistance of 8 kΩ and total resistance of 55 kΩ. The corner frequency of 1/f noise in the pixel is 9.5 kHz and 1.4 kHz under 20 μA and 10 μA current bias, respectively. The total rms noise is 192 pA within 8.4 kHz bandwidth for a current bias of 20 μA. Thermal conductance, G_{th}, of the pixel is measured as 17.4 nW/K with a time constant of 17.5 ms.

The measurement results indicate that the single pixels designed and fabricated in the scope of this thesis are applicable to large format FPAs in order to obtain a high performance imager. The expected NETD values are 33 mK and 36 mK for 384x288 and 640x480 format FPAs, respectively.

Keywords: Uncooled infrared detectors, high performance microbolometer detectors, Yttrium Barium copper Oxide (YBCO) microbolometers, surface micromachining MEMS technology

ÖZ

YÜKSEK ETKİN ALANLI VE YÜKSEK PERFORMANSLI SOĞUTMASIZ KIZILÖTESİ DETEKTÖRLERİNİN GELİŞTİRİLMESİ

Küçük, Şeniz Esra
Yüksek Lisans, Elektrik ve Elektronik Mühendisliği Bölümü
Tez Yöneticisi: Prof. Dr. Tayfun Akın

Eylül 2011, 129 sayfa

Bu tezde yüksek etkin alanlı ve yüksek performanslı yüzey mikroişleme teknolojisi ile üretilen soğutmasız kızılötesi direnç tipi mikrobolometre dedektörün tasarımı, üretimi ve karakterizasyonu sunulmaktadır. Aktif malzeme YBCO olarak seçilirken, 25 µm büyüklüğündeki pikseller iyileştirilmiş direnç yapısı kullanılarak çift katlı olarak tasarlanmış ve üretilmiştir. Piksel yapısının ilk katı daha uzun destek kolları dolayısıyla daha düşük ısıl iletkenlik elde etmek amacıyla, destek kollarının şekillendirilmesi için ayrılmıştır. Piksel gövdesi, dedektörün etkin alanını ve emilimini azami seviyeye çıkarmak için ikinci katta geliştirilmiştir. Yapısal ve feda katmanları da 8-12 µm dalgaboyu aralağındaki emilimi artırmak amacıyla optimize edilmiştir. Isıl simülasyonlar, sonlu eleman metodu (FEM) kullanılarak CoventorWare yazılımında yapılmıştır. Tasarlanan piksel, % 92'lik bir etkin alana sahiptir; ayrıca ısıl iletkenliği ve ısıl zaman sabiti sırasıyla 16.8 nW/K ve 19.3 ms olarak hesaplanmıştır.

Pikseller, CMOS'a uyumlu üretim sürecinin tasarlanmasının ardından ODTU MEMS tesislerinde üretilmiştir. Tüm üretim aşamaları beklenen yüksek performansı elde edtmek amacıyla tek tek optimize edilmiştir. Piksellerin karakterizasyon aşaması direncin sıcaklıkla değişim katsayısı (TCR), pikselin gürültü seviyesi, ısıl iletkenliği ve ısıl zaman sabitinin ölçülmesini kapsamaktadır. Toplam direnci 55 kΩ ve kol

direnci 8 kΩ olan pikselin direncinin sıcaklıkla değişim katsayısı (TCR) %–2.8 olarak ölçülmüştür. Pikselin 1/f gürültüsünün sınır frekansı 20 μA ve 10 μA akım biası için sırasıyla9.5 kHz ve 1.4 kHz'dir 8.4 kHz bant genişliği ve 20 μA akım biası için toplam etkin değer 192 pA'dir. Pikselin ısıl iletkenliği 17.4 nW/K ve zaman sabiti 17.5 ms olarak ölçülmüştür.

Ölçüm sonuçları, bu tez kapsamında tasarlanan ve üretilen piksellerin büyük biçimli odak düzlem matrislerine uygulanabilir olduğunu göstermektedir. 384x288 ve 640x480 boyutundaki odak düzlem matrisleri için beklenen gürültü eşlenikli sıcaklık farkı (NETD) değerleri sırasıyla 33 mK ve 36 mK'dir.

Anahtar kelimeler: Soğutmasız kızılötesi dedektörler, yüksek performanslı mikrobolometre dedektörler, YBCO malzemeli mikrobolometreler, yüzey mikroişlemeli MEMS teknolojisi

To my parents, my brother, and sister

ACKNOWLEDGMENTS

I would like to present my deepest appreciation and special thanks to my supervisor Prof. Dr. Tayfun Akın for his invaluable guidance, endless support and help throughout this study. It is a previlige to have a chance to study with him. I am more than glad to have got his advices not only for my professional carrier but also for my personal life.

I would also like to express my special thanks to Dr. M. Yusuf Tanrıkulu first of all for sharing his extensive knowledge and experience with me, for his help and advices during the design, fabrication and characterization steps, and at last but not least for his fellowship, patience and support throughout my graduate life. I would also like to thank Eren Canga for his help in the fabrication steps and for his valuable friendship. I want to thank Selçuk Keskin for his help and friendship in the cleanroom. I would also like to thank Orhan Akar for sharing his wide experience with me in the cleanroom and immediate help on the dicing of my process wafer. I want to thank Dr. Murat Tepegöz for his help on the design step and his support on this study. I should also mention the name of Ufuk Şenveli for sharing his knowledge and experience in the first year of my graduate study and for his friendship.

I would also like to thank Burak eminoğlu for his valuable friendship together with the help on the improvement of the noise setup. I want to thank Başak Kebapçı for her friendship both inside and outside of the cleanroom. I want to thank Deniz Eroğlu for his help in the writing cycle of this thesis and his friendship.

I would also present my thanks to Ceren Tüfekçi, Mert torunbalcı, Cavid Musayev, Soner Sönmezoğlu, Osman Aydın, Erdinç Tatar, Serdar Tez, Numan Eroğlu, Alper Küçükkömürler, and Tuncer Askerli for providing a very pleasant working environment and their support in the all cycles of my study.

I want to also express my thanks to members and staff of METU RF MEMS group, METU BIO-MEMS group, and METU MEMS Research Center facilities for their help and friendship.

I would also like to express my deepest thanks to Seçil Özdemir and Esma Parasızoğlu, my sister-like friends, for their invaluable friendship and their support in every moment of my undergraduate and graduate life.

At last but not least, I would like to thank my parents, my sister, and my brother for their endless support, encouragement and patience. Their presence is the only thing that keeps me going on when the things get wrong.

TABLE OF CONTENTS

ABSTRACT .... **IV**

ÖZ .... **VI**

ACKNOWLEDGMENTS .... **IX**

TABLE OF CONTENTS .... **XI**

LIST OF FIGURES .... **XIV**

LIST OF TABLES .... **XIX**

CHAPTERS

1 INTRODUCTION 1

1.1 Infrared Radiation 2

1.2 Thermal Infrared Detectors 5

1.2.1 Thermopile Detectors 6

1.2.2 Pyroelectric Detectors 8

1.2.3 Microbolometers 9

1.2.3.1 Diode Microbolometers 10

1.2.3.2 Resistive Microbolometers 11

1.3 Figures of Merit for the Microbolometers 16

1.3.1 Temperature Coefficient of Resistance (TCR) and Effective TCR 17

1.3.2 Thermal Conductance (Gth) 18

1.3.3 Thermal Time Constant (τ) 19

1.3.4 Responsivity 19

1.3.5 Noise Equivalent Power (NEP) 21

1.3.6 Noise Equivalent Temperature Difference (NETD) 22

1.4 Microbolometers with Double Sacrificial Layers 23

1.5 Research Objectives and Organization of the Thesis 25

2 DESIGN OF THE MICROBOLOMETER PIXELS 28
2.1 Determination of the Active Material 28
2.2 Determination of the Resistor Structure 32
2.2.1 Finger Type Resistor 32
2.2.2 Sandwich Type Resistor 35
2.2.3 Enhanced Sandwich Type Resistor 37
2.3 Detector Structure 38
2.3.1 The Design of the Support Arms 38
2.3.1.1 Pixel Type 1 39
2.3.1.2 Pixel Type 2 41
2.3.2 Design of the Pixel Body 43
2.4 Absorption Calculations of the Pixels 45
2.4.1 Theory 45
2.4.2 Absorption Simulations 48
2.5 Thermal Simulations 54
2.6 Conclusion 56
3 FABRICATION PROCESSES OF THE MICROBOLOMETER PIXELS ... 57
3.1 Design of the Fabrication Process 57
3.2 Optimization of the Process Steps 67
3.2.1 Mirror Layer 68
3.2.2 First Sacrificial Layer 70
3.2.3 First Structural Layer 73
3.2.4 Formation of the Metal Layer of the Support Arms 76
3.2.5 Contact Opening for the Second Structural Layer of the Arms 82
3.2.6 Structural Layer Formation of the Support Arms 83
3.2.7 Second Sacrificial Layer 89
3.2.8 First Structural Layer of the Second Level 90
3.2.9 Formation of the Bottom Electrodes 91
3.2.10 Resistor Openings in the Second Structural Layer of the Second Level 93
3.2.11 Active Material and Top Electrode Deposition 94
3.2.12 Deposition and Patterning of Cover YBCO 95
3.2.13 Absorber Layer 96

3.2.14 Pixel Body Formation and Release of the Pixels 97
3.3 Conclusion..103
4 TEST RESULTS 104
4.1 TCR Measurements 104
4.2 Noise Measurements...107
4.3 Thermal Conductance Measurements 114
4.4 Responsivity Measurements 115
4.5 Conclusion..119
5 CONCLUSION AND FUTURE WORK 121
REFERENCES 124

APPENDIX

A. SUMMARY OF THE THERMAL SIMULATION RESULTS OF THE TYPE 1 PIXELS 129

LIST OF FIGURES

FIGURES

Figure 1.1: Electromagnetic spectrum and the sub-regions of the visible and infrared spectrum[2]. 2
Figure 1.2: The transmittance of the atmosphere and the absorbing molecules [3]. ... 3
Figure 1.3: Change of the spectral exitance of a blackbody with respect to the wavelength at different temperatures. 4
Figure 1.4: Principle of an infrared detector. 5
Figure 1.5: The structure of a thermocouple. 6
Figure 1.6: Representative view of a pyroelectric detector. 9
Figure 1.7: Representetive view of a microbolometer pixel [32]. 11
Figure 1.8: Images obtained using (a) a 25 μm 640x480 FPA by Raytheon [21], (b) a 17 μm 1024x768 FPA by DRS [22], (c) a 17 μm 1024x768 FPA by SCD [23], and (d) a 17 μm 1024x768 FPA by BAE Systems [24]. 14
Figure 1.9: Images obtained using (a) a 17 μm 1024x768 FPA by L3 [29], (b) a 17 μm 1024x768 FPA by ULIS [29]. 15
Figure 1.10: Image obtained by 384×288 detector array fabricated at METU-MEMS Center with 35 μm pixel pitch. 16
Figure 1.11: Electrical analogue circuit of a microbolometer detector. 20
Figure 1.12: SEM image and the cross sectional view of the DRS umbrella pixel structure [26] 23
Figure 1.13: SEM image of two level 25 μm microbolometer pixel fabricated by Raytheon [21]. 25
Figure 2.1: TCR vs temperature characteristics of the YBCO deposited in METU-MEMS facilities [33]. 31
Figure 2.2: The noise measurement results of the YBCO resistor fabricated in METU MEMS facilities under different bias currents [32]. 32
Figure 2.3: Cross sectional view of a planar resistor. 33

Figure 2.4: Top view of two electrodes of a finger type resistor structure. 34
Figure 2.5: Cross sectional view of a sandwich type resistor. 35
Figure 2.6: Top view of the bottom electrode and etched isolation layer. 36
Figure 2.7: Cross sectional view of an enhanced sandwich type resistor. 37
Figure 2.8: Layouts of the first levels with 0.5 µm arm width. 39
Figure 2.9: Layouts of the first levels with 0.8 µm arm width. 40
Figure 2.10: Layouts of the first levels with 1.0 µm arm width. 41
Figure 2.11: Type 2 pixels with the support arms having 0.5 µm wide metal layers. 42
Figure 2.12: Type 2 pixels with the support arms having 0.7 µm wide metal layers. 43
Figure 2.13: Implementation of all types of resistors on the support arm with the arm metal width of 0.8 µm. 44
Figure 2.14: Layouts of the first levels of the pixels with 0.5 µm arms and different anchor placements. 44
Figure 2.15: Representative perspective view of a layer stack and its corresponding CTL model. 46
Figure 2.16: The modified CTL model of the layer stack. 47
Figure 2.17: Isometric view of the pixel used in the simulations. 49
Figure 2.18: Variation of the absorption coefficient with respect to the total sacrificial layer thickness and the structural layer thickness of the second level. 51
Figure 2.19: Absorption coefficient variation with respect to the first sacrificial layer thickness. 52
Figure 2.20: Variation of the absorption coefficient with respect to the sheet resistance of the absorber layer. 53
Figure 2.21: The Variation of the absorption of the microbolometer pixel with respect to the wavelength. 54
Figure 2.22: Result of the thermal simulation. 55
Figure 2.23: The variation of the pixel temperature with time. 56
Figure 3.1: Representative 3D views of the process flow. 67
Figure 3.2: Layout of the die containing the pixels, references, test pixels and the arrays. 68

Figure 3.3: (a)Photoresisit residue between the anchor and mirror layer of the pixels, (b) Short circuit problem as a result of the photoresist residue. 69
Figure 3.4: Successful mirror formation of a single pixel. 69
Figure 3.5: SEM image of the support arms of a pixel. PI2610 is used as the sacrificial layer in this pixel, and the dots on the field are the result of surface roughness of PI2610. 71
Figure 3.6: SEM image of a pixel with the polyimide openings for the anchors. After the strip of the titanium there are some titanium particles left near the anchor openings. 73
Figure 3.7: Layouts of different anchor structures. The inner most octagon is the opening of the structural layer. 74
Figure 3.8: SEM image of a pixel with the anchor opening of the first structural layer. 75
Figure 3.9: SEM image of 2 μm structural layer opening. 75
Figure 3.10: SEM images of two unsuccessful photolithography trials for the support arm. 78
Figure 3.11: SEM image of a successful photolithography trial for the support arm.78
Figure 3.12: SEM image showing the standing wave effect on the photoresist. 79
Figure 3.13: SEM image of the metal layer of the support arms after metal RIE process. Photoresist is removed after the MRIE process. The standing wave effect causes photoresist on the edges to be etched away before the process is completed, and the edges of the arm metal get thinner. 80
Figure 3.14: SEM image after a successful photolithography for the etch of the support arm metal. 81
Figure 3.15: SEM image of metal layer of two support arms after MRIE process.... 81
Figure 3.16: SEM image of the contact openings for the anchors connecting the first and second levels. 82
Figure 3.17: SEM image of the support arm lithography using S1813 84
Figure 3.18: SEM image of a support arm with sidewalls after nitride RIE. 84

Figure 3.19: SEM image of the support arm lithography conducted by using S1805. 85
Figure 3.20: SEM image of the support arms after the PR strip trial in PRS1000. ... 86
Figure 3.21: SEM image of the support arms after holding the wafer in EKC solution for 30 minutes. 87
Figure 3.22: SEM image of an anchor and a support arm after holding the process wafer in O_2 plasma for 2 minutes and in EKC solution for 10 minutes. 88
Figure 3.23: SEM image of an anchor and a support arm after holding the process wafer in O_2 plasma for 2 minutes, and then in PRS1000 solution for 30 minutes..... 89
Figure 3.24: SEM of a polyimide opening for the anchor formation to connect the first and second levels. 90
Figure 3.25: SEM image of a contact opening for the anchor connecting the first and second levels. 91
Figure 3.26: SEM image of a bottom electrode. The step coverage inside the anchor is good enough.. 92
Figure 3.27: SEM image of a bottom electrode pair. 93
Figure 3.28: SEM image of the resistor openings above the bottom electrodes. 94
Figure 3.29: SEM image of a top electrode on the YBCO layer. 95
Figure 3.30: SEM image of a pixel after YBCO etch. 96
Figure 3.31: SEM image of a pixel after the patterning of the absorber layer. 97
Figure 3.32: SEM image of a pixel buckled after the suspension. 98
Figure 3.33: SEM image of a pixel with the sidewalls remaining between the support arms and the pixel body. 99
Figure 3.34: SEM image of a pixel suspended after the strip of YBCO layer. 100
Figure 3.35: SEM image of a successfully suspended pixel. 101
Figure 3.36: SEM images of successfully suspended pixels in array forms. 102
Figure 3.37: SEM image of a pixel with 17 μm pitch. 103
Figure 4.1 106
Figure 4.2: Measurement results of the effective TCR value of the pixel with respect to the temperature. 106

Figure 4.4: Measurement results of the noise spectral densities of the resistors fabricated at METU MEMS Center with different resistor opening areas. 108
Figure 4.5: Schematic view of the noise measurement setup................................... 110
Figure 4.6: Noise power spectral densities of 55 kΩ resistors under 10 μA, 20 μA, and 30 μA bias currents and the corresponding corner frequencies. 113
Figure 4.7: Measurement setup used in the responsivity measurements................. 116
Figure 4.8: Measured transmission of the Si wafer used in the responsivity measurements. 116
Figure 4.9: Measured responsivity values together with the fitted responsivity curve 118

LIST OF TABLES

TABLES

Table 2.1. Width of the metal and nitride layers of the support arms for Pixel Type 2. 42
Table 2.2: Optical constants used in the simulations. 50
Table 2.3: The thermal properties of the layers used in the simulations. 55
Table 3.1. Summary of the thickness optimization trials conducted using PI2610 and PI2556. 71
Table 3.2: Thermal conductance values of the structural and active materials together with the metal layer of the support arms 76
Table 3.3: Thermal conductance values of some of the metals. 77
Table 4.1: Summary of the noise measurement results of the resistors having different resistor opening areas. 109
Table 4.2: Summary of the noise measurement results of single pixels with enhanced sandwich type resistors. 113
Table 4.3. The spesifications of the pixel used in the thermal conductance measurements. 115
Table 4.4: The comparison of the simulation and measurement results for the thermal conductance and the thermal time constant of the pixel. 118
Table 4.5: Summary of the performance parameters of fabricated pixel and expected NETD values 120

CHAPTER 1

INTRODUCTION

All objects above 0 K emit infrared radiation depending on their temperature. Thermal imaging is based on this fact in order to image the objects from a scene even under low or no daylight conditions. Infrared detectors, which use the thermal imaging to detect the objects, are composed of one or two dimensional arrays of single pixels. These arrays are also called focal plane arrays (FPAs). FPAs consist of two parts: infrared detectors and readout circuitry. Infrared detectors produce an electrical signal as a result of the incident infrared radiation emitted from an object. Readout circuitry processes this electrical signal and converts it to an image. Infrared detectors are commonly used in military applications (like targeting missions, surveillance); and in civilian applications (like firefighting viewers, preventive maintenance) [1]. The need for high resolution in both military and civilian applications requires larger format FPAs, therefore, smaller pixel sizes. Hence, the main concern in the research on the infrared imaging is to produce smaller detector pixels while maintaining high sensitivity. This thesis reports the development of a single microbolometer pixel with a 25 μm pitch.

The following sections give information about the infrared radiation, commonly used infrared detectors, and the figures of merits for microbolometers. Section 1.1 makes an overview on the infrared radiation, while Section 1.2 explains the thermal detector types and their detection mechanisms. Section 1.3 discusses the figures of merit for microbolometers, and Section 1.4 gives information about the microbolometers with double sacrificial layers. Finally, Section 1.5 summarizes the research objectives and thesis organization.

1.1 Infrared Radiation

The infrared spectrum is the part of electromagnetic spectrum spanning in the wavelength range of 0.75-1000 μm. This spectrum is divided into sub-regions. Figure 1.1 shows the electromagnetic spectrum and infrared spectrum with its sub-regions [2].

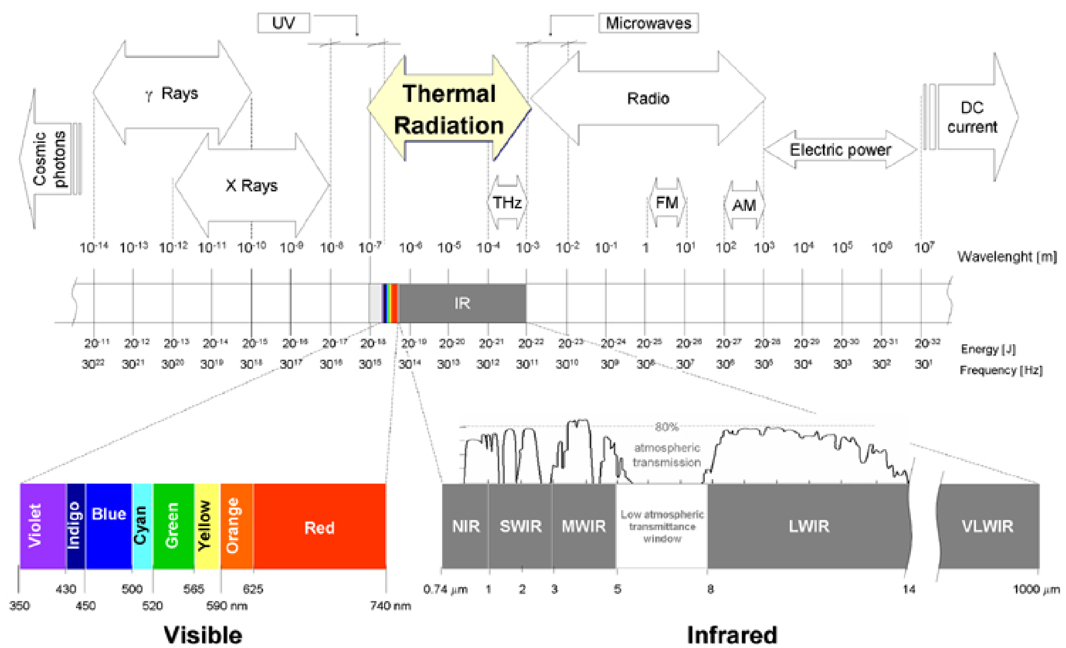

Figure 1.1: Electromagnetic spectrum and the sub-regions of the visible and infrared spectrum[2].

The atmosphere attenuates the radiation due to absorption by the atmospheric gases and scattering by the particles. Therefore, an infrared detector needs to be able to sense in the transparent region of the atmosphere. Figure 1.2 shows the transmittance of the atmosphere with respect to the wavelength with the absorbing molecules [3]. It is observed that there are some atmospheric windows where the

infrared imaging is possible due to the transparency in the atmosphere. 3-5 µm and 8-12 µm bands are generally used for the infrared detection.

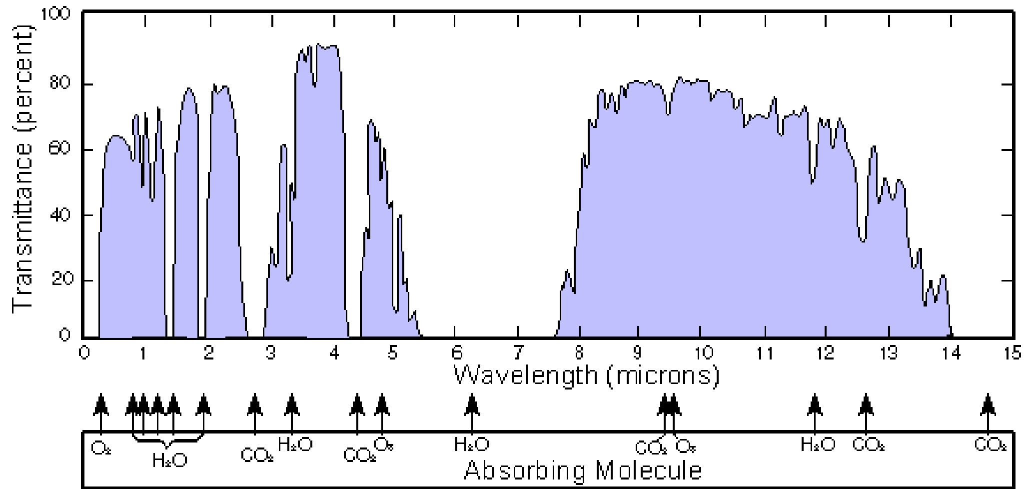

Figure 1.2: The transmittance of the atmosphere and the absorbing molecules [3].

The choice of the spectral band to be detected can be determined by considering the temperature range of the target. A blackbody, which is an ideal radiation source, has the maximum spectral exitance at a specific temperature for a given wavelength. The relation between the temperature and the spectral exitance of a blackbody can be extracted from Planck's radiation formula as follows [4]:

$$M(\lambda, T) = \frac{2\pi hc^2}{\lambda^5 (e^{hc/\lambda kT} - 1)} \tag{1.1}$$

where M is the spectral radiant exitance, h is the Planck's constant, c is the speed of the light, λ is the wavelength, k is the Boltzmann's constant, and T is the temperature of the blackbody. The wavelength where the peak exitance of a blackbody for a given temperature occurs can be calculated by taking the derivative of Equation (1.1) and finding the wavelength where the derivative is equal to zero. Wien's displacement law expresses the wavelength where the maximum exitance occurs:

$$\lambda_{max} = \frac{2898}{T} \tag{1.2}$$

where λ_{max} is the wavelength of the maximum exitance in μm and T is the temperature of the object in K. Figure 1.3 shows the change of the spectral exitance of a blackbody with respect to the wavelength at different temperatures. As indicated in the figure, the maximum exitance for the objects in room temperature, 300 K, occurs around 10 μm. Therefore, these objects are sensed by the detectors operating at 8-12 μm range. Objects with higher temperatures such as airplanes can be sensed in 3-5 μm range and the detectors to sense these objects are designed in such a manner.

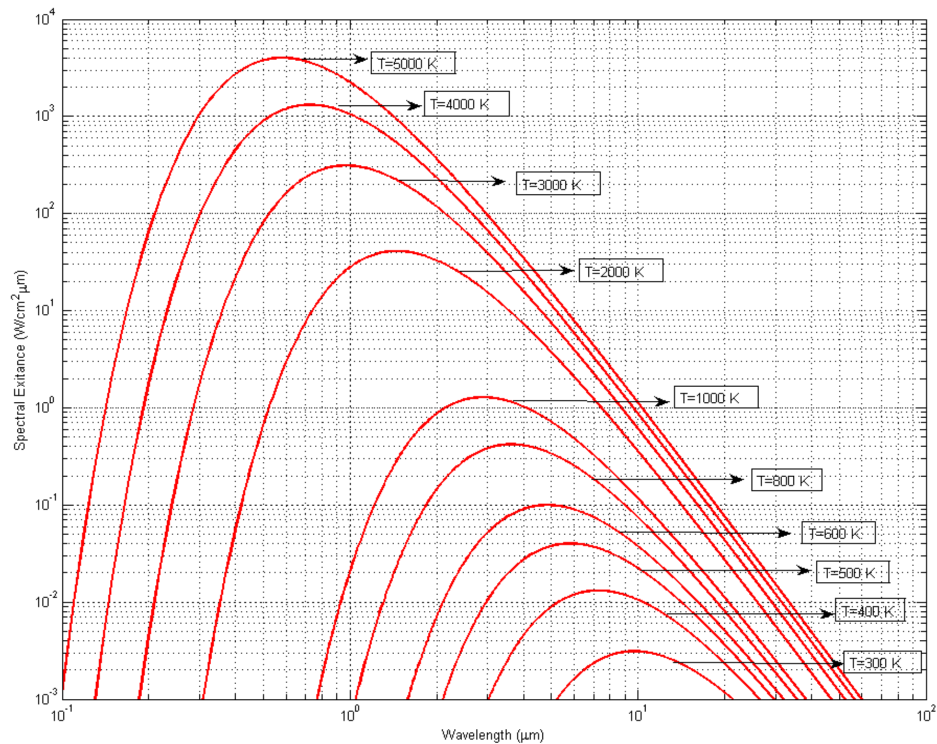

Figure 1.3: Change of the spectral exitance of a blackbody with respect to the wavelength at different temperatures.

1.2 Thermal Infrared Detectors

There are two main detection mechanisms used in infrared imaging: photon and thermal detection. Photon detection occurs when an incident photon, absorbed by a detecting material, interacts with electrons in the material [5]. This interaction gives rise to the intrinsic or extrinsic excitation. Semiconductors are generally used as the detecting material and the photon energy must exceed the bandgap energy of this material. The number of thermally excited carriers, which depends on the temperature, must be kept low in order to detect relatively small number of incident photons. Therefore, the photon detectors are needed to be cooled down to the cryogenic temperatures.

Thermal detectors detect the absorbed infrared radiation as a change in a specific property of the active material. Figure 1.4 shows the principle of a thermal detector. The pixel body is exposed to the infrared radiation. This radiation causes a rise in the initial temperature T of the detector to $T + \Delta T$. The temperature difference changes an electrical property of the active detector material such as the resistance of the detector, so that the incident radiation is detected by the readout circuitry. The detector is connected to a substrate that also behaves like a heat sink with the supporting arms having an acceptable thermal conductance, G_{th}, value.

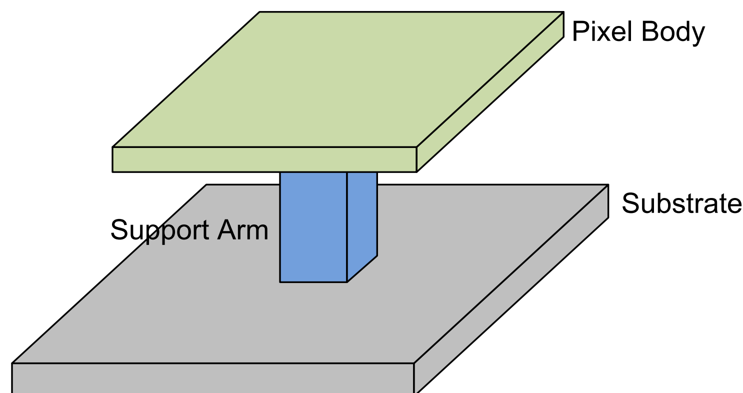

Figure 1.4: Principle of an infrared detector.

There are three kinds of commonly used thermal infrared detectors: thermopile detectors, pyroelectric detectors and microbolometer detectors. These detectors and the detection mechanisms are explained in the following subsections.

1.2.1 Thermopile Detectors

Thomas Johann Seebeck began to examine the junction behavior of electrically conductive material in the 19th century. He discovered that a small current will flow in a closed circuit of two dissimilar metallic conductors when their junctions are kept at different temperatures. Therefore, an open circuit voltage occurs if one junction is in the electric circuit is opened [6]. This phenomenon is called the Seebeck effect and thermopile detectors use this effect for infrared detection.

Figure 1.5 shows an example of such an open circuit structure, also called thermocouple structure. The incident light on the structure heats up the absorption region resulting in a temperature gradient which is converted into an output voltage. This voltage is produced on the open end of the thermocouple between *lead a* and *lead b*.

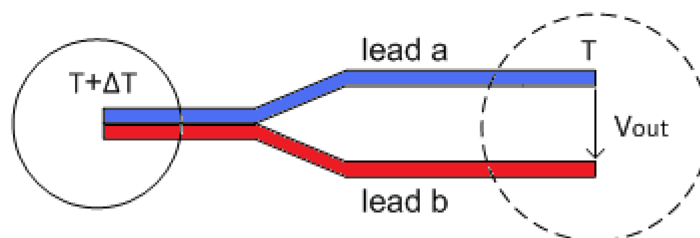

Figure 1.5: The structure of a thermocouple.

A proportionality factor α, Seebeck coefficient, is introduced to represent this relation analytically. It is a temperature and material dependent constant relating the

thermoelectric voltage generated by the thermocouple and the temperature difference as follows:

$$V_{out} = (\alpha_a - \alpha_b)\Delta T \quad (1.3)$$

where V_{out} is induced voltage at the output end, α_a and α_b are Seebeck coefficients of the materials a and b respectively, and ΔT is the temperature difference between the hot and cold junctions of the thermocouple.

The output voltage generated at the end of the thermocouple is relatively small preventing the detection of very small temperature differences. Therefore, thermocouples are connected in series to generate higher output voltages. This serially connected thermocouples form thermopiles. The output voltage of a thermopile increases linearly with the number of thermocouples serially connected, N:

$$V_{out} = N(\alpha_a - \alpha_b)\Delta T \quad (1.4)$$

Thermopile detectors require no electrical bias and have negligible 1/f noise. They are highly linear and do not need optical chopper making the system smaller. They can operate over a wide temperature range with little or no thermal stabilization requirement. The broad-operating temperature range and the lack of the need of thermal stabilization make thermopiles good candidates for some space-based imaging applications [7, 8]. As a result of their self-generating characteristics, thermopile detectors have better drift and offset behavior compared to other thermal detectors. Therefore, thermopiles are chosen in applications with almost static radiation or temperature signal such as temperature, gas or biochemical sensors [9].

Thermopile detectors have lower responsivity values than pyroelectric or microbolometer type detectors. Besides, they do not have high resolution since their pitch sizes are not small enough and the installation of thermopiles is limited [10].

These disadvantages prevent the usage of thermopile detectors in high resolution infrared imaging systems.

1.2.2 Pyroelectric Detectors

Pyroelectricity is the generation of an electric dipole moment in an insulator due to a change in temperature. The usage of the pyroelectric effect for radiation detection was first suggested by Yeou Ta in 1938.

When a pyroelectric material experiences a temperature change, dipoles in the material orient themselves in one direction and generate a net polarization. The polarization vector is proportional to the charge per unit volume. These charges arise at the surface of the pyroelectric material. The change in the charge per unit time generates a current. Therefore, a pyroelectric material generates a current whenever it experiences a temperature change and this current can be expressed as [10]:

$$i_P = pA_d \frac{dT}{dt} \tag{1.5}$$

where i_P is the pyroelectric current, p is the change in electric polarization per change in temperature, also called pyroelectric coefficient, A_d is the sensitive area of the detector and T is the temperature. If the temperature is constant, the detector current is equal to zero. Therefore, a chopper is used to modulate the incident radiation for imaging static scenes or temperatures [11]. The radiation is modulated with a constant angular frequency $= 2\pi f$. The pyroelectric detectors are high frequency thermal detectors since the maximum response is attained at a time shorter than the thermal relaxation time [12]. Figure 1.6 shows the representative view of a pyroelectric detector. It can be seen that the pyroelectric detectors act as a capacitor under a change in the temperature.

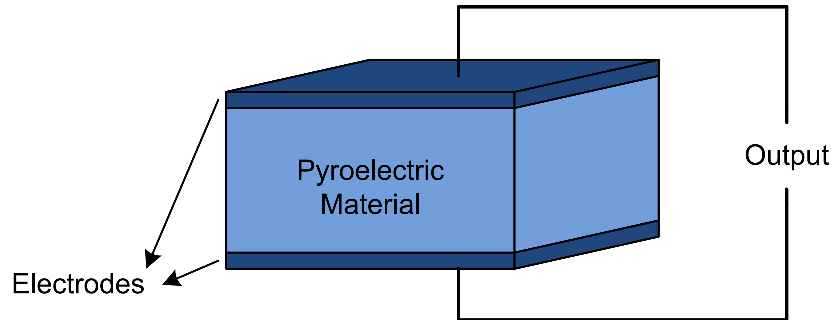

Figure 1.6: Representative view of a pyroelectric detector.

The pyroelectric coefficient generally increases with the temperature. However, it abruptly drops to zero when a specific temperature, called the *Curie temperature,* is reached. Thus, the pyroelectric detectors must be operated below this temperature to have an acceptable responsivity value.

The main advantage of the pyroelectric detectors is their uniform wavelength response. They do not need cooling or an external bias. However, a chopper is needed to obtain static images or temperatures, which makes them difficult to use in moving platforms. Pyroelectric detectors are piezoelectric, making them act as microphones. Thus, they must be isolated from the acoustic environment of the surrounding [13]. Further, these detectors must be operated under the Curie temperature to obtain reasonable responsivities.

1.2.3 Microbolometers

Microbolometers detect the incident infrared radiation as a change in the electrical property of an active material. The infrared radiation is usually absorbed by an absorber layer. This radiation causes a rise in the temperature of the detector. As a result of this temperature rise, the detector generates an electrical output in terms of voltage or current depending on the biasing. This electrical output is processed to form an image by the readout circuit. There are mainly two types of

microbolometers: diode microbolometers and resistive microbolometers. The following subsections contain an overview of these microbolometer types individually.

1.2.3.1 Diode Microbolometers

As is evident from its name, diode microbolometer uses diodes as the sensing element to the infrared radiation. It uses the temperature dependence of the forward voltage or current of the diodes. These types of detectors are biased with either constant voltage or constant current to observe the change in forward current or voltage respectively.

METU MEMS Center has developed detectors with suspended p+-active/n-well diodes in the array sizes of 64×64 and 128×128 [14-16]. The most prominent advantage of these diode microbolometers is manufacturability of the detector array and CMOS readout circuit together in a standard CMOS process. In addition, only some simple post-CMOS process steps are needed for the diode microbolometers designed at METU-MEMS Center. This feature results in reducing the detector cost to nearly that of CMOS chip [14]. The drawback of these detectors is the low sensitivity with low fill factor and relatively high time constant.

Another approach proposed by Mitsubishi is to fabricate the detector array with SOI (silicon-on-insulator) diode detectors [17]. These SOI diode detectors have infrared radiation absorbing structures which increase the fill factor, hence the absorbed infrared radiation. Therefore, the sensitivity of these detectors is higher. However, they require dedicated post-CMOS process steps. Mitsubishi reported 640×480 and 320×240 detector arrays with 25 μm and 17 μm pixel pitch values [18, 19].

1.2.3.2 Resistive Microbolometers

Resistive microbolometers use the temperature coefficient of resistance (TCR) of the active material used in the detectors as the sensing mechanism. TCR of a material is defined as:

$$\alpha = \frac{1}{R}\frac{dR}{dT} \tag{1.6}$$

where α is the temperature coefficient of resistance, R is the total resistance of the material and T is the temperature. Figure 1.7 shows the representative view of a microbolometer pixel [32]. The incident infrared radiation is absorbed by the absorber layer on the pixel and this gives rise to an increase in the temperature of the pixel. The resistance of the active material changes depending on the TCR of this material. This resistance change is converted into an electrical signal by the readout circuit. The sensitivity of the pixel depends on the TCR and noise level of the active material. Therefore, the choice of a suitable active material for a microbolometer pixel is crucial.

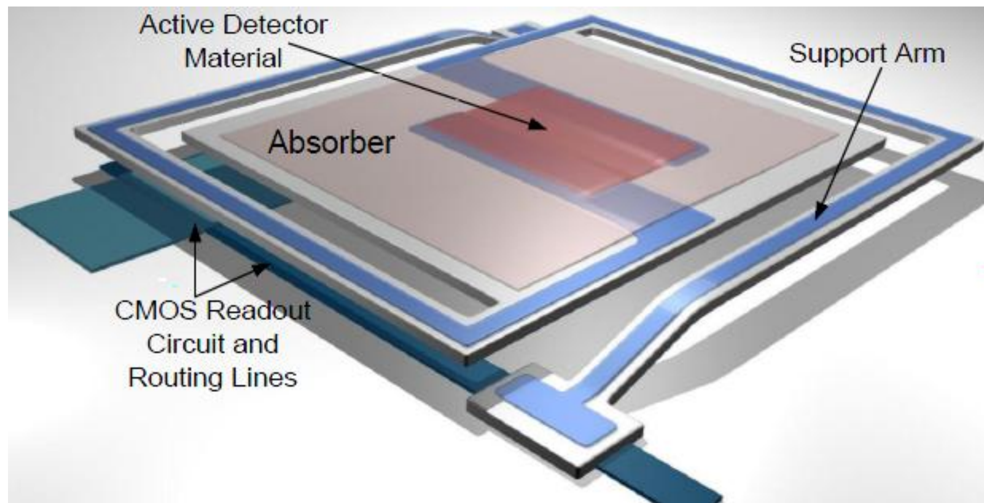

Figure 1.7: Representetive view of a microbolometer pixel [32].

VO_x is the most commonly used material for the resistive type microbolometers. It has a TCR value of 2-3%/K in magnitude. This material was patented by Honeywell Research Labs [20]. Today, many companies such as Raytheon, DRS, SCD, and BAE Systems fabricate focal plane arrays (FPAs) using VO_x as the active material. These companies reported 384×288, 640×480, and 640×512 format FPAs with 17 μm pixel pitch [21-24]. Furthermore, 1024×768 and 2048×1536 format FPAs with 17 μm and even smaller pixel pitch sizes are under development [25-27]. Figure 1.8 shows the images obtained by the IRFPAs of these companies.

(a)

(b)

(c)

(d)

Figure 1.8: Images obtained using (a) a 25 µm 640x480 FPA by Raytheon [21], (b) a 17 µm 1024x768 FPA by DRS [22], (c) a 17 µm 1024x768 FPA by SCD [23], and (d) a 17 µm 1024x768 FPA by BAE Systems [24].

Another important active material for the microbolometer pixels is amorphous silicon, a-Si. a-Si has a TCR value around 2-3%/K and it is a CMOS compatible material. ULIS and L3 are the most important companies fabricating a-Si based infrared detectors. 640×480 and 1024×768 format FPAs with 17 µm pixel pitch were reported [28, 29]. Figure 1.9 shows the images obtained the IRFPAs of these companies.

(a)

(b)

Figure 1.9: Images obtained using (a) a 17 μm 1024x768 FPA by L3 [29], (b) a 17 μm 1024x768 FPA by ULIS [29].

Yttrium Barium Copper Oxide (YBCO) is another significant active material having a TCR value of 3-4%/K, in magnitude. The studies on this material were reported by Mitsubishi and University of Texas at Arlington [30, 31]. YBCO has also been used as the active material for the microbolometers at METU MEMS Center [32-34]. 320×240 and 384×288 detector arrays with 50 μm and 35 μm pixel pitch were reported [32, 34]. Figure 1.10 shows an image obtained by 384×288 detector array fabricated at METU-MEMS Center with 35 μm pixel pitch

Figure 1.10: Image obtained by 384×288 detector array fabricated at METU-MEMS Center with 35 μm pixel pitch.

1.3 Figures of Merit for the Microbolometers

This section summarizes the figures of merit for the microbolometers that describe the performance of the microbolometer focal plane arrays.

1.3.1 Temperature Coefficient of Resistance (TCR) and Effective TCR

Temperature coefficient of resistance (TCR) of a material, denoted by α, is the normalized change in the resistance per degree of the change in the temperature. It is given as:

$$\alpha = \frac{1}{R}\frac{dR}{dT} \tag{1.7}$$

where R is the total resistance of the material and T is the temperature. In microbolometers, total resistance R_t is given as:

$$R_t = R_{det} + R_{arms} \tag{1.8}$$

where $R_{det}$is the resistance of the detector which is equal to the resistance of the active material and R_{arms} is the total resistance of the support arms. Therefore, the effective TCR α_{eff} can be expressed as, assuming that the TCR of the support arm material is equal to zero:

$$\alpha_{eff} = \frac{1}{R_{det} + R_{arms}}\frac{dR_{det}}{dT} \tag{1.9}$$

or

$$\alpha_{eff} = \frac{R_{det}}{R_{det} + R_{arms}}\alpha \tag{1.10}$$

Effective TCR can be assumed to be equal to the TCR of the material, α , provided that $R_{det} \gg R_{arms}$. However, the effective TCR decreases by the ratio of R_{det} to R_t for the detectors with very thin and long support arms.

1.3.2 Thermal Conductance (Gth)

The most important structural parameter that affects the performance of the microbolometers is the thermal conductance of the detector. Thermal conductance plays a significant role on the thermal isolation of the detectors from the substrate. Heat loss decreases with decreasing thermal conductivity, resulting in an improvement on the performance of the detector.

The thermal conductance of the detector consists of three different components: Thermal conductance of the support arm, radiative thermal conductance, and thermal conductance of the gas environment.

Total thermal conductance of two support arms of the detector is expressed as:

$$G_{arms} = 2\sum_{k}^{n} \sigma_k \frac{A_k}{l} \tag{1.11}$$

where σ_k is the thermal conductivity of the kth material of the support arms, A_k is the cross sectional area of the arms, and l is the length of the support arm.

The radiative thermal conductance is given as [35]:

$$G_{rad} = 4A_D\eta\sigma T^3 \tag{1.12}$$

where A_D is the active detector area, η is the absorptance of the detector, σ is the Stefan's constant, and T is the temperature of the detector.

Radiative thermal conductance is usually much smaller than the thermal conductance of the support arms. Therefore, it can be neglected. In addition, microbolometers operate under vacuum conditions making the thermal conductance of the gas environment surrounding the detector negligible. As a result, only the thermal conductance of the support arms is taken into account for the performance calculations of the detectors.

1.3.3 Thermal Time Constant (τ)

Thermal time constant τ, also called thermal response time, is the time required for the temperature of a detector pixel to decrease to $1/e$ of its initial value when the incident thermal radiation is instantaneously removed. Thermal time constant is defined as:

$$\tau = \frac{C_{th}}{G_{th}} \quad (1.13)$$

where C_{th} is the heat capacity of the pixel (J/K), and G_{th} is the thermal conductance of the support arms (W/K). Thermal conductance of the pixel must be as small as possible to improve the thermal isolation of the detector. On the other hand, the time constant of the detector is in tendency to increase proportionally with the decrease in the thermal conductance of the detector. The rule of thumb for the adjustment of the time constant of the detector is,

$$\tau < \frac{1}{2 \times frame\ rate} \quad (1.14)$$

where the frame rate is commonly given as 30 fps for standard applications [36]. Therefore, the time constant should not exceed 16 msec.

1.3.4 Responsivity

The responsivity $\Re$ is the ratio of the output signal of the detector to the incident radiant power falling on it. If the output signal is voltage, voltage responsvity $\Re_V$ is defined as:

$$\Re_V = \frac{V_s}{P_{inc}} \tag{1.15}$$

where V_s is the voltage signal expressing the change in the output in terms of Volts and P_{inc} is the incident radiant power falling on the detector (Watts). If the output signal is current, then current responsivity $\Re_I$ becomes:

$$\Re_I = \frac{I_s}{P_{inc}} \tag{1.16}$$

where I_s is the current signal expressing the change in the output in terms of Ampers.

Figure 1.11 shows the electrical analogue circuit of a microbolometer detector with the previously explained thermal components, thermal conductance G_{th} and thermal capacitance C_{th}. P_0 is the incident infrared power modulated with a modulation frequency of ω and η is the absorptance of the microbolometer detector which will be explained in detail in Chapter 2.

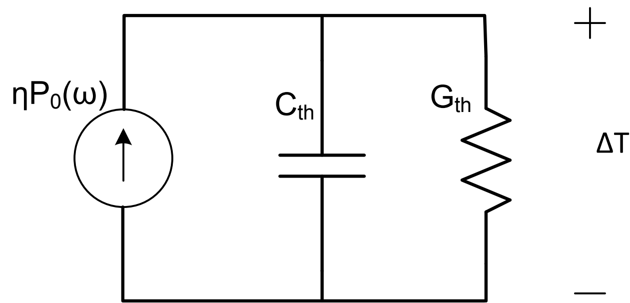

Figure 1.11: Electrical analogue circuit of a microbolometer detector.

Using the circuit in Figure 1.11 the temperature chance ΔT of the detector is given as:

$$\Delta T = \frac{\eta P_0}{G_{th}\sqrt{1 + (\omega\tau)^2}} \tag{1.17}$$

where τ is the thermal time constant of the detector.

If the detector is biased with voltage, the output is expressed as a current and the current responsivity ($\Re_I$) is defined as:

$$\Re_I = \frac{\eta\alpha V_d}{R_d G_{th}\sqrt{1 + (\omega\tau)^2}} \tag{1.18}$$

where α is the TCR of the detector, V_d is the bias voltage, and R_d is the resistance of the detector. Similarly, if the detector is biased with current, output is expressed as a voltage. The voltage responsivity ($\Re_V$) is given as:

$$\Re_V = \frac{\eta\alpha R_d I_d}{G_{th}\sqrt{1 + (\omega\tau)^2}} \tag{1.19}$$

where I_d is the bias current of the detector.

As is evident from Equations 1.18 and 1.19, responsivity can be improved by increasing the absorptance of the detector and TCR of the active material while decreasing the thermal conductance.

1.3.5 Noise Equivalent Power (NEP)

The noise equivalent power (NEP) is the incident infrared power on the detector that gives rise to the output of the detector equal to the rms value of the detector noise within the system bandwidth [33]. The NEP is expressed in Watts and defined as:

$$\text{NEP} = \frac{V_n}{\Re_V} \tag{1.20}$$

where V_n is the total rms noise of the detector within the system bandwidth and $\Re_V$ is the voltage responsivity. Since the active materials of the microbolometers are generally amorphous materials, 1/f noise is the dominant noise source. For the calculation of the total noise of the detector 1/f noise and thermal noise must be taken into account.

1.3.6 Noise Equivalent Temperature Difference (NETD)

Noise equivalent temperature difference (NETD) is the temperature change in the target scene that generates an output signal equal to the total rms noise value of the detector system [5]. It has the unit of K and defined as:

$$\text{NETD} = \frac{[4(f/\#)^2 + 1]V_n}{\Re_V \tau_0 A_D (\Delta P/\Delta T)_{\lambda_1 - \lambda_2}} \tag{1.21}$$

where $f/\#$ is the f-number of the optics, V_n is the total rms noise voltage of the system, $\Re_V$ is the voltage responsivity of the detector, τ_0 is the transmittance of the detector optics, A_D is the active detector area, and $(\Delta P/\Delta T)_{\lambda_1 - \lambda_2}$ is the change of power per unit area radiated in the $\lambda_1 - \lambda_2$ spectral range by a blackbody at temperature T.

NETD is the most important performance parameter of a microbolometer pixel. NETD must be as small as possible to be able to detect small temperature differences. This can be ensured by decreasing the noise level of the system and increasing the responsivity and active absorbing area of the detector.

1.4 Microbolometers with Double Sacrificial Layers

The need of high resolution may come up for both military and civilian applications. Therefore, decreasing the pixel size is important to increase the FPA format while maintaining enough active detection area. The primary goals while designing small-size pixels are to decrease the thermal conductance of the pixel and to maintain a high fill factor. The decrease in the absorption coefficient of the pixel or increase in the thermal conductance is inevitable for smaller pixel sizes such as 25 or 17 µm when the pixel is designed in one level. One approach to optimize both the thermal conductance and the fill factor is to fabricate a multilevel pixel, which is first proposed in [37].

There are mainly two different approaches in the design of the microbolometer pixels with double sacrificial layers, i.e. in two levels. The first approach is to form the pixel body and arms in the first level and an umbrella structure in the second level to increase the absorption [38]. This approach is patented by DRS and used in the 25 and 17 µm pixels of DRS [26]. Figure 1.12 shows an SEM image and the cross sectional view of the umbrella pixel structure [26].

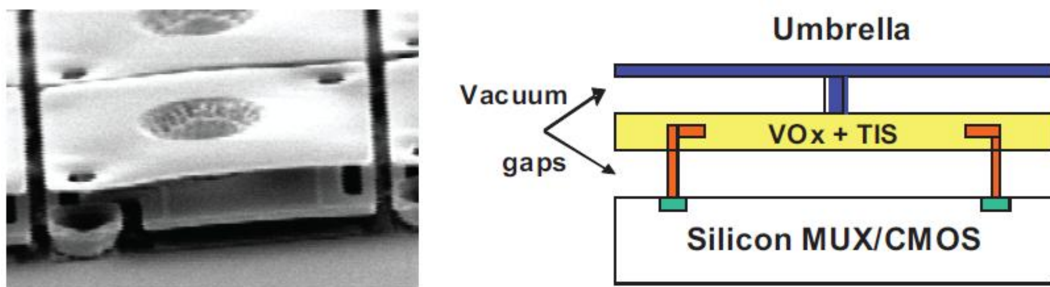

Figure 1.12: SEM image and the cross sectional view of the DRS umbrella pixel structure [26].

The first level is connected to the CMOS substrate via the anchors. The support arms connected to these anchors provide the thermal isolation. The pixel body carrying

the active detector material is in the middle of the first level. The second level is composed of an umbrella structure covering almost the entire pixel pitch, and this structure ensures the maximization of the absorption. In this approach, the support arms and the pixel body must be fit into only one level. Therefore, a material with a low thermal conductivity and low resistivity must be used to guarantee an acceptable thermal and electrical performance. Another method to provide the desired values for the thermal conductance is to decrease the width of the support arms as low as possible. The pixels with metal layers such as titanium and nichrome that are used in METU MEMS research group for both thermal isolation and the contact to the CMOS circuitry do not ensure very low thermal conductance values when the support arms are not long enough. Besides, the optimized minimum feature size at METU MEMS facility is 0.5 μm which is not small enough to establish the pixel body and support arms in single level while maintaining the desired thermal conductance values. As a result, this approach is not usable in the METU MEMS facilities without an extensive research on a new material to be used in the support arms for the thermal isolation and electrical conduction.

Another approach in the multilevel pixel design is to form the support arms in the first level and the pixel body with the resistor structure on the second level. Raytheon is one of the companies using this approach in the small pixel fabrication [39]. Figure 1.13 shows an SEM image of a two level 25 μm microbolometer pixel fabricated by Raytheon [21]. The advantage of this approach is the design convenience for the support arms. The whole pixel area is allocated for the support arm formation in the first level. Therefore, thermal conductance can be reduced to the required level. However, the absorption coefficient of this structure is less than the umbrella structure.

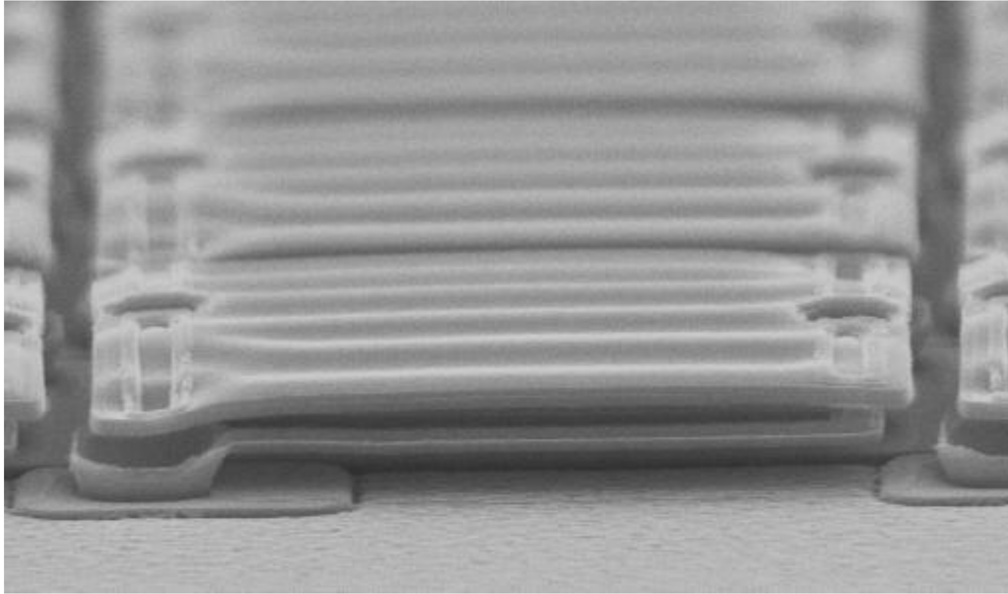

Figure 1.13: SEM image of two level 25 μm microbolometer pixel fabricated by Raytheon [21].

In the scope of this thesis, two level 25 μm microbolometer pixels were designed applying the second approach considering the adjustment easiness of the thermal conductance values. The design procedure will be explained in Chapter 2 in detail.

1.5 Research Objectives and Organization of the Thesis

The goal of this thesis is to design and fabricate double sacrificial layer microbolometer pixels with 25 μm pixel pitch size. The pixels must be fabricated using CMOS compatible process steps in order to be able to fabricate them on the readout circuits. The specific objectives of this thesis work can be listed as follows:

1. Design and optimization of double sacrificial layer microbolometer pixels with high performance. The active material is needed to be determined with relatively high TCR and low noise levels. The resistor structure must be chosen to fulfill the resistance value requirement of the readout circuit. The

main design consideration is the G_{th} value of the detector pixels to obtain the desired high performance while keeping the time constant at an acceptable range.

2. Modeling of the pixels to obtain the fabrication parameters. Absorption simulations must be carried out to calculate the sacrificial and structural layer thicknesses for a high absorption coefficient value. Thermal simulations are crucial to obtain the optimum thermal conductance and time constant values.

3. Development of a fabrication process. The process steps must be CMOS compatible. Each process step must be optimized individually such that none of them affects the other process steps. The applicability of the process steps at METU MEMS facilities is vital to fabricate the pixels as they designed.

The organization of the thesis can be summarized as follows:

Chapter 2 discusses the design consideration of the double sacrificial layer microbolometer pixels. This chapter starts with the determination of the active material and the resistor structure to fulfill the TCR, noise and resistance value requirements in order to obtain desired performance levels. Then, it discusses the design of the support arms to get the optimum thermal conductance value and the pixel body having an acceptable absorption coefficient and sustaining the mechanical stability. Absorption simulation gives the optimum structural and sacrificial layer thicknesses to get the maximum absorption coefficient. Thermal simulations are carried out for the calculation of the thermal conductance and time constant values of the pixels designed.

Chapter 3 summarizes the determination of the fabrication process flow. It starts with the design of the process flow. Then, the individual optimization for each process step is explained in detail.

Chapter 4 gives the test results obtained after the fabrication of the pixels. Performance parameters of the pixels are given in this chapter.

Finally, Chapter 5 summarizes the research work conducted in the scope of this thesis and gives the suggestions on the possible future work.

CHAPTER 2

DESIGN OF THE MICROBOLOMETER PIXELS

This chapter discusses the design considerations of the double sacrificial layer microbolometer together with the simulations. 56 different pixels were designed in the scope of this thesis differentiating from the resistor type, the width of the metal and nitride layers of the arms, and the anchor placement. Section 2.1 explains the determination of the active material, while Section 2.2 discusses the determination of the resistor type. Section 2.3 makes an overview on the detector structure and design considerations. Section 2.4 and Section 2.5 gives the results of the absorption and thermal simulations, respectively. Finally, Section 2.6 summarizes the results of the design considerations and simulations.

2.1 Determination of the Active Material

The active material of the microbolometer pixel is the most crucial component since it directly affects the sensitivity of the detector to the incident infrared radiation. TCR and noise characteristics of the active material must be considered in the first place. Responsivity is directly proportional to the TCR of the active material as explained in Chapter 1. In the case of the pixels that have a comparable support arm resistance to the detector resistance, effective TCR is considered in the responsivity calculations. Therefore, the magnitude of TCR becomes even more important in this case. Equation 1.21 shows that the NETD, which is the most important performance parameter for the comparison of the microbolometers, is directly proportional to the

rms noise value of the detector. Thus, detectors with active materials having lower noise characteristics can detect smaller temperature differences.

Resistivity is another important performance parameter for the microbolometer pixels. The readout circuits designed at METU-MEMS Center generally use the voltage bias technique [40]. Therefore, the current responsivity is taken into account for NETD calculations. Equation 1.18 gives the current responsivity relation. The responsivity decreases as the detector resistance increases since the current is higher for the lower resistances under same voltage bias. As a result, the responsivity can be maximized by keeping the detector resistance as low as possible. However, there is a limitation for the resistance of the detector. Since the current flowing through the resistor structure of the detector increases for smaller resistances, the power on the resistor also increases under the same voltage bias. This would result in the self heating problem. The differential readout method by using the reference detectors can solve the self heating problem to a certain extent [40]. Therefore, the optimum resistance for the minimum NETD must be carefully investigated. The simulations for the optimum resistance values are given in Section 2.2.

TCR, noise and resistivity characteristics of the active material directly affect the performance of the detectors. Another parameter that should be taken in consideration is the process condition of the material. Since the detectors fabricated at METU MEMS Center is monolithically integrated on CMOS substrates, the deposition and formation of the active material must be CMOS compatible. Die level uniformity and the reproducibility are also noteworthy in terms of processing the active material.

The most commonly used material is VO_x in the fabrication of microbolometers. Although it was patented by Honeywell Research Lab, many companies use this material in the fabrication of FPAs as stated in Chapter 1. VO_x has a TCR value between -2 and -3 %/K, which can be considered as high. However, there is not much information about the process conditions of this material in the literature. Therefore, an extensive research on this material is required before fabricating

microbolometer pixels with VO_x. Tungsten doped VO_x, VWO_x, is another candidate as the active material for the microbolometer FPAs [42]. Although there is a thesis work on the characterization of this material in METU MEMS Research Group [41], further research is needed to optimize the bolometric properties of this material.

Another active material for the microbolometer pixels is a-Si. It is CMOS compatible with TCR values between -2 and -3 %/K. The drawback of this material is the required high annealing temperature, which prevents its monolithic integration. Proper annealing temperature for monolithic integration could be achieved by adjusting the process conditions after an intense research which is achieved by LETI and L3 as stated in Chapter 1. However, another drawback that is the high resistivity of this material can cause a decrease in the performance of the microbolometers fabricated on the readout circuits designed at METU-MEMS Center. a-Si formation together with a proper and dedicated new readout circuitry may solve the performance decrease problem. Yet this is another research topic that must be deeply analyzed. Other research topic in this field is to dope Ge to a-Si to obtain a better performing bolometer material as studied by LETI and ULIS.

Metals are also candidates as active materials for the microbolometers. The noise level of the metals are remarkably low since they have too low 1/f noise which is the most dominant noise source in the semiconductor materials used as active detector material. However, low TCR levels take the noise advantage away.

Yttrium Barium Copper Oxide (YBCO) is another remarkable active material for microbolometers. It has TCR values between -3 and -4 %/K as stated in Chapter 1. In addition to this, YBCO has low noise levels. Figure 2.1 shows the TCR vs. temperature characteristics of YBCO deposited in METU-MEMS facilities [33]. This previous work conducted at METU showed that a TCR of around -3.45 %/K could be achieved at room temperature. Figure 2.2 shows the noise measurement results of YBCO resistors fabricated in METU-MEMS facilities under different bias currents [32]. The corner frequency for the 1/f noise of 106 kΩ YBCO resistor is 1.6

kHz and 4.3 kHz under 27 μA and 54 μA bias currents, respectively. Therefore, YBCO has a reasonable noise level and a high TCR value.

This thesis work considers to use the YBCO layer as the active microbolometer maerial, but the fabrication approach can be easily adopted to other microbolometer materials, such as VO_x or VWO.

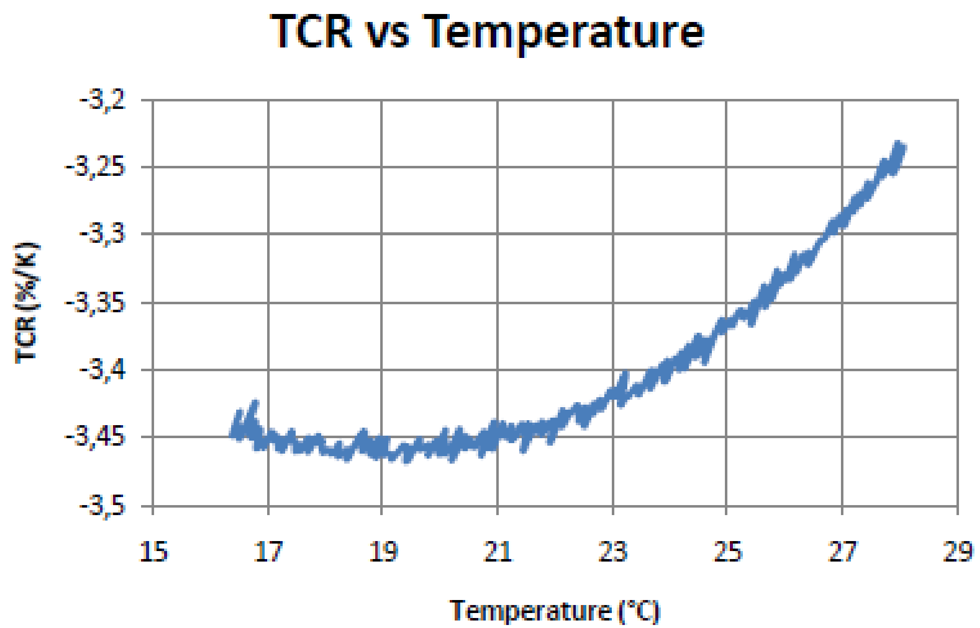

Figure 2.1: TCR vs temperature characteristics of the YBCO deposited in METU-MEMS facilities [33].

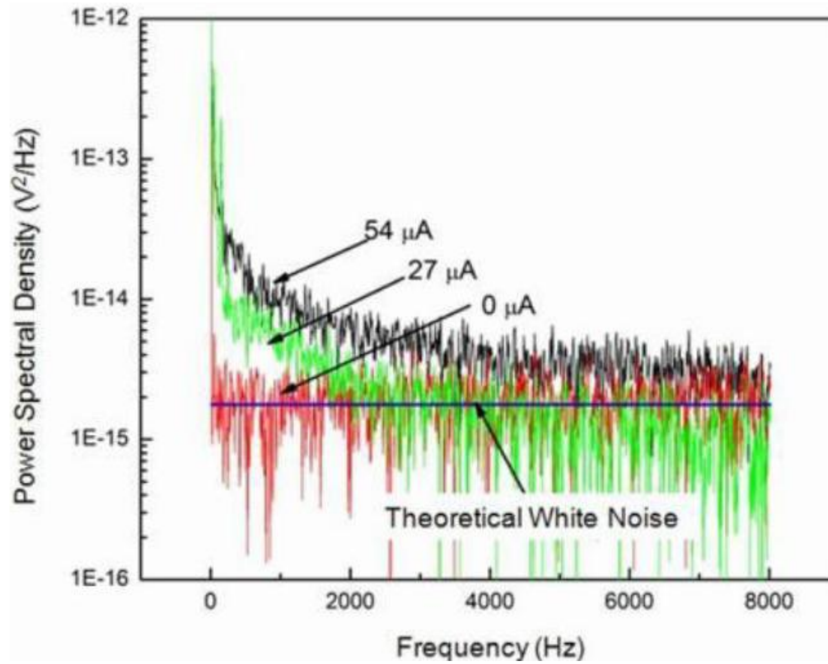

Figure 2.2: The noise measurement results of the YBCO resistor fabricated in METU MEMS facilities under different bias currents [32].

2.2 Determination of the Resistor Structure

Three different resistor structures were used in the design of different pixels in the scope of this thesis, namely: the finger type resistor, sandwich type resistor and enhanced sandwich type resistor. Following subsections explain these structures individually.

2.2.1 Finger Type Resistor

The finger type resistor is a modified version of the planar type resistors. Figure 2.3 shows a cross sectional view of a planar type resistor structure. Active detector material is deposited on two metal electrodes, thus, the current flows from one electrode to the other one as indicated in Figure 2.3. The resistance value of the planar type resistor structure is calculated as:

$$R = \rho \frac{l}{\omega t} \tag{2.1}$$

where R is the resistance of the structure, ρ is the resistivity of the active material, l is the length between the electrodes, ω is the width of an electrode, and t is the thickness of the active material layer. The desired resistance value is adjusted by changing the active material layer thickness, the electrode dimensions or the length between the electrodes. However, it is not always possible to obtain the desired resistance value for all active materials. Due to the process limitations the thickness of the active material can be increased up to only a certain value. Besides, the length between the electrodes and the width of the electrodes are limited with the pixel dimensions. Therefore, the finger type resistor structure was proposed to obtain higher resistance values than the ones got with the planar type resistors.

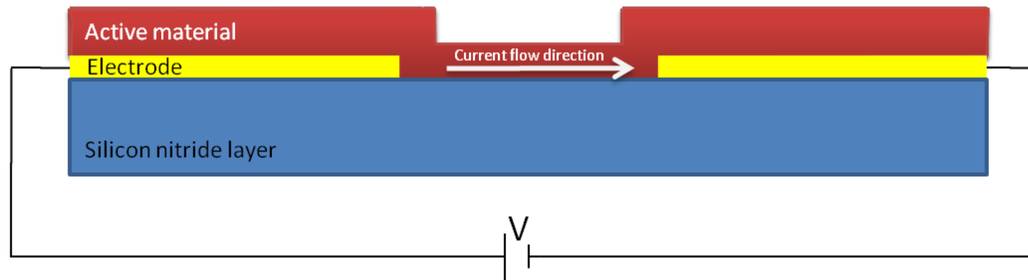

Figure 2.3: Cross sectional view of a planar resistor.

Figure 2.4 shows the top view of the electrodes of a finger type resistor structure. As it is seen in this figure, the length of the resistor given in Equation 2.1 is the spacing between the fingers of the electrodes and the width of the resistor is the total length among the finger that is shown as dashed line.

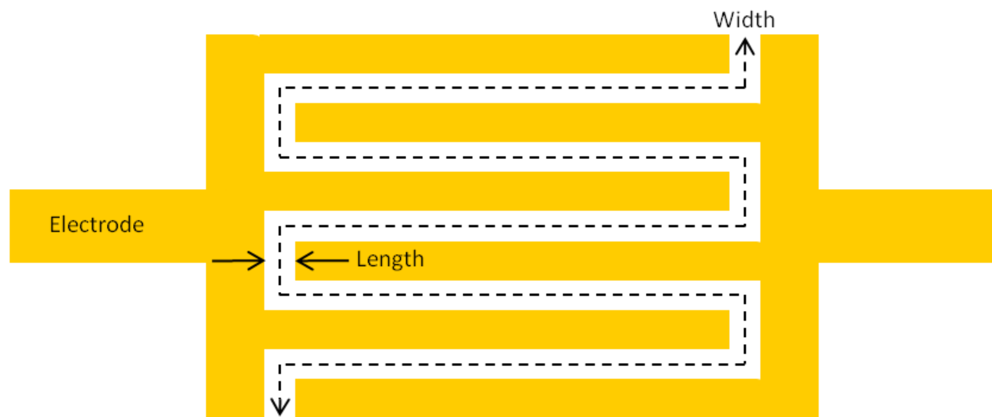

Figure 2.4: Top view of two electrodes of a finger type resistor structure.

Previous studies conducted at METU showed that the W/L ratio of the finger type resistor must be kept as high as possible to obtain 100 kΩ or closer resistance values [32]. High W/L ratio requires either a large number of electrode fingers or lower distance between the fingers. For the small size of pixels such as 25 µm or 17 µm, it may be needed to apply both. Increase in the number of fingers means enlargement of the metal layer on the pixel area at the same time. This affects the absorption performance of the pixel negatively. Besides, the small distances between the electrode fingers necessitate more advanced etching techniques than the wet etching process.

Another drawback of the finger type resistor is the nitride deposition process that is conducted after the formation of the active material layer. This nitride layer is deposited to prevent the oxidation of the YBCO layer during the release of the pixels in O_2 plasma. Nevertheless, high process temperature, 300 C, changes the resistivity of the YBCO unpredictably.

Although all different support arm structures were designed with pixel bodies having finger type resistors as well as the other resistor structures, none of the pixels with the finger type resistor were tested considering mentioned drawbacks.

2.2.2 Sandwich Type Resistor

Another resistor structure used in microbolometer pixels is the sandwich type resistors. Figure 2.5 shows a cross sectional view of this type resistor structure. As indicated in the figure, after the formation of the bottom electrode an isolation layer such as silicon nitride (Si_3N_4) is deposited and etched to form a resistor opening. Active material is fabricated on the top of this layer together with the top electrode layer for in-situ fabrication. The current flow direction is vertical in this type of resistor.

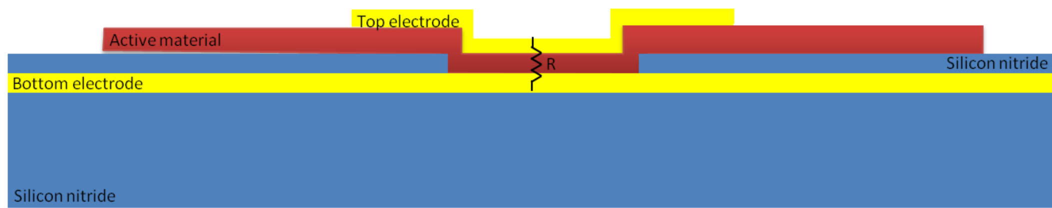

Figure 2.5: Cross sectional view of a sandwich type resistor.

Since the current flow direction of the sandwich type resistor is different from the finger type, resistance equation becomes:

$$R = \rho \frac{t}{WL} \tag{2.2}$$

where R is the resistance of the sandwich type resistor structure, W and L are the dimensions of the isolation layer opening, and t is the thickness of the active material layer. Figure 2.6 shows a top view of the bottom electrode together with the isolation layer deposited and etched to form resistor opening on the top of it. W and L, which forms the active resistor area, are shown in this figure.

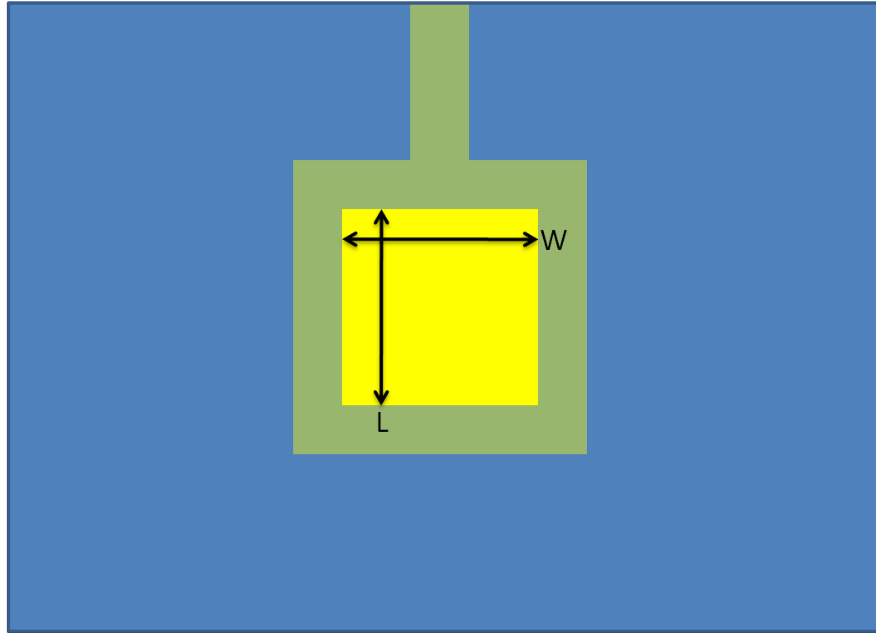

Figure 2.6: Top view of the bottom electrode and etched isolation layer.

Although this type of the resistor has a better performance in terms of absorption, the resistance value obtained is not high enough. The resistance obtained using this structure in the 25 µm single pixel fabrication trials is around 30 kΩ. The desired value is 60 kΩ considering the NETD and readout performances together [40]. Increase in the active material thickness would increase the resistance, however, the given resistance value was obtained at the undercut limit of the YBCO. Since the active material is etched away by wet etchant in METU-MEMS facilities, the undercut of this layer is inevitable due to the isotropic etching characteristics. Another solution to the low resistance problem is to decrease the resistor opening dimensions. Nonetheless, this would increase the noise of the resistor since the 1/f noise rises with the decrease in the active resistor area. This phenomenon will be explained in Chapter 4 in detail.

2.2.3 Enhanced Sandwich Type Resistor

Enhanced sandwich type resistor is a modified version of the sandwich type resistor. There are two bottom electrodes each having a resistor opening on the top of it. The contacts to the support arms are provided by the bottom electrodes. Figure 2.7 shows the cross sectional view of an enhanced sandwich type resistor. As indicated in the figure, the total detector resistance can be considered as the equivalent resistance of two series connected sandwich type resistors. Therefore, the total resistance of the enhanced sandwich type resistor is the double of sandwich type.

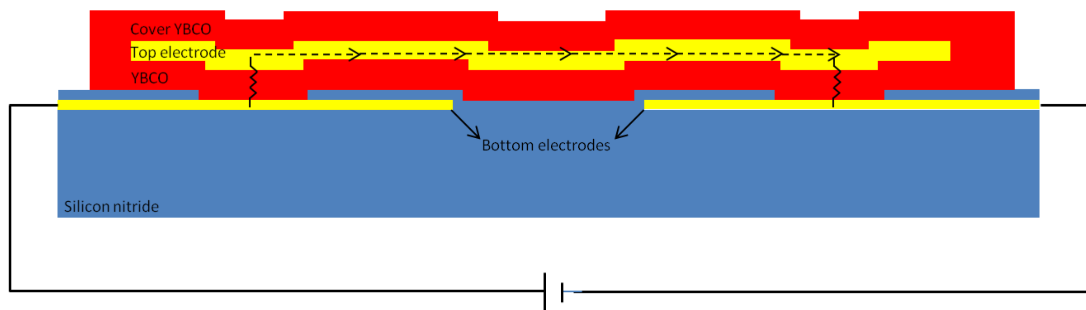

Figure 2.7: Cross sectional view of an enhanced sandwich type resistor.

The cover YBCO shown in Figure 2.7 was deposited to prevent the oxidation of the YBCO layer during the release of the pixels in O_2 plasma. This layer was deposited under the same conditions with the active YBCO layer; thus, resistance values do not alter like the finger type resistor case.

The resistance values obtained with these types of resistors are between 50 and 55 kΩ. These values are lower than the expected value, 60 kΩ. The reason of this mismatch is the fact that the resistor openings are fabricated 0.3 µm larger than expected as will be explained in Chapter 3 in detail.

2.3 Detector Structure

Two-level microbolometer design can be considered as the combination of two different designs. The first level is composed of only support arms; therefore, the main design consideration in this level is the thermal conductance value. In the second level, the pixel body with the resistor structure must be designed such that the absorption coefficient is maximized while adjusting the desired resistance values. Following subsections analyze two levels of the microbolometer pixels separately.

2.3.1 The Design of the Support Arms

The thermal conductance, G_{th}, is the most crucial performance parameter in the design procedure of a microbolometer pixel. The thermal conductance of the support arms, G_{th_arms}, is the most dominant component of the total thermal conductance of the pixel as explained in Chapter 1. Therefore, it was aimed to decrease the thermal conductance down to an acceptable level in the scope this thesis. It must be kept in mind that the thermal time constant tends to increase while thermal conductance is decreasing. The maximum time constant value for the frame rate of 30 fps is calculated as 16 msec using Equation 1.13 in Chapter 1. This value decreases further to 8 msec for 60 fps frame rate application.

Under the consideration of these parameters, the main objective of the support arm design step is to decrease the thermal conductance value as low as possible while keeping the thermal time constant below 16 msec.

The process limitations must be taken into account in addition to the performance parameters. The width of the arm metal and nitride layers, the spacing between the arms, and the width of the anchor openings were designed under the consideration of the limitations and parameters mentioned above. The pixels designed in the scope of this thesis are categorized as two different types regarding the width of the metal and the nitride layers of the support arms.

2.3.1.1 Pixel Type 1

In Pixel Type 1, the width of the metal and the nitride layers of the support arms are equal. Therefore, one mask is enough to form both nitride and metal layers. As a starting point, the pixels with the minimum thermal conductance value that can be obtained using the technology in the METU-MEMS facilities were designed. The minimum feature size that is producible in the METU MEMS facilities for the metal and nitride formation is 0.5 µm. Hence, the width of the metal and the nitride layers was set to 0.5 µm for the initial designs. The spacing between the arms differs from 0.6 µm to 1.0 µm. Figure 2.8 shows the layouts of the first levels with 0.5 µm arm width. The thermal conductance values of these pixels are below 10 nW/K; however, the time constants are above 30 ms.

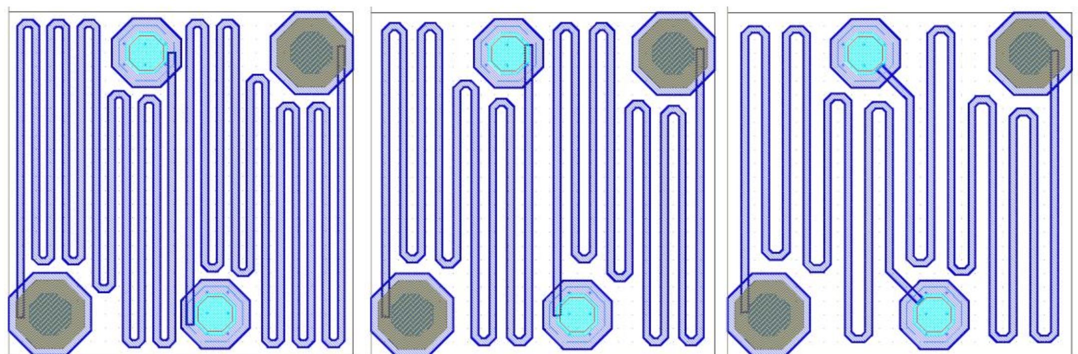

Figure 2.8: Layouts of the first levels with 0.5 µm arm width.

Since the time constants of the pixels with the arm width of 0.5µm are higher than the desired level, the pixels with the arm with of 0.8 µm were designed in order to obtain acceptable time constant values. Besides, the nitride and metal RIE processes of the arms of these pixels are tolerant to the problems like undercut. The spacing between the arms varies same as the support arms with the arm width of 0.5 µm. Figure 2.9 shows the layouts of the first levels with 0.8 µm arm width. The thermal conductance values of these pixels are around 20 nW/K, and the time constants are changing from 10 ms to 20 ms depending on the thickness of the metal layer of the support arms. The thermal conductance and time constant values of these pixels promise a good detector performance.

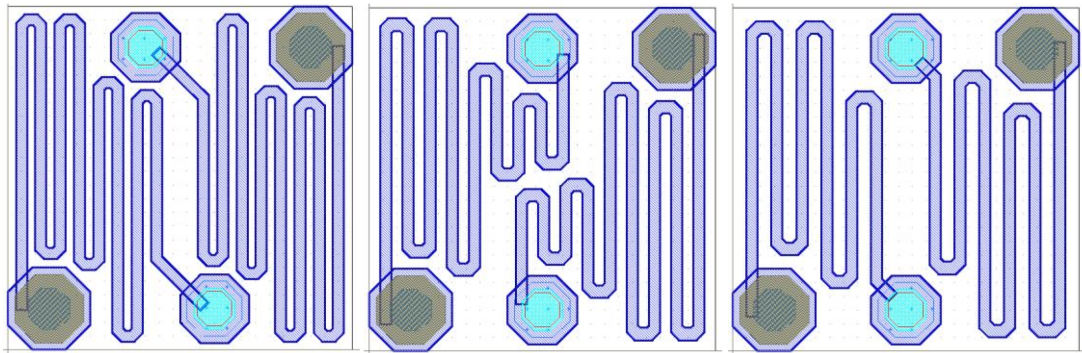

Figure 2.9: Layouts of the first levels with 0.8 µm arm width.

Although the pixels with 0.8 µm arm width met the desired thermal conductance and time constant values, the pixels with the arm width of 1.0 µm were also designed. The pixels with the arm width of 1.0 µm had been fabricated in METU-MEMS Center facilities in the 35 µm arrays [34]. Therefore, the pixels with the arm width of 1.0 µm were also included in the single pixel designs in order to prevent problems occurring during the fabrication step. Figure 2.10 shows the layouts of the first levels with 1.0 µm arm width. Thermal conductance values of these pixels are around 25 nW/K, and the time constant values are approximately 15 ms.

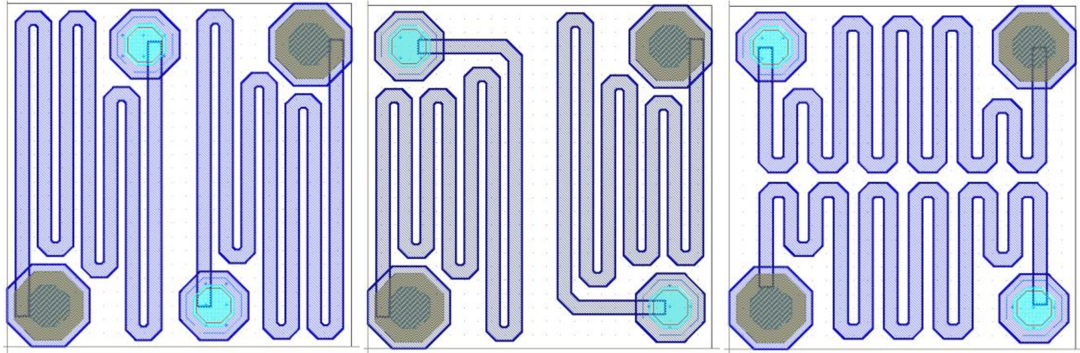

Figure 2.10: Layouts of the first levels with 1.0 μm arm width.

The thermal simulation results and expected performance comparison of the selected pixels will be illustrated in Section 2.5 in detail. The thermal simulation results for all of the designed pixels are given in Appendix A.

2.3.1.2 Pixel Type 2

When the thicknesses of metal and the nitride layers are equal, the arm metal could be exposed to the oxygen in the air. This may result in the oxidation of the arm metal, which is titanium in our case. Therefore, the width of the metal and the nitride layers of the support arms are different in this type of pixels in case there would be a problem with the arm metal that is exposed to oxygen.

There are 6 different types of Type 2 pixels regarding the support arm formation. Table 2.1 shows the width of the metal and nitride layer of the support arms, stated as W_{metal_layer} and $W_{nitride_layer}$ respectively, and the spacing between the support arms, indicated as $W_{spacing_arms}$.

Table 2.1. Width of the metal and nitride layers of the support arms for Pixel Type 2.

W_{metal_layer}	$W_{nitride_layer}$	$W_{spacing_arms}$
0.5 μm	0.7 μm	0.6 μm
0.5 μm	0.8 μm	0.6 μm
0.5 μm	1.0 μm	0.6 μm
0.7 μm	0.9 μm	0.6 μm
0.7 μm	1.2 μm	0.6 μm
0.7 μm	1.2 μm	0.8 μm

The main approach in the design of the Type 2 pixels was to keep the metal layer of the support arms as small as possible to obtain lower G_{th} while enlarging the width of the nitride layer for the coverage of the metal layer of the support arms. The sizes of the coverage vary as 0.1 μm, 0.15 μm, and 0.25 μm for the sake of independency from the misalignment in the lithography step. The spacing between the support arms was kept small in order to form longer support arms. Figure 2.11 shows the Type 2 pixels with the support arms having 0.5 μm wide metal layers while Figure 2.12 incating the ones having 0.7 μm wide metal layers.

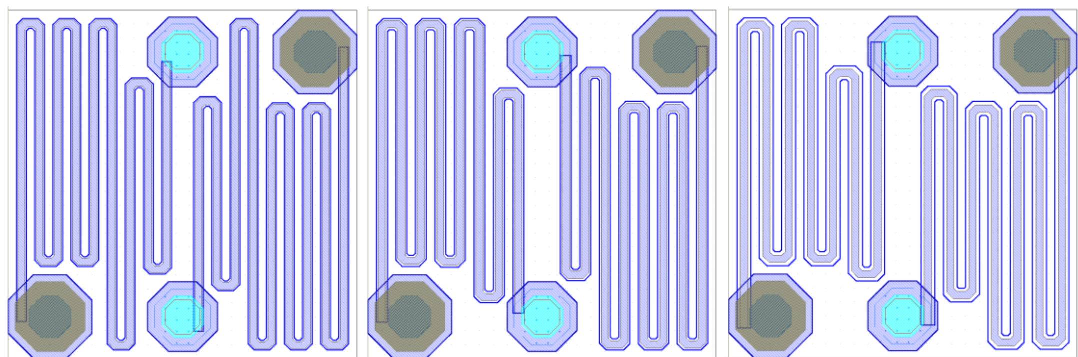

Figure 2.11: Type 2 pixels with the support arms having 0.5 μm wide metal layers.

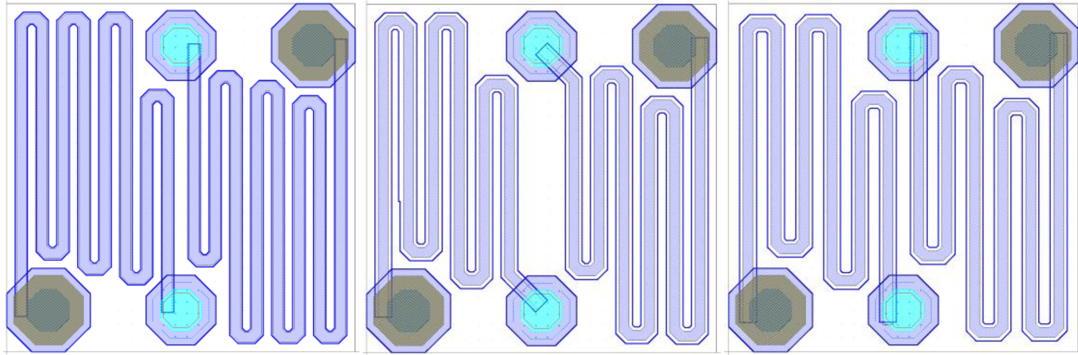

Figure 2.12: Type 2 pixels with the support arms having 0.7 µm wide metal layers.

2.3.2 Design of the Pixel Body

The pixel body is composed of the resistor structure, absorber layer, and the structural layer carrying both. The determination of the resistor structure is explained in Section 2.2. All three resistor structures, namely the finger, the sandwich, and the enhanced sandwich types, were applied on all different support arm structures. The optimum performance, in terms of resistance value and reproducibility, was obtained by the enhanced sandwich type resistors as stated in Section 2.2. Figure 2.13 shows the implementation of all types of resistors on the support arm with the arm metal width of 0.8 µm.

As a result of the forming the support arms in the first level, the absorber layer covers the whole second level. Thin metallic film is used as the absorber layer at METU-MEMS Center. Therefore, it is crucial to isolate the top and bottom electrodes in order to prevent the short circuit. The top and bottom electrodes of the sandwich and enhanced sandwich type resistors are at the different nitride layers. The process steps will be explained in Chapter 3 in detail. An isolation layer to prevent the oxidation of the YBCO layer is deposited for the finger type resistor as stated in Section 2.2.1. Thus, the short circuit problem does not arise for the finger type resistors.

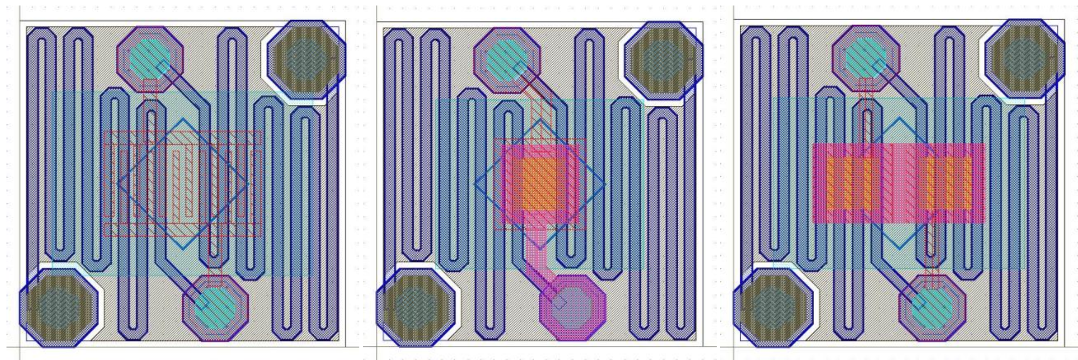

Figure 2.13: Implementation of all types of resistors on the support arm with the arm metal width of 0.8 µm.

Another crucial property of the pixel body is the placement of the anchors that connects the first and the second layers. In order to prevent the mechanical stability problems different anchor placements were designed in this study. Figure 2.14 shows the layouts of the first levels of the pixels with 0.5 µm arms and different anchor placements.

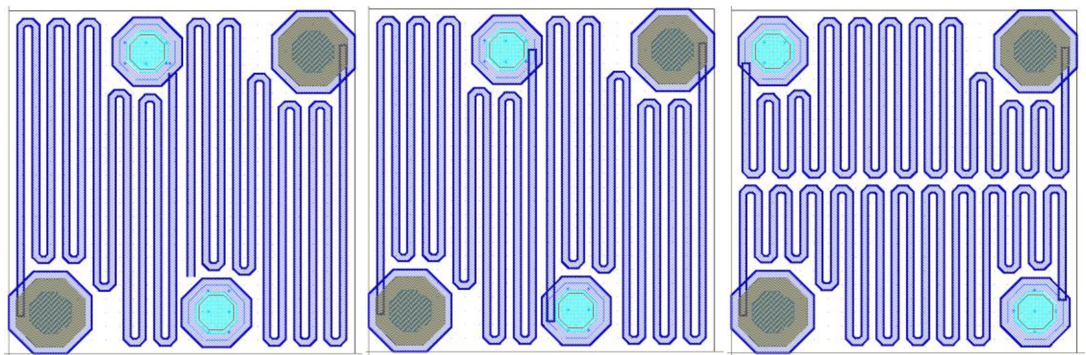

Figure 2.14: Layouts of the first levels of the pixels with 0.5 µm arms and different anchor placements.

2.4 Absorption Calculations of the Pixels

Formation of the support arms in the first level ensures better thermal conductance values by allowing the usage of the whole level for them. Then, resistor structure and the absorber layer are fabricated in the second level to increase the fill factor of the pixel. In order to complete the optimization of the pixel performance by maximizing the absorption of the pixel, a detailed analysis of the absorption coefficient is needed.

2.4.1 Theory

The absorption coefficient of a pixel can be calculated using the cascaded transmission line (CTL) model [43]. In the CTL model, all layers are represented by their characteristic impedances [44]. In the absorption simulations, the microbolometer pixel is divided into sub-regions consisting of different stacks of layers. Figure 2.15 shows a representative perspective view of a stack of layers and its corresponding CTL model. In order to obtain the absorption coefficient of the pixel, it is essential to calculate the input resistances of these sub-regions. The equivalent input resistances of these subregions can be calculated by using the Telegrapher's Equation [45]. The impedance seen from the input of a medium having a characteristic impedance Z and a load impedance Z_L is given by Telegrapher's Equation:

$$Z_{in} = Z\frac{Z_L + Z\tanh(\gamma l)}{Z + Z_L\tanh(\gamma l)} \tag{2.3}$$

where, γ is the complex propagation constant of the medium and l is the thickness of the layer. The equivalent input impedance of the structure given in Figure 2.15 can be derived by applying the Telegrapher's Equation starting from the first cavity.

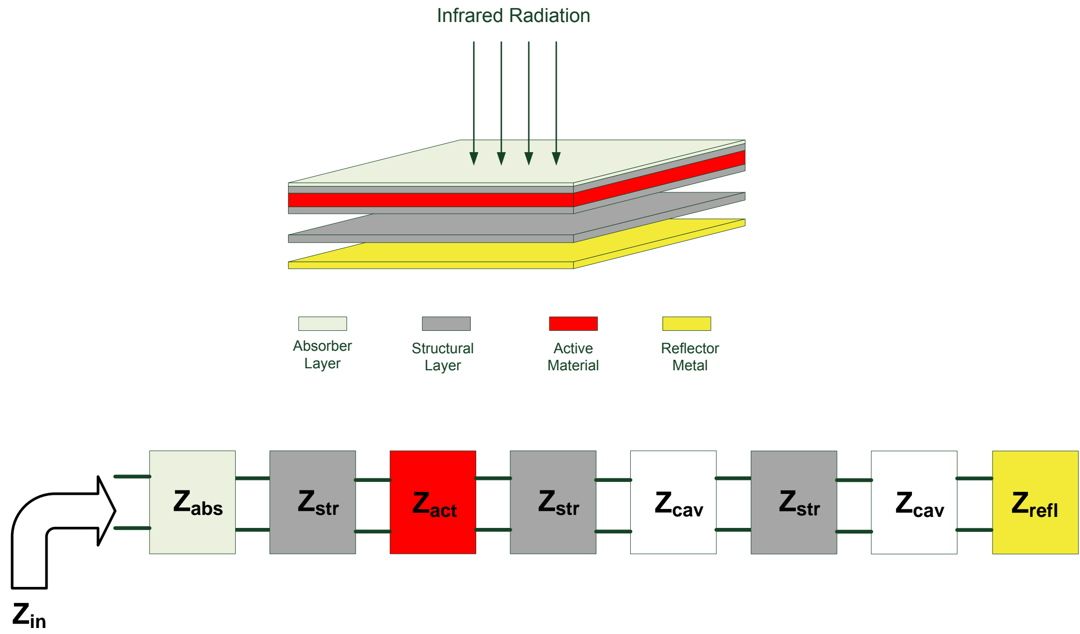

Figure 2.15: Representative perspective view of a layer stack and its corresponding CTL model.

The absorber layer of a microbolometer can be fabricated as a very thin metallic film to match its sheet resistance to that of free space which is 377 Ω/□. Since the thickness of the absorber is much smaller than the skin depth at the working wavelength, it can be modeled as a lumped resistor [46]. Figure 2.16 shows the modified CTL model of the layer stack in Figure 2.15 with a lumped resistor instead of the absorber layer. Then, the equivalent impedance of the layer stack is obtained as,

$$Z_{in} = R_{s_abs} \,//\, Z_{L_abs} \tag{2.4}$$

where, R_{s_abs} is the sheet resistance of the absorber layer and Z_{L_abs} is the load impedance of the absorber layer.

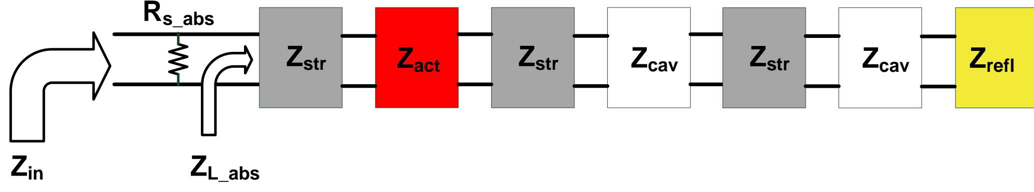

Figure 2.16: The modified CTL model of the layer stack.

The equivalent impedances of the stacks of layers extracted using Equation 2.4 are used to calculate reflection coefficients of these layer stacks. The reflection coefficient of the structure in Figure 2.16 is calculated using the formula,

$$\Gamma_{inf} = \frac{Z_{in} - Z_0}{Z_{in} + Z_0} \tag{2.5}$$

where, Γ_{inf} is the reflection coefficient of the infrared radiation incident on the absorber layer, Z_{in} is the equivalent input impedance of the structure, and Z_0 is the characteristic impedance of free space.

There is no transmission through the microbolometer structure since there is a reflective layer at the bottom of the pixel. Therefore, the incident radiation is either reflected or absorbed by the structure. The ratio of the absorbed infrared power to the incident power is,

$$P_{abs} = (1 - |\Gamma_{inf}|^2)P_{in} \tag{2.6}$$

where, P_{abs} is the absorbed power and P_{in} is the incident power. This equation gives the power absorbed by a single layer stack. The total absorbed power can be obtained by calculating the amount of the power absorbed by each individual stack of layers using Equation 2.6 and then summing them up. In the following step, the total absorption coefficient of the detector is found by calculating the weighted average of

the individual absorption coefficients of all stacks of layers with respect to their areas as follows [47],

$$P_{abs_{\%}} = \frac{(1-\Gamma_1^2)S_1 + (1-\Gamma_2^2)S_2 + \cdots + (1-\Gamma_n^2)S_n}{S} \text{x}100 \quad (2.7)$$

2.4.2 Absorption Simulations

The CTL model constructed in the previous section is used in the absorption simulations to calculate the optimum structural and sacrificial layer thicknesses. Equations 2.5 and 2.6 show that the load impedance of the absorber should be infinite, and the sheet resistance of the absorber should be equal to that of the free space in order to get 100 % absorption. The sheet resistance of the absorber can be fixed to the desired value by determining the thickness of this layer. The load impedance of the absorber can be adjusted by varying the layer thicknesses of the microbolometer pixel and the optical constants that depends on the deposition conditions of the layers. In the simulations, the optical constants of the layers are assumed as constant since the process conditions are determined with respect to the other performance parameters and these conditions are fixed. Optimization of the process conditions will be explained in Chapter 3 in detail.

The maximum load impedance is obtained by adjusting the thickness of the absorber to a quarter of the working wavelength if there is only one layer between the absorber and the mirror metal [48]. However, this approach cannot be used for simulations of pixels where there is more than one layer in the pixel structure. Figure 2.17 shows the isometric view of the multilevel pixel used in the simulations. The structure is divided into 8 different regions with respect to the layer stacks.

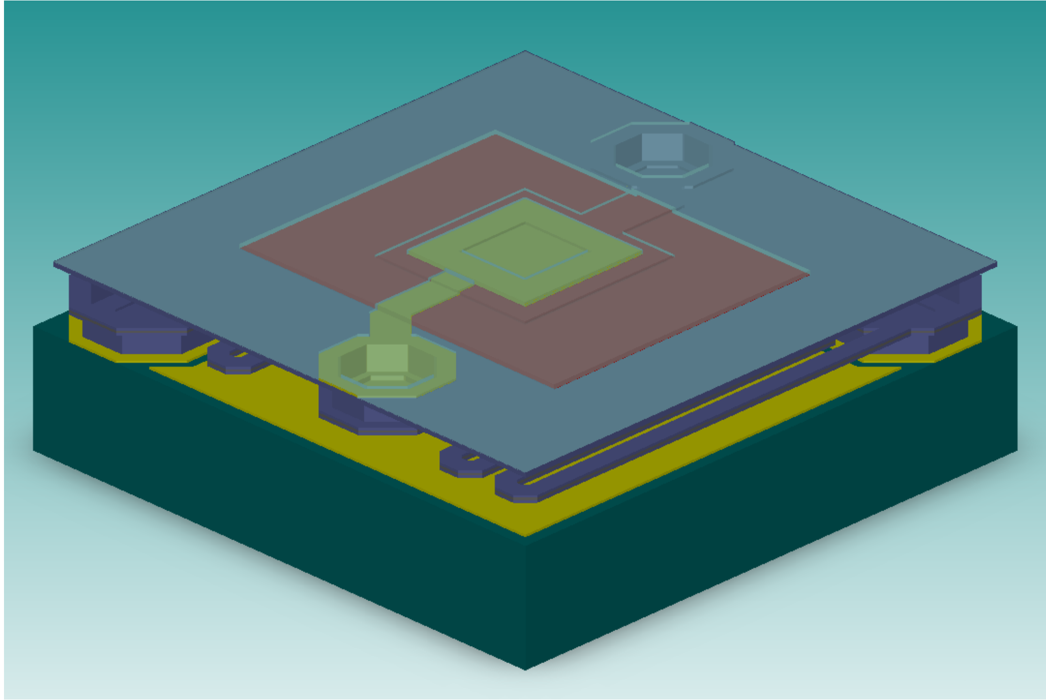

Figure 2.17: Isometric view of the pixel used in the simulations.

The simulations are performed using Matlab Software. The thicknesses are assumed to be 50 nm for both the top and the bottom electrodes of the enhanced sandwich type resistor and 200 nm for the active material. The sheet resistance of the absorber layer is adjusted as 377 Ω/□. The structural layer thickness is selected as 200 nm. There are a number of constraints while choosing the thickness of this layer. Some introduce lower limits for the thickness while some others bring upper limits. One of the constraints is the thermal conductance, which can be decreased by minimizing the thickness of the structural layer. On the other hand, the time constant of the detector is in tendency to increase proportionally with the decrease in the structural layer thickness of the detector as explained in Chapter 1.Therefore, the thickness of the structural layer can be decreased as low as possible unless the thermal time constant reaches 16 ms, which is the upper limit for the operation of 30 fps. However, there is another constraint for the structural layer thickness due to the force exerted on the support arm that may lead to buckling. The force on a support arm is given as,

$$F = kx \quad (2.8)$$

where, k is the spring constant and x is the total displacement in z direction. The spring constant, k, for an arm is defined as:

$$k = E\frac{wh^3}{l^3} \quad (2.9)$$

where E is the Young's Modulus of the structural layer material, w is the width, h is the thickness and l is the length of the arm. Equations 2.8 and 2.9 show that the displacement in the z direction, which can be considered as buckling, is proportional to the third power of the thickness. As a result, the thickness of the first structural layer must be adjusted taking mechanical stability into account.

Under all these conditions, the thickness of the structural layer for the support arms is adjusted as 200 nm. Then, the absorption simulation is carried out by varying the structural layer thickness of the second level and the total sacrificial layer thickness, i.e., the sum of the first and the second cavity thicknesses. Table 2.2 shows the optical constants used in the simulations. The wavelength of the incident infrared radiation is chosen as 10µm which is in the middle of the long-wave infrared region.

Table 2.2: Optical constants used in the simulations.

	Extinction Coefficient	Refractive Index
Structural Layer	1.3	1
Active Material	0	2

Figure 2.18 shows the variation of the absorption coefficient with respect to the structural layer thickness of the second level and the total sacrificial layer thickness. Maximum absorption percentage of 75.5% takes place for the second structural layer thickness of 70 nm and the total sacrificial layer thickness of 2 µm. However, the

second structural layer thickness is chosen as 200 nm considering the mechanical stability of the microbolometer pixel. The absorption for a structural layer thickness of 200 nm and a total sacrificial layer thickness of 2 μm is 74.8% which is very close to the maximum value. The first and second sacrificial layer thicknesses are kept as equal in this simulaton

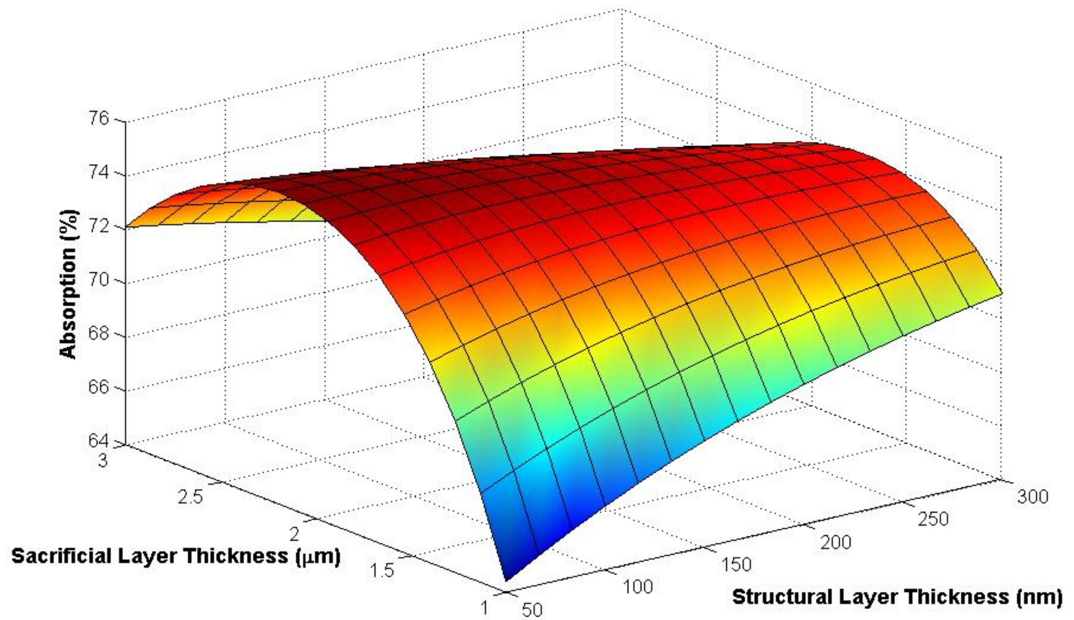

Figure 2.18: Variation of the absorption coefficient with respect to the total sacrificial layer thickness and the structural layer thickness of the second level.

The variation of the absorption coefficient with respect to the thickness of the first sacrificial layer is observed in another simulation. The thickness of the second layer is chosen as the difference between the total thickness and the first sacrificial layer. Figure 2.19 shows the variation of the absorption coefficient with respect to the first sacrificial layer thickness. The results show that the optimum thickness for the first sacrificial layer is 0.6 μm, and the thickness of the second sacrificial layer is 1.4 μm. The absorption percentage is raised to 75.2% for these thicknesses of the sacrificial layers. Since the absorption percentage do not increase as a significant amount, the thicknesses of the first and second sacrificial layer is kept as equal.

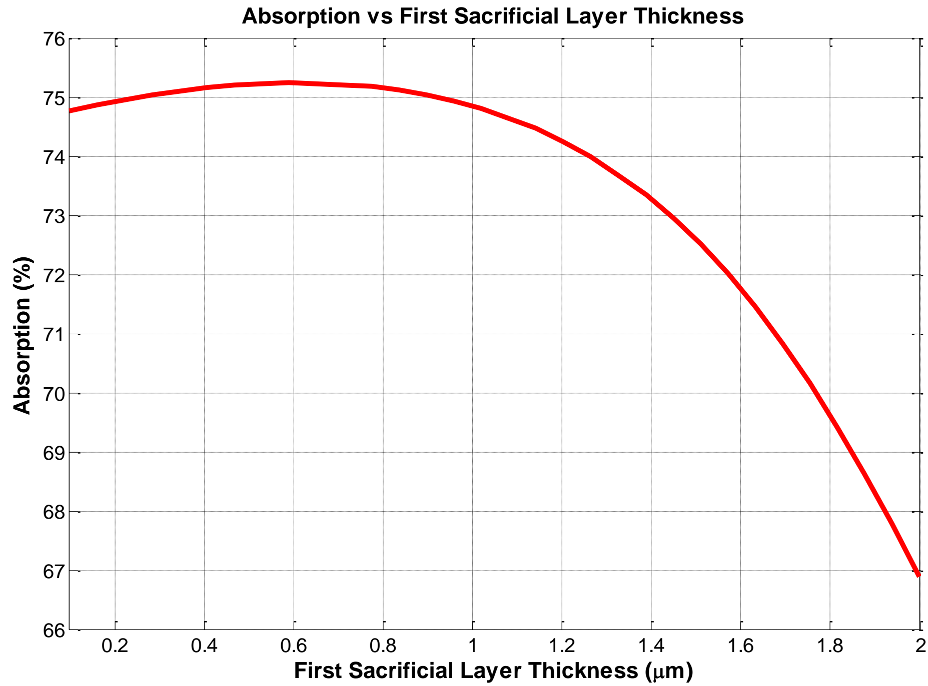

Figure 2.19: Absorption coefficient variation with respect to the first sacrificial layer thickness.

The dependence of the absorption percentage on the sheet resistance of the absorber layer is simulated. Figure 2.20 shows the variation of the absorption with respect to the sheet resistance of the absorber layer. The maximum absorption occurs for the sheet resistance value of 500 Ω/□ which may be considered as in agreement with the initial design value of 377 Ω/□. In fact the absorption is increased up to 76.3 % from 74.8 % when the sheet resistance of the absorber layer is set to 500 Ω/□ instead of 377 Ω/□. For a range between 350 Ω/□ and 800 Ω/□, the absorption does not alter significantly.

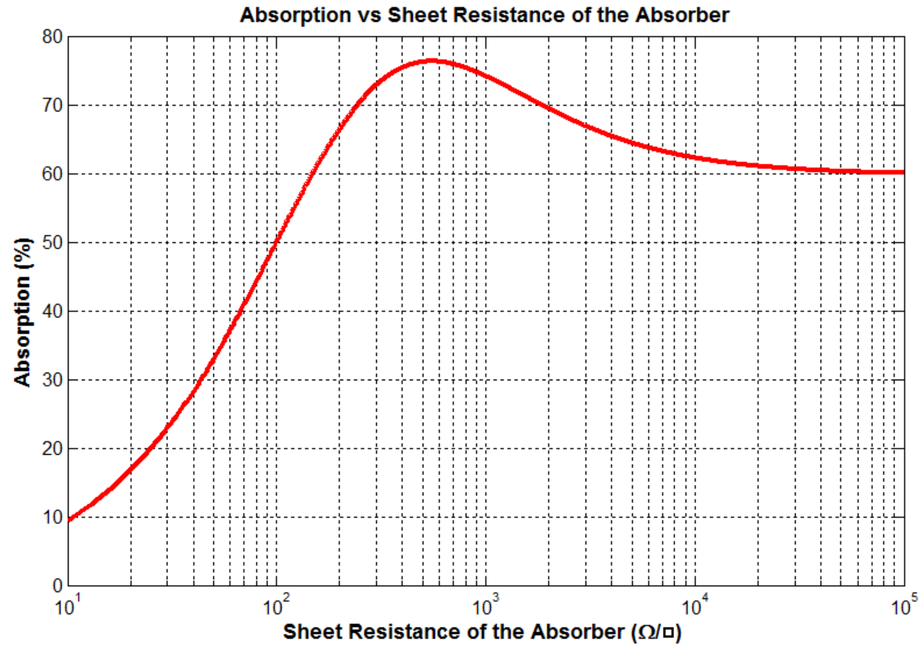

Figure 2.20: Variation of the absorption coefficient with respect to the sheet resistance of the absorber layer.

The simulations mentioned above are carried out taking the refractive index and the extinction coefficient of the structural and active materials as constant since the wavelength is chosen as 10 µm which is in the middle of long-wave infrared region. However, the refractive index and extinction coefficient values for these materials change with respect to the wavelength. Therefore, a detailed analysis on the absorption of the pixel must be carried out considering the effects of these wavelength dependent parameters. Figure 2.21 shows the variation of the absorption of the microbolometer pixel structure with respect to the wavelength using the chosen sacrificial and structural layer thicknesses, which are 2 µm and 200 nm, respectively. The refractive index and the extinction coefficient values are measured for the wavelength range between 3 µm and 25 µm, and these values are used in the simulations. The pixel structure has an average absorption percentage of 69.5 at the wavelength range of 8-12 µm.

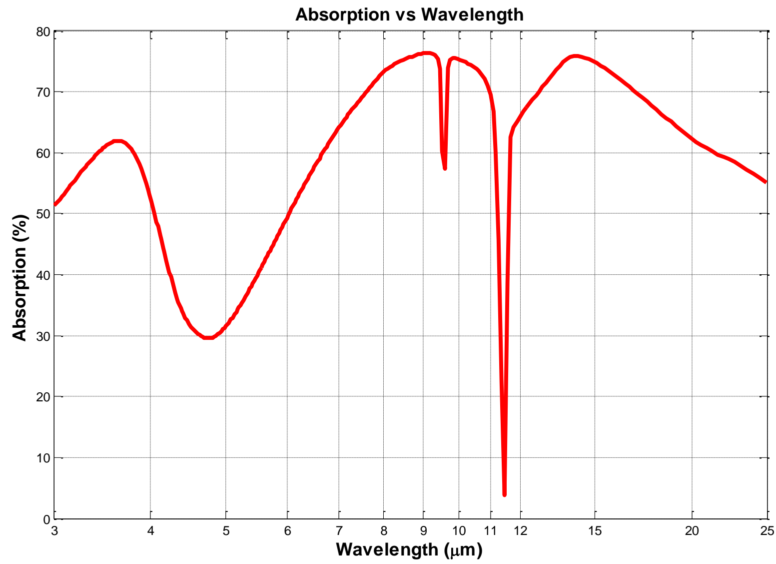

Figure 2.21: The Variation of the absorption of the microbolometer pixel with respect to the wavelength.

2.5 Thermal Simulations

The thermal conductance and the time constant of the microbolometer pixels are key features that give an idea about the expected NETD levels of the detector. Therefore, the thermal simulation of the pixel is the most important design step. The simulations are conducted using the finite element method (FEM) by CoventorWare software. The thermal simulations of all designed pixels are completed. However, the thermal simulation results of only one of the pixels are explained in this section. The thermal simulation results of all the pixels are given in Appendix A. The pixel with 0.8 μm arm metal width and 0.8 μm arm spacing is used in the simulations. Table 2.3 shows the thermal properties of the layers used in the simulations. The simulation is carried out assuming that the pixel is initially at 300 K and then exposed to 100 nW infrared radiation power. Figure 2.22 shows the result of the thermal simulation. The temperature of the pixel rises to 305.96 K. Thermal conductance value of the pixel is found as 16.8 nW/K. Figure 2.23 shows the

variation of the pixel temperature with time. The time constant of the pixel is found as 19.3 msec. These results are compatible with the result reported in the literature for 25 µm pixels [36].

Table 2.3: The thermal properties of the layers used in the simulations.

	Si_3N_4	Ti	Au	YBCO	NiCr
Thermal conductivity (W/mK)	01	219	320	35	113
Spesific Heat (J/cm^3K)	2.2	2.36	2.49	2.65	3.78

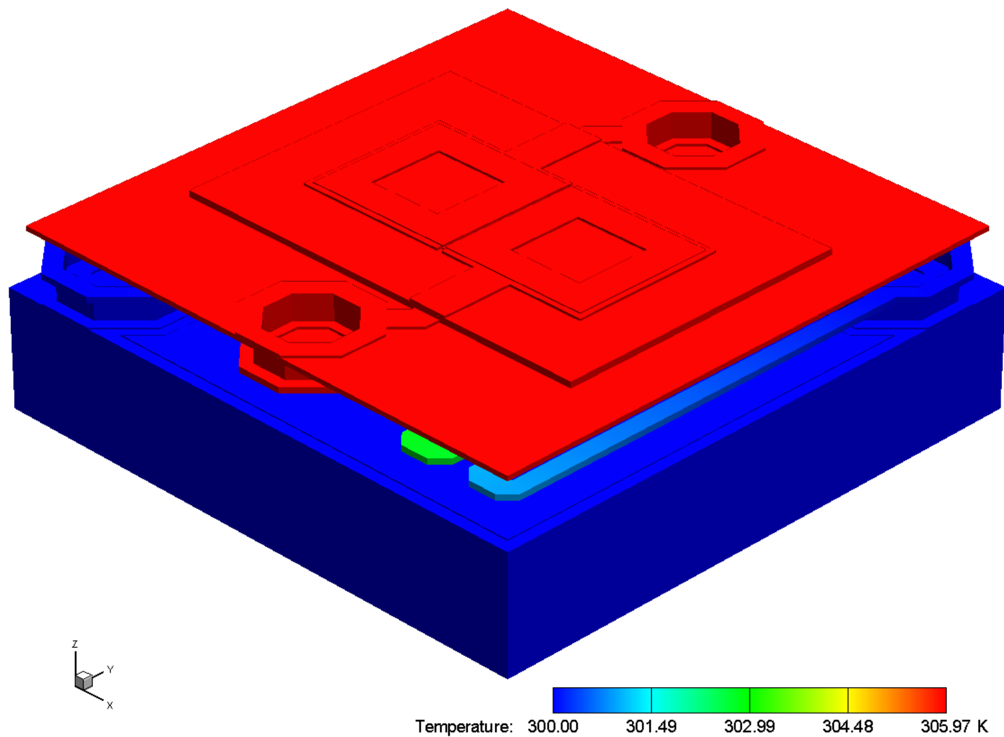

Figure 2.22: Result of the thermal simulation.

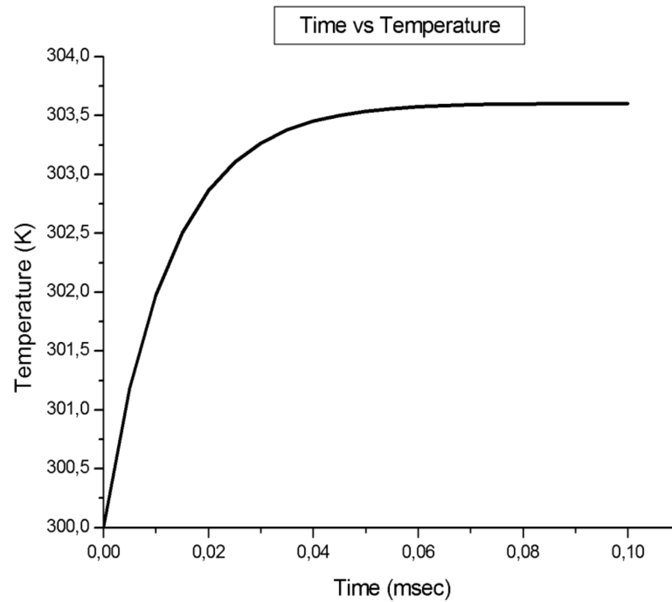

Figure 2.23: The variation of the pixel temperature with time.

2.6 Conclusion

This chapter explains the design considerations and the optimization of the microbolometer pixels together with the simulation results. The active material is determined as YBCO, which has a relatively high TCR value and relatively low noise levels. Then, the resistor structure which would give the desired resistance value is determined as enhanced sandwich type resistor. The design of the support arms and the pixel body are explained considering the performance and mechanical stability of the pixels. Absorption simulations summarize the effects of the structural and sacrificial layer thicknesses on absorption coefficient. Optimum structural and sacrificial layer thicknesses are obtained in these simulations. Finally, the thermal simulation shows that a pixel with 16.8 nW/K thermal conductance and 19.3 msec time constant can be fabricated.

CHAPTER 3

FABRICATION PROCESSES OF THE MICROBOLOMETER PIXELS

This chapter summarizes the fabrication steps of the microbolometer pixels designed in the scope of this thesis. The resistive type microbolometer pixels are designed using CMOS compatible surface micromachining techniques since the detectors are intended to be fabricated on CMOS readout circuits. Section 3.1 explains the design of the fabrication process stating the considerations taken into account during the design procedure. Section 3.2 indicates the optimization of the process steps. Finally, Section 3.3 summarizes the chapter.

3.1 Design of the Fabrication Process

The achievement of the desired high performance detector is only possible with the implementation of the pixel parameters as close as possible to the design parameters. Therefore, the fabrication process must be determined cautiously before starting the step by step implementation. There are a number of key features that determine the design of the fabrication process. The most important one is the capabilities of the available fabrication facility. The minimum feature size must be compatible with the capabilities of the facility and some pixels with the safety margins must be also included for the first design trials. The coherency of the successive process steps is another important consideration. In other words, a process step must not affect the

previous one. If it is inevitable to conduct a process that affects the previous one, necessary precautions, such as masking the sensitive layers, must be taken. The adhesion characteristic of the layers is another consideration that must be taken into account for the successive process steps. However, in some process steps it may be necessary to deposit a layer on the top of another even it is nonadhesive. Using an additional thin layer which is adhesive to both two layers is an approach to solve this kind of adhesion problem. Topological effects must also be taken into account especially for the critical dimensions. The topology caused by the thick layers may prevent the fine lithography or the etching processes of the structures with small dimensions.

The design of the fabrication process for the microbolometer pixels with double sacrificial layer is completed considering all these criteria. The fabrication processes of the pixels with all three resistor types are designed. However, only the process flow of the pixels with the enhanced sandwich type resistor is explained in this chapter. The criteria mentioned above can be considered as the common design criteria that are applicable for all kinds of designs. In order to optimize the proposed process, hence the pixel structures, there are also some specific parameters that need to be considered together with the common criteria mentioned above. These parameters are summarized below:

- The process steps must be CMOS compatible. Although the proposed pixel structures are fabricated as single pixels, the long term aim is to fabricate the detector array on a CMOS substrate. Therefore, the processes like annealing above 400 C must be avoided.
- The absorption simulations are conducted assuming that the mirror metal is a good reflector as explained in Chapter 2. Therefore, the mirror metal must be a good enough reflector in order to fulfill the absorption requirement. Moreover, this metal must be a good conductor since the path from pixel to the pads used for the tests is provided in this layer.

- Another parameter used in the absorption simulation is the sacrificial layer thickness. Therefore, the thickness optimization of the sacrificial layer must be conducted to match the optimum values obtained in the simulations. The choice of the sacrificial layer is another concern in terms of the process simplicity. This layer must be able to be removed easily while it is not affected during the implementation of the all other fabrication steps.

- The structural layer that is used in both support arm and pixel body levels must be stress free in order to avoid buckling. Besides, the thermal conductivity of this layer must be low to obtain desired performance levels.
- The interconnect metal used in the support arms must have low thermal conductivity and high electrical conductivity for the optimum thermal and electrical performance. However, the two are inversely proportional to each other for the metals. Therefore, the material choice is crucial to obtain the optimum performance.
- The active material must be chosen carefully to obtain the desired performance levels. TCR value of the active material must be high while the noise level is as small as possible. Besides, the resistance values must be compatible with the values that the readout circuit is capable of processing.
- The absorber layer must be as close as possible to the value obtained in the absorption simulations.

The proposed process flow starts with the formation of the mirror layer and the routing to the test pads. The first layer of the pixel which is above the mirror layer includes the support arms of the pixel. The second layer of the pixel includes the resistor structure and the pixel body. Figure 3.1 shows the representative 3D views of the proposed process flow.

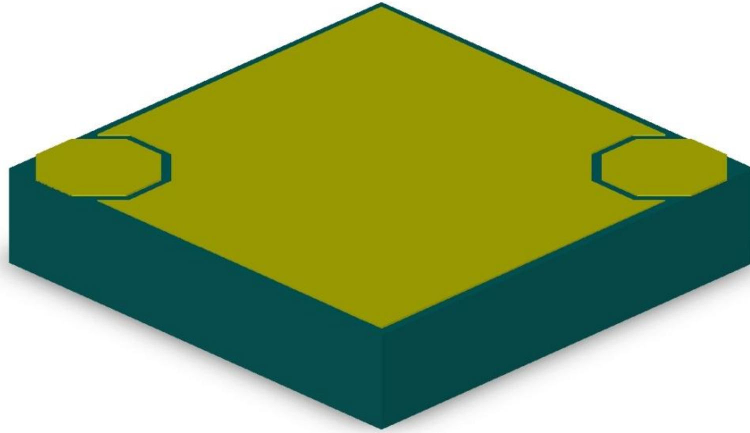

(a) Deposition and patterning of mirror layer.

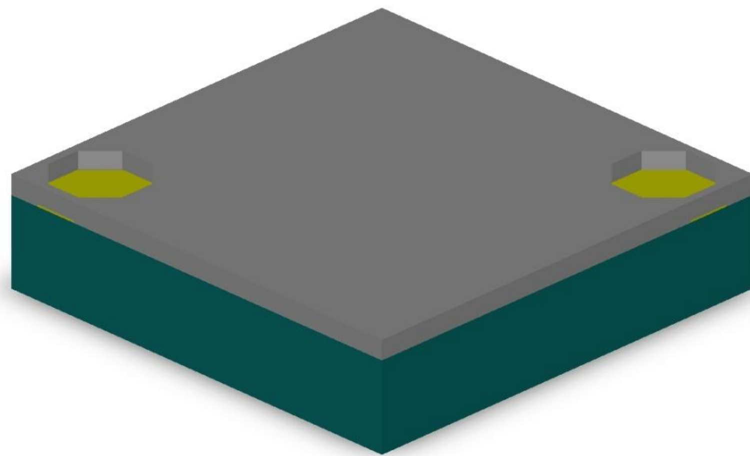

(b) Deposition and patterning of the first sacrificial layer.

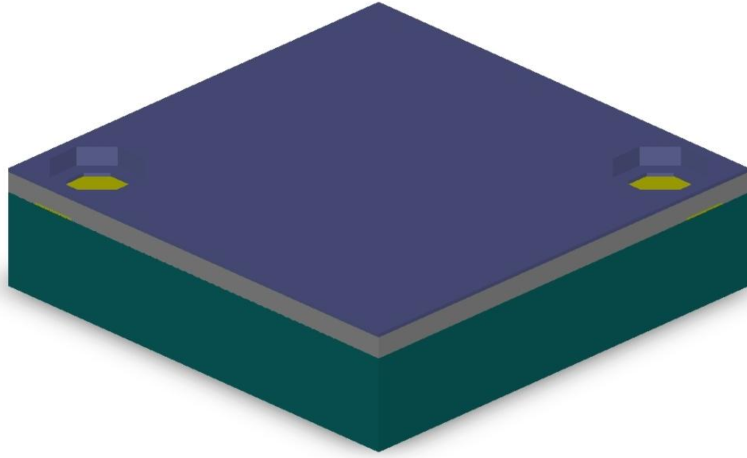

(c) Deposition and patterning of the first nitride layer of the support arms.

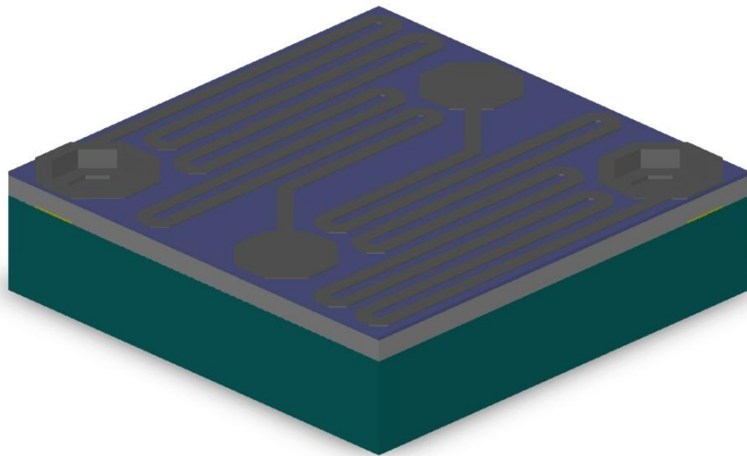

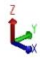

(d) Deposition and patterning of the metal layer of the support arms.

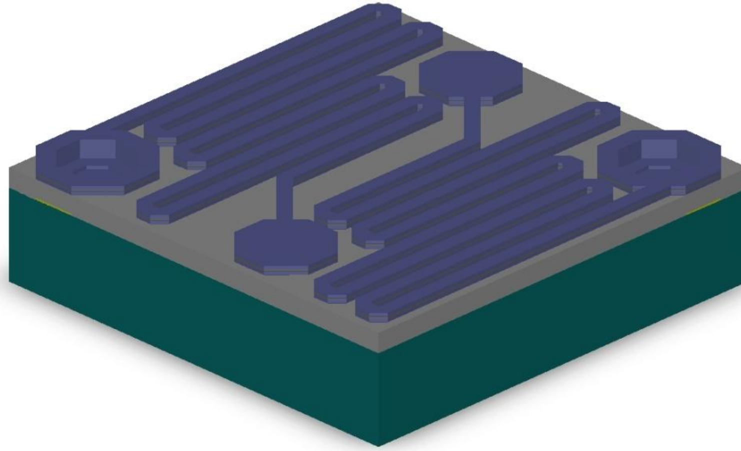

(e) Deposition of the second nitride layer of the support arms and patterning of the nitride layers.

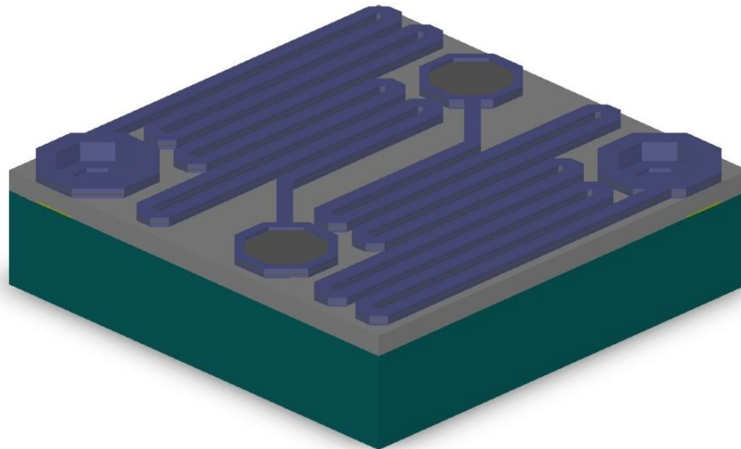

(f) Patterning of the second itride layer of the support arms for contact opening.

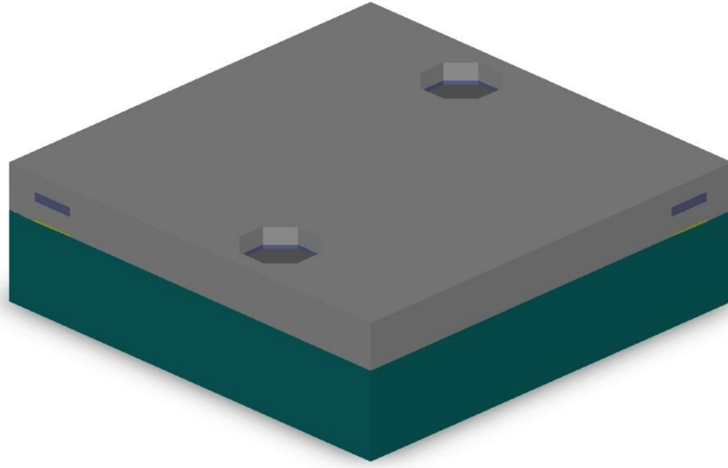

(g) Deposition and patterning of the second sacrificial layer.

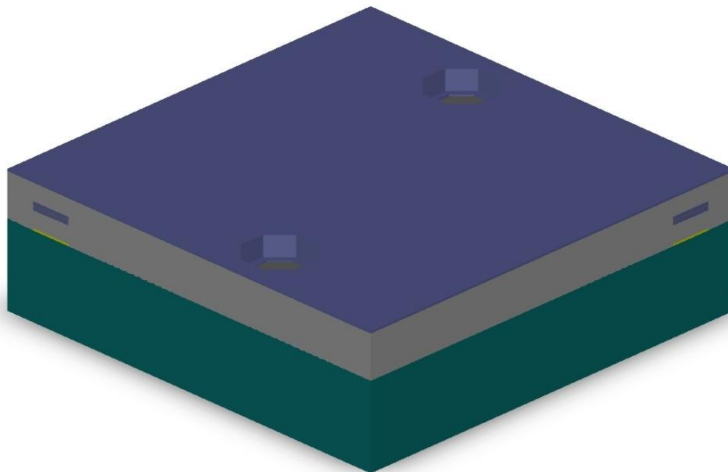

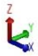

(h) Deposition and patterning of the first nitride layer of the pixel body for contact opening.

(j) Deposition and patterning of the second nitride layer of the pixel body for resistor opening.

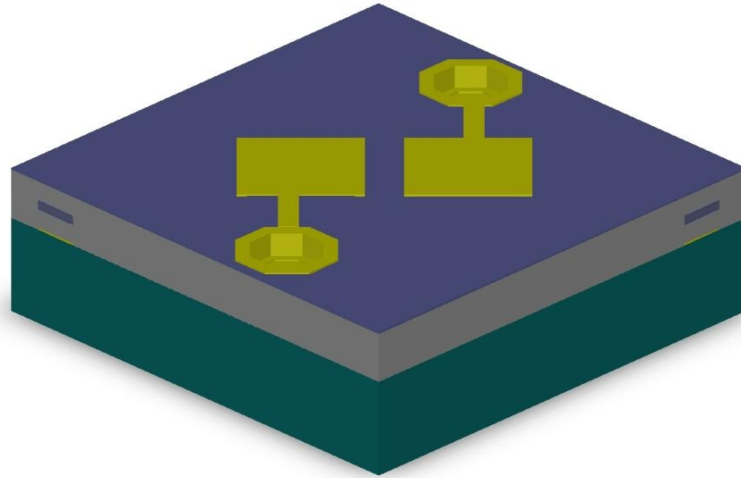

(i) Deposition and patterning of the bottom electrodes.

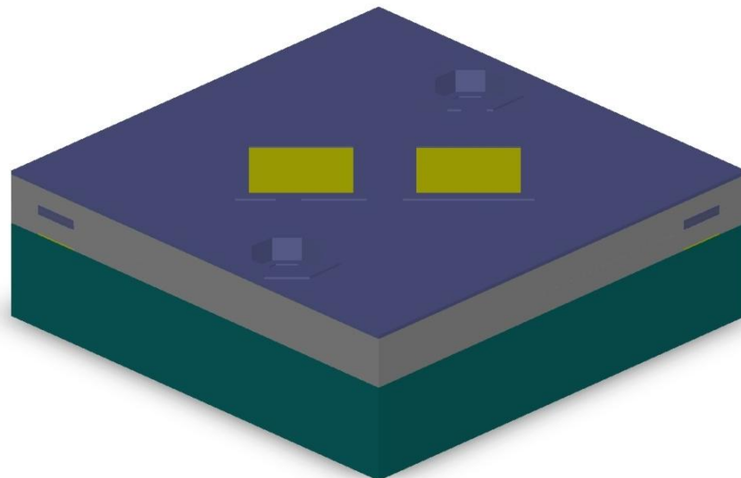

(j) Deposition and patterning of the second nitride layer of the pixel body for resistor opening.

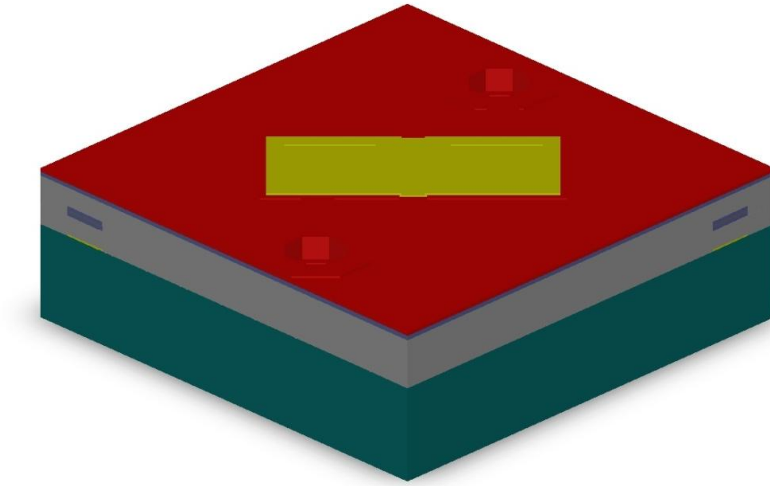

(k) Deposition of the YBCO and top electrode metal layer and patterning of the top electrode.

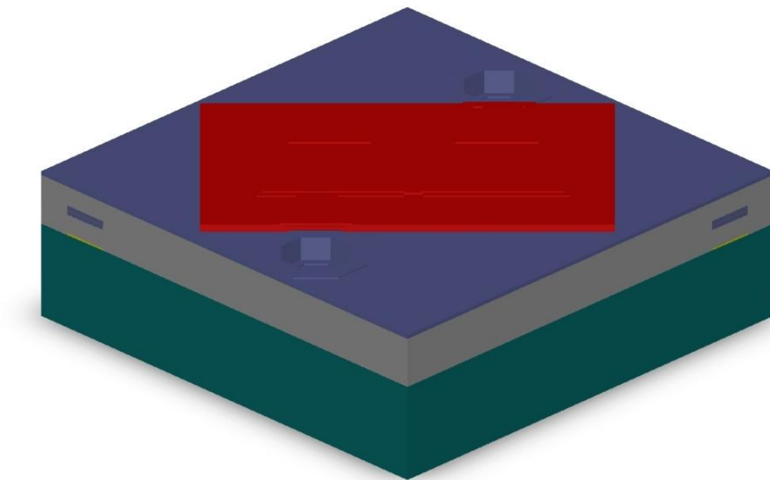

(l) Deposition of the cover YBCO and patterning of the YBCO layer.

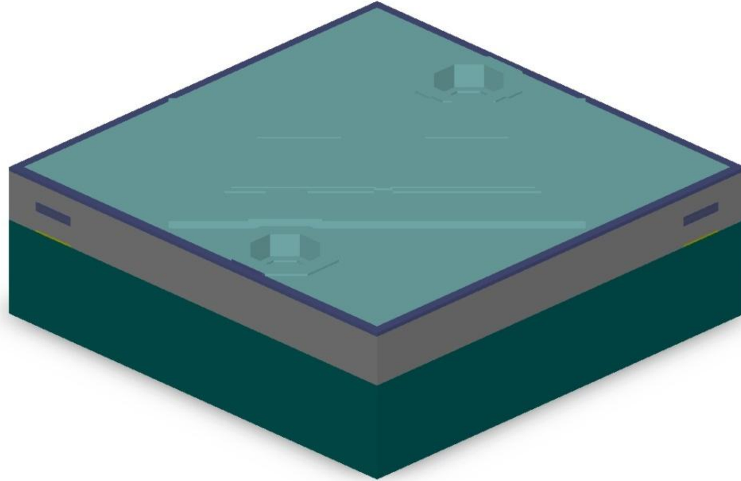

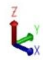

(m) Deposition and patterning of the absorber layer.

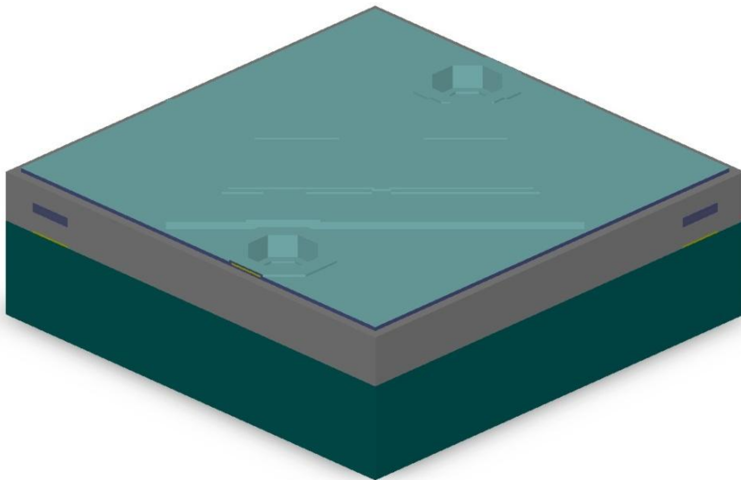

(n) Patterning of the nitride layers of the second level for pixel body formation.

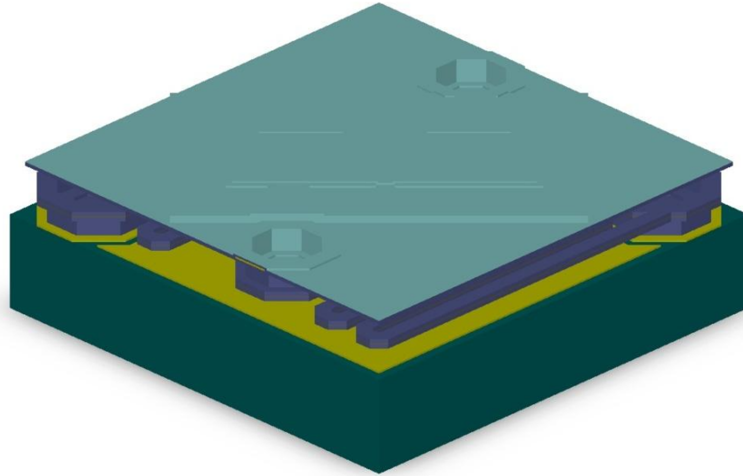

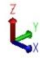

(o) Removal of the sacrificial layer and release of the pixel.

Figure 3.1: Representative 3D views of the process flow.

3.2 Optimization of the Process Steps

After the design of the process flow, the implementation of individual steps must be carried out in order to optimize these steps. Test pixels may be needed to check some of the intermediate steps. Therefore, some test pixels are placed in the design reticles together with the single pixels and array structures. The lithography steps are carried out by a stepper at METU MEMS facilities. The reticles of the stepper in the facility are capable of containing up to 9 different layers depending on the size of the die. The proposed pixels are designed with 14 different lithography steps. Two reticles each having 9 different layers containing the layers for the test steps as well as the main process layers are fabricated at METU MEMS Center by Orhan Akar

and Eren Çanga. Figure 3.2 shows the layout of the die that is composed of the designed pixels, references, test pixels, and array structures.

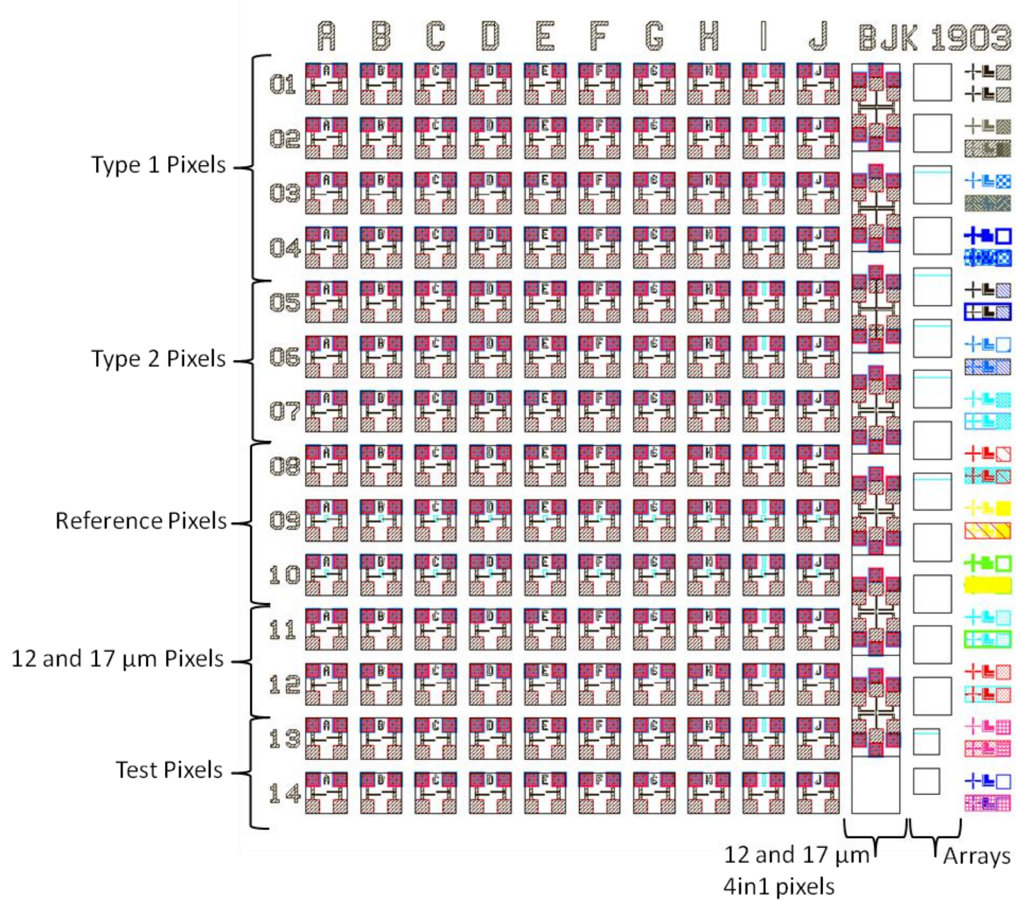

Figure 3.2: Layout of the die containing the pixels, references, test pixels and the arrays.

3.2.1 Mirror Layer

The first step of the process flow is the deposition and patterning of the mirror layer. Although the patterning of the mirror layer is straight forward, it must be carefully handled since the routing of the pixels to the test pads is completed in this layer. Residual photoresist between the anchor and mirror layer may result in short circuit problems. Figure 3.3 (a) and (b) show the photoresist residue between the anchor and mirror layer of the pixels and the short circuit problem as a result of this residue,

respectively. The residue problem is solved by adjusting the exposure energy during the lithography step. Figure 3.4 shows a successfully formed mirror layer of a single pixel.

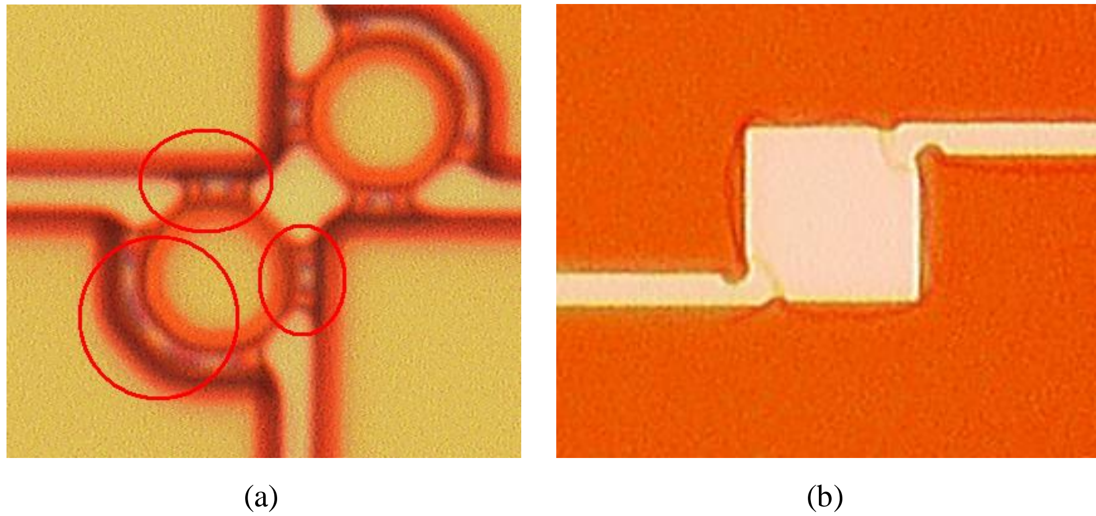

(a) (b)

Figure 3.3: (a)Photoresisit residue between the anchor and mirror layer of the pixels, (b) Short circuit problem as a result of the photoresist residue.

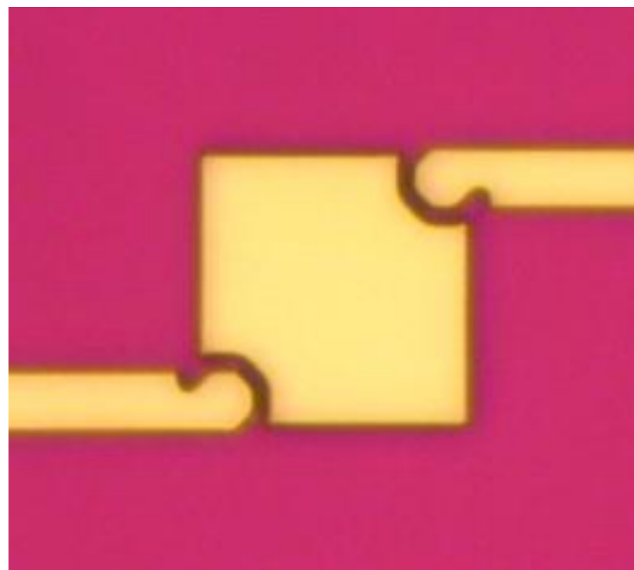

Figure 3.4: Successful mirror formation of a single pixel.

3.2.2 First Sacrificial Layer

The first step in the optimization of the sacrificial layer is the choice of the material. The sacrificial layer must be able to be deposited uniformly. This layer must endure during the other process steps and it must be able to be removed easily during the release of the pixels. The removal of the sacrificial layers is conducted in two different ways: wet etch and dry etch. Wet etch may cause stiction problems because of the capillary forces. Therefore, it is preferred to remove the sacrificial layer using dry etching techniques. Polyimide has been used as the sacrificial layer at METU MEMS facilities in the previous studies [32, 33]. It can be spin-coated uniformly, and it can be removed in O_2 plasma. Therefore, polyimide is used as the sacrificial layer in this study as well.

The second step in the optimization of the sacrificial layer is the thickness optimization. The absorption is simulated and optimized with respect to the thickness of the sacrificial and structural layer thicknesses as explained in Chapter 2. Therefore, it is crucial to obtain the desired sacrificial layer thickness in order to obtain the desired performance. The sacrificial layer thickness of the single level microbolometer pixels fabricated at METU MEMS Center is approximately 2 µm [32], and PI2610 is spin-coated at 2500 rpm to obtain the desired thickness. The first and second sacrificial layer thicknesses of the pixels designed in the scope of this thesis are both 1 µm. PI2556, which is mainly used for processes requiring relatively thin polyimide layers, and PI2610 are used in the optimization trials. Table 3.1 summarizes the thickness optimization trial results conducted using PI2610 and PI2556. Thickness values before and after curing are given in this table. Curing is performed at 300 °C.

Table 3.1. Summary of the thickness optimization trials conducted using PI2610 and PI2556.

	Thickness before curing	Thickness after curing
PI2610 @6000 rpm	1200 nm	1000 nm
PI2610 @7000 rpm	1080 nm	850 nm
PI2556 @3500 rpm	1520 nm	1160 nm
PI2556 @4000 rpm	1310 nm	1070 nm

It is observed that the sacrificial layer can be coated using both PI2610 and PI2556 in consideration of the results summarized in Table 3.1. However, it is observed that the surface of PI2610 polyimide is rough when it is spin coated relatively thinner. Figure 3.5 shows the surface roughness of the PI2610 in an SEM image. The SEM image shows the support arms of a pixel whose sacrificial layer is formed using PI2610. The dots seen on the field are the result of the surface roughness of PI2610.

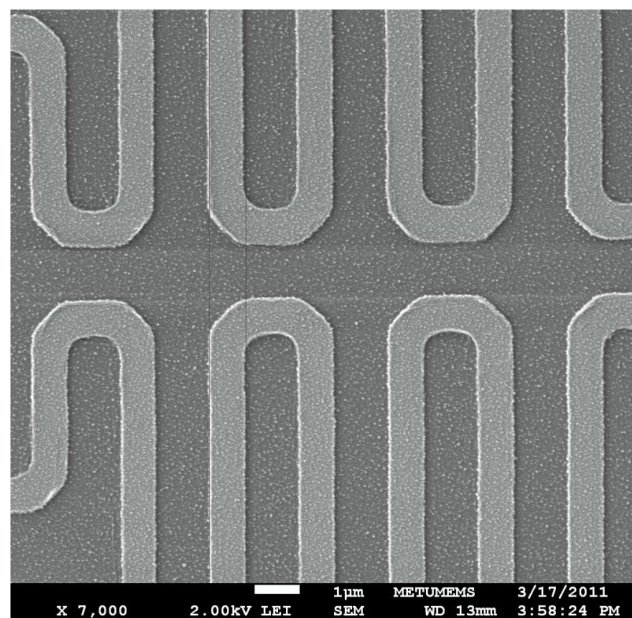

Figure 3.5: SEM image of the support arms of a pixel. PI2610 is used as the sacrificial layer in this pixel, and the dots on the field are the result of surface roughness of PI2610.

The last concern about the optimization of the polyimide is the etching step. O_2 plasma is used to etch the polyimide layer in an RIE chamber, but O_2 plasma also etches the photoresist layers. Therefore, the process must be carefully handled in order to prevent the etching of the polyimide more than desired amount. One way to prevent the undesired etching is to use thick photoresist layers that would not be etched completely during the RIE process of the polyimide. Another way is to cover the polyimide with a material that is resistant to O_2 plasma. This material protects the polyimide even if the photoresist is completely etched away. Titanium is a hard material that stands in the RIE step for the formation of the polyimide openings. It has been used in the polyimide RIE steps at METU MEMS facilities in previous studies [34]. However, titanium is oxidized if it is exposed to O_2 plasma for relatively long times, and the stripping of the titanium layer gets difficult, sometimes impossible. As a result, titanium particles might be left even after the strip of this layer, especially near the anchors openings, since the photoresist is removed faster at the edges. Figure 3.6 shows an SEM image of a pixel with the polyimide openings for the anchors. It is observed that there are titanium particles left in the field, especially near the anchor openings. Therefore, the photoresist is made thicker, and then it is observed that it can stand the polyimide RIE. Since the polyimide layer is relatively thinner, 1 μm, with respect to the previous studies SPR220-3 can stand the polyimide RIE, which is 25-minute-long.

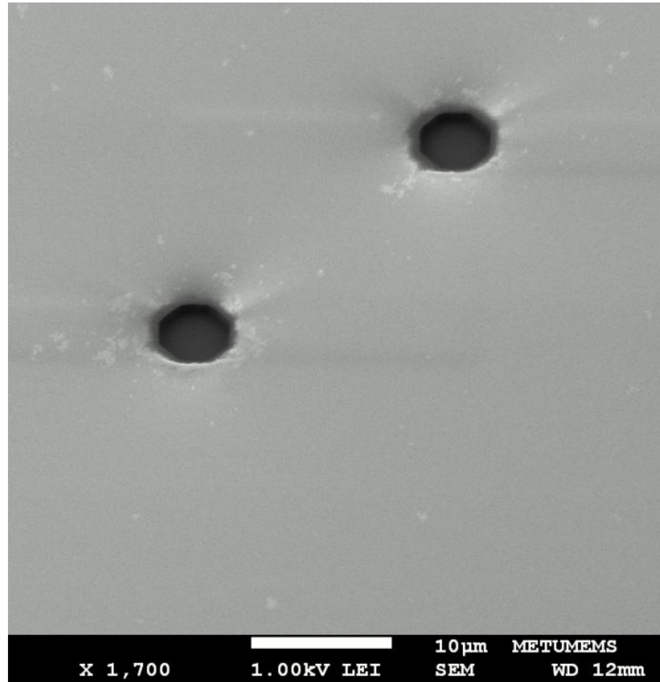

Figure 3.6: SEM image of a pixel with the polyimide openings for the anchors. After the strip of the titanium there are some titanium particles left near the anchor openings.

3.2.3 First Structural Layer

The structural layer is used in the both support arms and the pixel body. Therefore, it must be stress free to prevent problems arising from the buckling while having a relatively low thermal conductance value in order not to limit the performance of the pixel. Silicon nitride (Si_3N_4) is the best candidate for the structural layer selection at METU MEMS facility since the facility has the capability of stress free nitride deposition. Besides, the thermal conductance of silicon nitride value is very small when compared to the titanium layer which is used in the support arms as the contact material. The first etch step of the structural layer is the contact opening inside the anchors. The anchors differ with respect to the opening sizes in the pixels designed in this study. Figure 3.7 shows layouts of three different anchor structures. The inner most octagon is drawn for the opening of the structural layer while the outer most one is for the contact metal formed with the mirror layer. The octagon in

between these two is used for the opening of the sacrificial layer. All three opening areas are successfully etched in the anchor opening of the structural layer step.

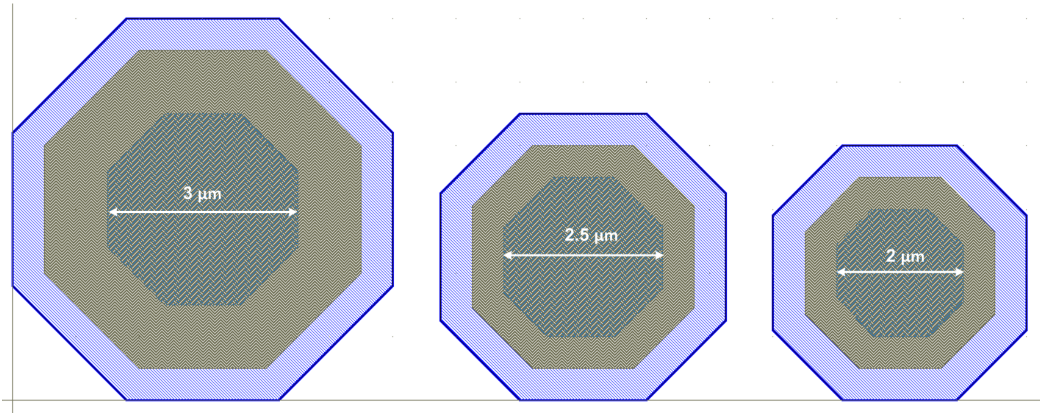

Figure 3.7: Layouts of different anchor structures. The inner most octagon is the opening of the structural layer.

Test pixels are designed with the widest anchor openings to prevent the problems in the patterning of the anchor openings. Figure 3.8 shows an SEM image of a pixel with 3 µm anchor opening of the first structural layer. The contact metal is under the polyimide layer so it is not seen in the SEM image. Figure 3.9 shows an SEM image of a 2 µm structural layer opening. It is observed that it is possible to pattern the structural layer with a width of 2 µm in METU MEMS facility. Therefore, the size of the anchors of the pixels can be decreased.

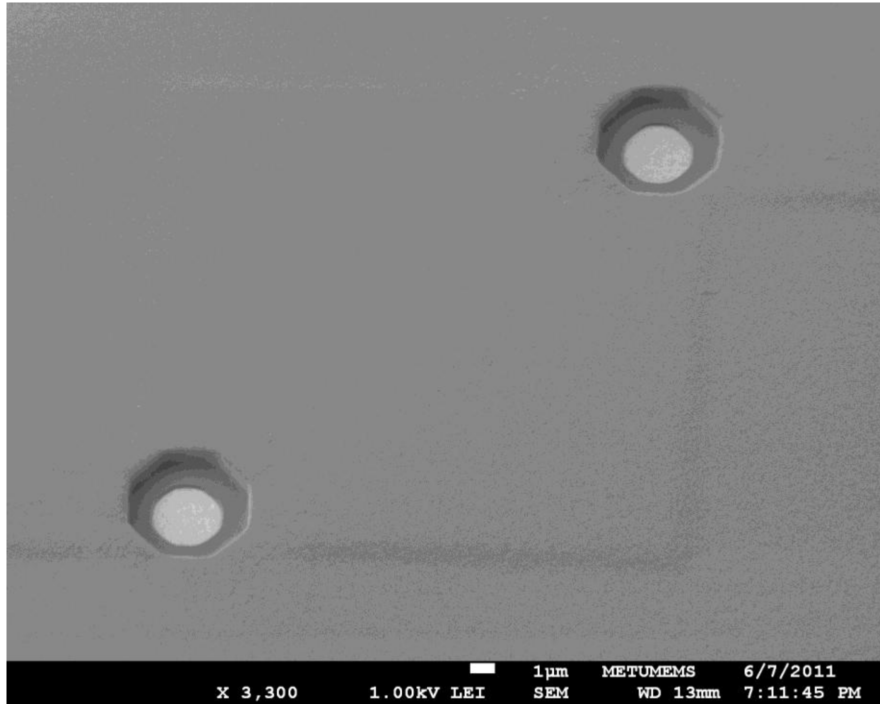

Figure 3.8: SEM image of a pixel with the anchor opening of the first structural layer.

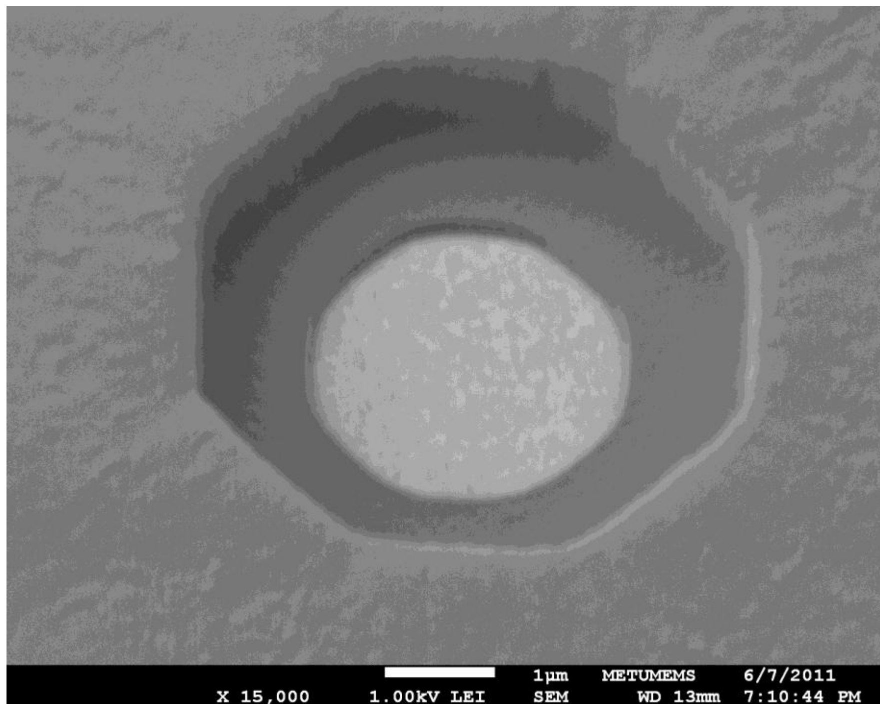

Figure 3.9: SEM image of 2 μm structural layer opening.

3.2.4 Formation of the Metal Layer of the Support Arms

The thermal conductance is the most important structural parameter when the NETD of the detector is taken into account. The metal layer of the support arms has the most dominant contribution to the thermal conductance since the thermal conductance values of the metals are higher when compared to the structural and active materials used in the pixel fabrication. The contributions of the absorber layer and the electrode materials on the thermal conductance are relatively small. Table 3.2 shows the thermal conductance values of the structural and active materials together with the metal layer of the support arms.

Table 3.2: Thermal conductance values of the structural and active materials together with the metal layer of the support arms.

	Si_3N_4	YBCO	Ti
Thermal Conductance (W/cmK)	0.01	0.035	0.219

In order to decrease the thermal conductance of the pixels for better thermal isolation, the support arms are designed to be thin and long as explained in Chapter 2. The low thermal conductance is also made possible by the proper selection of the metal layer in the support arms. As explained in Section 3.1, a metal with low thermal conductance must be selected while also taking the electrical resistivity of the material into account. Table 3.3 indicates the thermal conductance values of some of the metals. NiCr has the lowest thermal conductance value among these, 0.113 W/cmK. Titanium has the closest value to NiCr with the value of 0.219 W/cmK. Although NiCr has lower thermal conductance, the electrical resistivity of NiCr, which is 1.1 μΩ-m, is higher than the resistivity of titanium, 0.42 μΩ-m. Moreover, decreasing the thermal conductance as much as possible is

not the only concern regarding the performance of the detectors. Thermal time constant, which is inversely proportional to the thermal conductance, is another parameter that should be taken into account as explained in Chapter 1. As a result, titanium is chosen as the metal layer of the support arms in order to optimize the performance considering the electrical conduction, the thermal isolation, and the time constant of the detectors.

Table 3.3: Thermal conductance values of some of the metals.

	Al	Au	Cr	Cu	Ni	NiCr	Ti
Thermal Conductance (W/cmK)	2.37	3.2	0.939	4.01	0.909	0.113	0.219

The next step in the optimization of the metal layer of the support arms is the etching process. Although the minimum feature size of the support arms is in agreement with the capabilities of the METU MEMS facility, the process must be carried out with a careful treatment to fabricate the minimum size features. There are also support arms with the safety margins in case the support arms with the minimum feature size cannot be fabricated. The first optimization considering the etching process is the photolithography step. The first problem encountered in this step is the undeveloped photoresist between the support arms. Figure 3.10 shows two SEM images of unsuccessful photolithography trials for the support arms. This problem could not be solved by altering the exposure energy indicating that exposure focus optimization is required. Since the alignment mark of the stepper and the photoresist to be exposed are not on the same level, the focus of the exposure must be optimized to obtain the desired structures. The optimum energy and exposure values are obtained by varying both of them in the stepper. Figure 3.11 indicates an SEM image of a successful photolithography trial for the support arm.

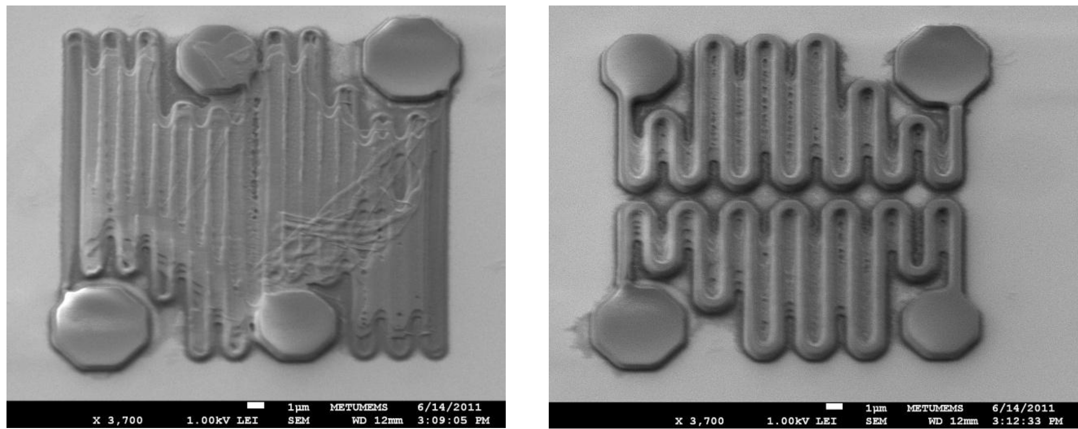

Figure 3.10: SEM images of two unsuccessful photolithography trials for the support arm.

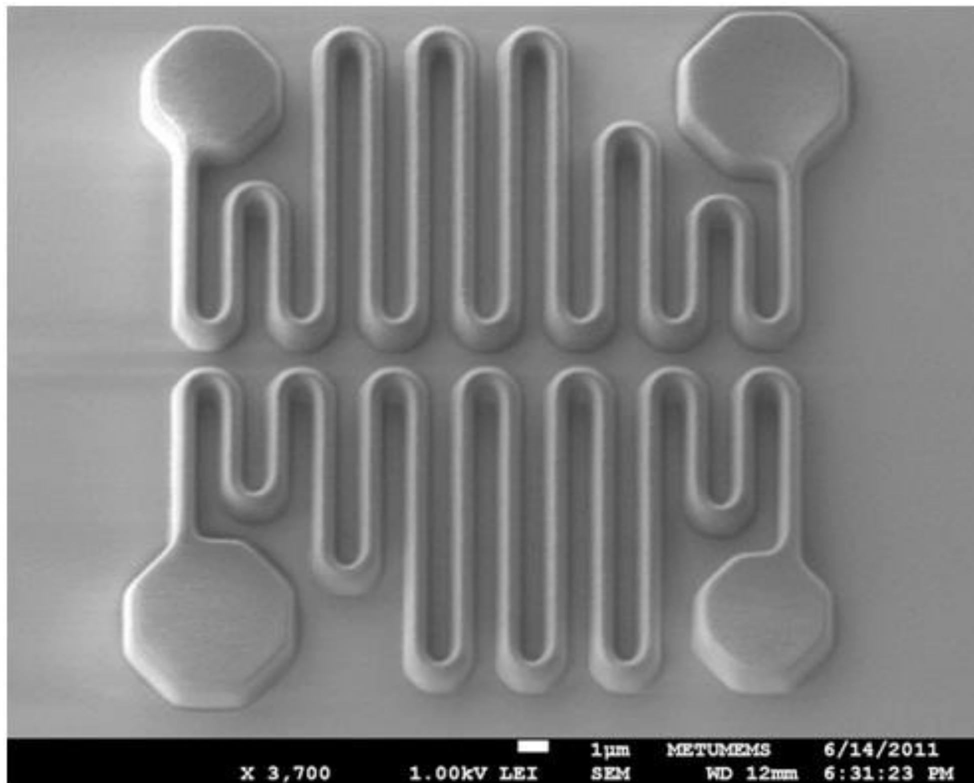

Figure 3.11: SEM image of a successful photolithography trial for the support arm.

Another problem encountered in the photolithography step is the standing wave effect. Standing wave effect results from the interference of the light falling on the

substrate and the light reflected from the substrate. This effect causes the edges of the photoresist layer to be formed in a stair-like manner. Figure 3.12 shows the standing wave effect on the photoresist. The dry etch method, metal RIE, is used to fabricate the metal layer of the support arms since the minimum feature size of 0.5 μm cannot be formed using wet etchants. The metal RIE processes have low selectivity on the photoresist. Therefore, the photoresist on the edges is etched before the process is completed if the standing wave effect causes stair-like formation in the photoresist.

Figure 3.13 shows an SEM image of the metal layer of the support arms after metal RIE process. Photoresist is removed after the MRIE process is completed. The standing wave effect causes the photoresist on the edges to be etched away before the process is completed, and the edges of the arm metal get thinner. Then, the thin part of the arm metal is lifted off, and gets stuck on the thick part of the arm metal.

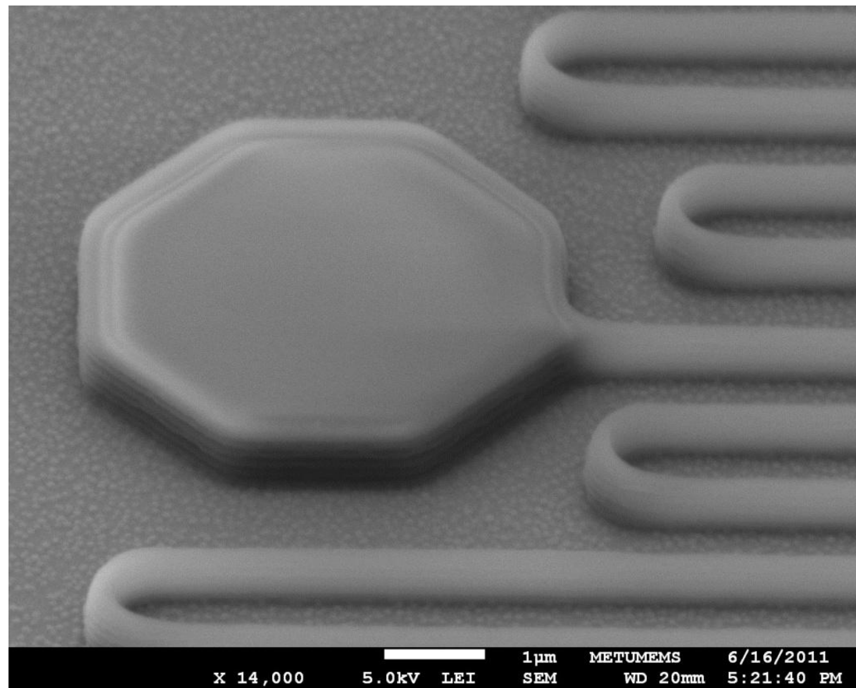

Figure 3.12: SEM image showing the standing wave effect on the photoresist.

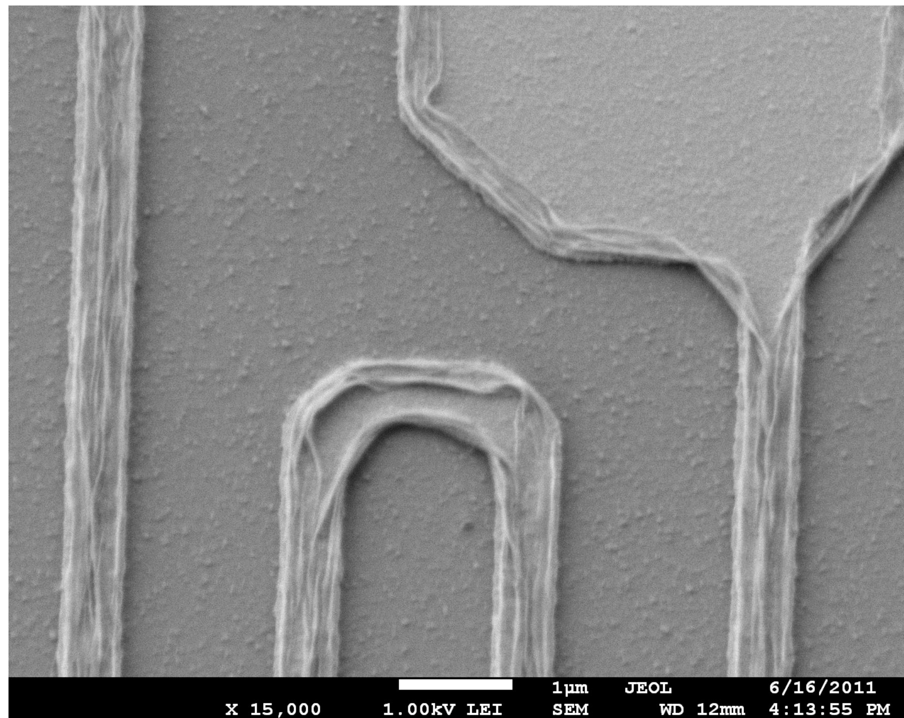

Figure 3.13: SEM image of the metal layer of the support arms after metal RIE process. Photoresist is removed after the MRIE process. The standing wave effect causes photoresist on the edges to be etched away before the process is completed, and the edges of the arm metal get thinner.

It is observed that the standing wave effect depends on the photoresist type. In other words, some photoresist types are affected more by standing wave effect than others. Therefore, the type of photoresist used in the lithography step for the support arm metal is changed. Then, the energy and focus values of the exposure are optimized for the chosen photoresist, S1805.

Figure 3.14 shows an SEM image after a successful photolithography for the etch of the support arm metal while Figure 3.15 indicates an SEM of a metal layer of two support arms after the MRIE process.

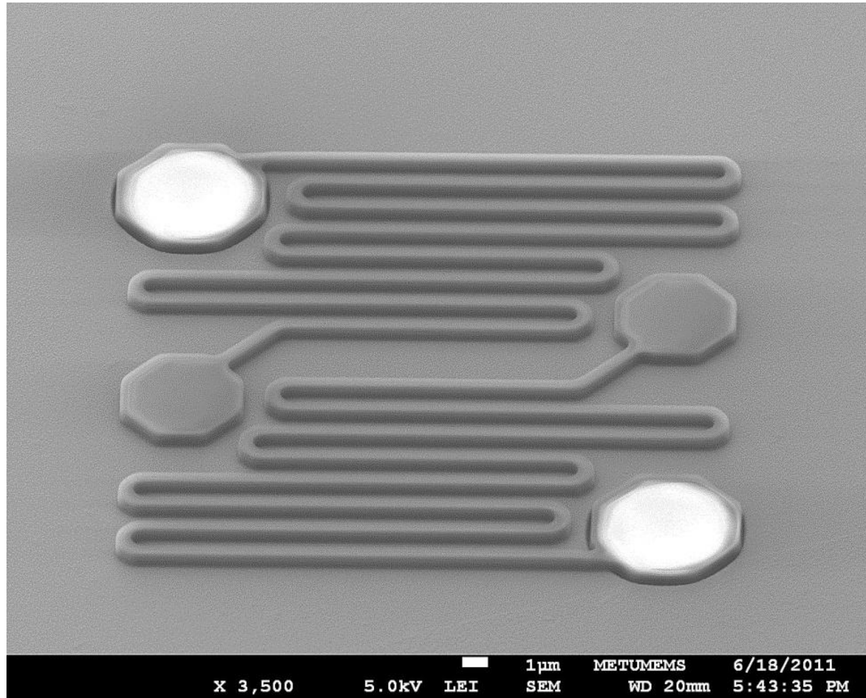

Figure 3.14: SEM image after a successful photolithography for the etch of the support arm metal.

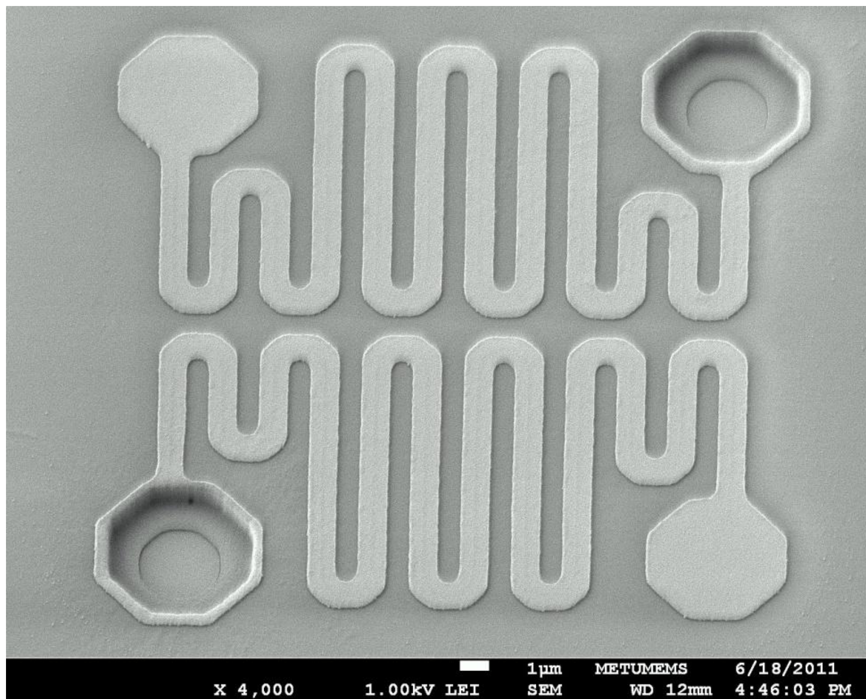

Figure 3.15: SEM image of metal layer of two support arms after MRIE process.

3.2.5 Contact Opening for the Second Structural Layer of the Arms

The structural layer is selected as Si_3N_4 as explained in Section 3.2.3. The second structural layer of the support arms is deposited after the formation of the support arm metal. Then, the contact openings for the anchors connecting the support arms and the second level of the pixel are formed. Figure 3.16 shows an SEM image of the contact openings for the anchors connecting the first and second levels.

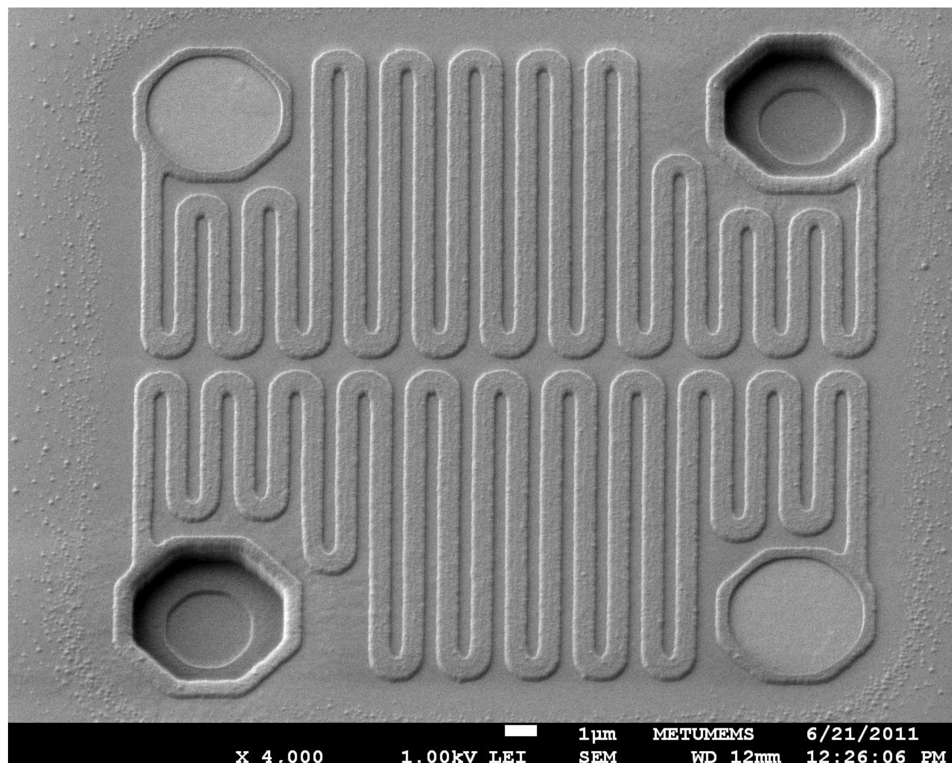

Figure 3.16: SEM image of the contact openings for the anchors connecting the first and second levels.

3.2.6 Structural Layer Formation of the Support Arms

The support arms are composed of two layers of structural material covering the metal layer in between. These two layers are formed for the mechanical stability of the arms. The structural layer of the support arms has the minimum feature size equal to that of metal layer of the arms. Therefore, attention must be paid on the lithography and etch steps. The optimum energy and focus offset values of the exposure changes as the layers are established, i.e., as the height from the substrate gets larger. Optimization of these values is necessary for all of the following steps.

The formation of the support arms is carried out by dry etching, in RIE system. S1813 has been used as the photoresist for the nitride RIE processes in earlier studies at METU MEMS Center [34]. However, it is observed that this photoresist is not suitable for the support arm formation in this study. This photoresist has an angled shape resulting in the thinner photoresist layer at the edges. This phenomenon causes etching of the photoresist at the edges before the process is completed just like the case of standing wave effect. Then, sidewalls at the edges are formed after the nitride RIE process. Figure 3.17 shows an SEM image of the support arm lithography conducted using S1813. Figure 3.18 shows an SEM image of a support arm with sidewalls after nitride RIE.

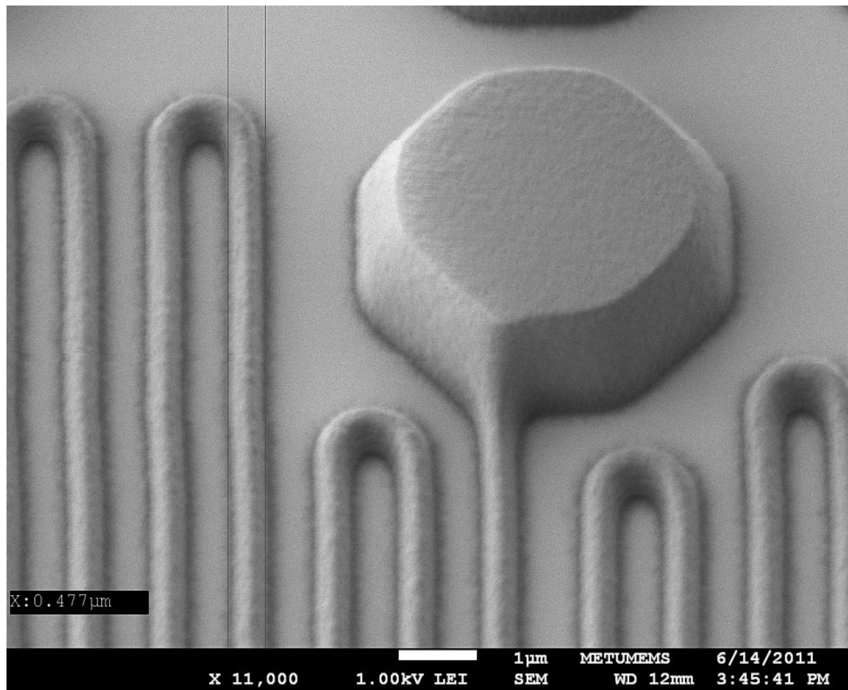

Figure 3.17: SEM image of the support arm lithography using S1813

.

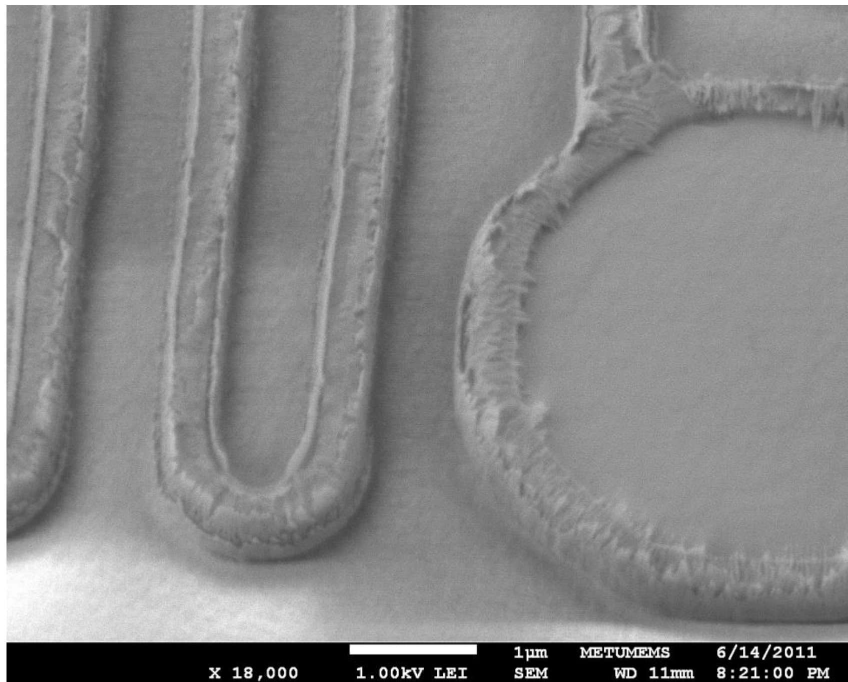

Figure 3.18: SEM image of a support arm with sidewalls after nitride RIE.

It is observed in the lithography step of the arm metal that S1805 is better than S1813 at the lithography of smaller dimensions such as 0.5 μm. Therefore, the formation of the support arms is carried out by using S1805 in the lithography step. Figure 3.19 shows an SEM image of the support arm lithography conducted by using S1805.

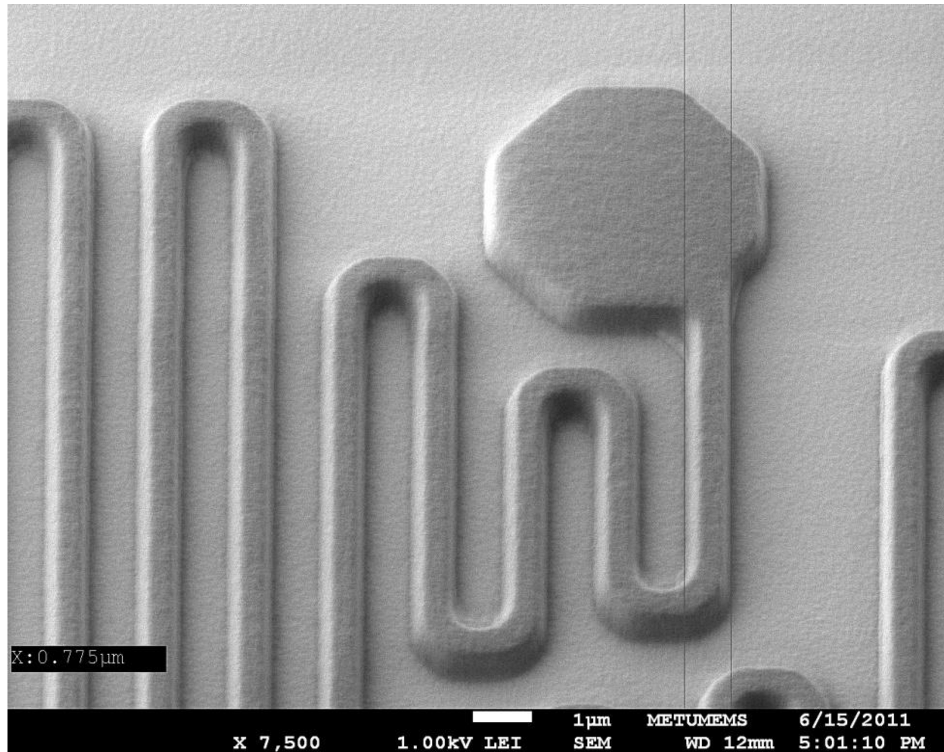

Figure 3.19: SEM image of the support arm lithography conducted by using S1805.

Another problem encountered during the optimization of the support arm formation is the photoresist removal. The chemical compound of the photoresist changes when it is exposed to plasma formed from fluorine (F) based gases. Therefore, the removal of the photoresist gets more difficult such that it cannot be removed in acetone. The photoresist removal after nitride RIE has been conducted by O_2 plasma in the earlier studies at METU MEMS Center [34]. However, the polyimide layer becomes visible after the formation of the support arms in the case of two-level microbolometer pixel. Therefore, the polyimide is also exposed to O_2 plasma if the photoresist is removed

in this plasma. Some other methods are tried to remove the photoresist after the nitride RIE process step. The first method is the removal of the photoresist in PRS1000 solution. It is observed that PRS1000 does not attack polyimide layers. However, it cannot strip the photoresist layer completely. Figure 3.20 shows an SEM image of the support arms after photoresist strip trial in PRS1000 solution at 80 °C. The second method which is tried for the removal of the photoresist is using EKC265 solution. The photoresist is completely stripped after holding the wafer in EKC for 30 minutes. However, EKC attacks the polyimide which results in the suspension of the support arms. Figure 3.21 shows an SEM image of the support arms after holding the wafer in EKC solution for 30 minutes. A relatively thin polyimide layer under the support arms is etched. The support arms are suspended, and then stuck to the remaining polyimide layer. The buckling in the support arms can be seen in the figure.

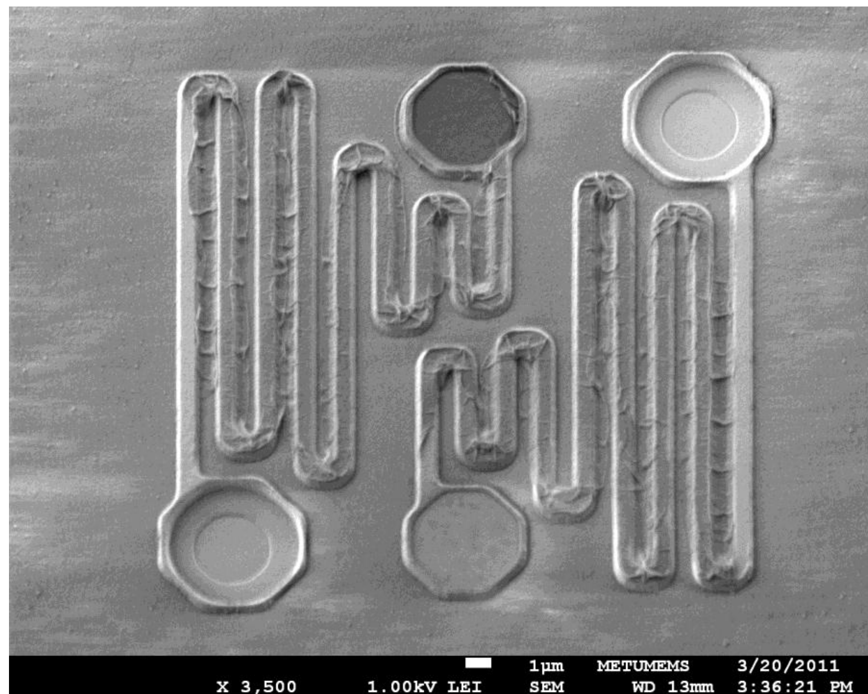

Figure 3.20: SEM image of the support arms after the PR strip trial in PRS1000.

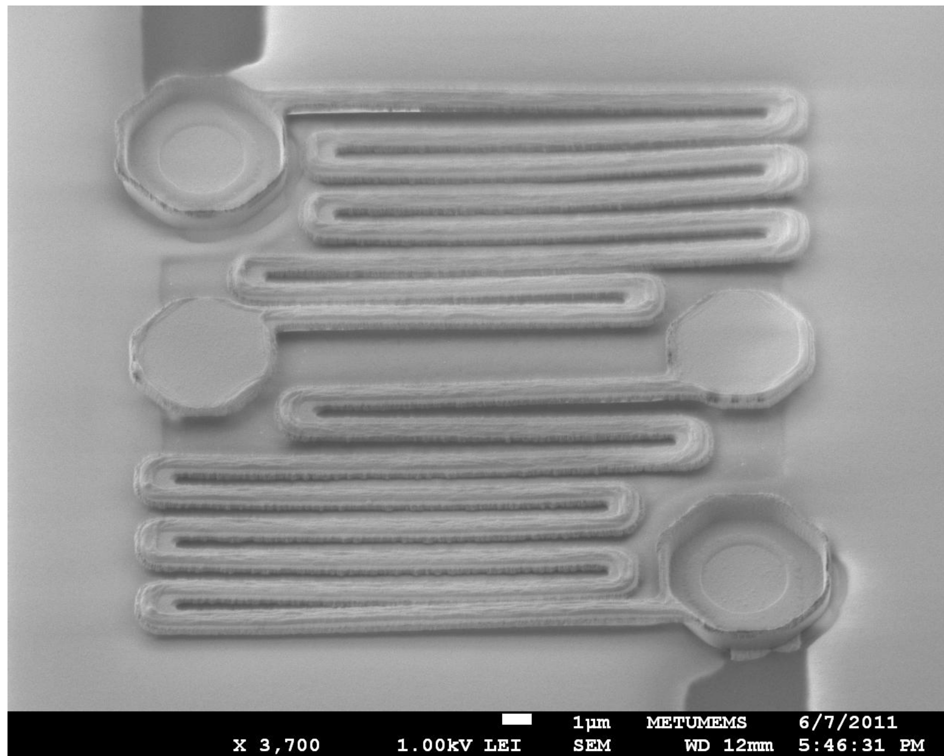

Figure 3.21: SEM image of the support arms after holding the wafer in EKC solution for 30 minutes.

Another method carried out to remove the photoresist is holding the wafer in O_2 plasma for a very short time, like 2 or 3 minutes. This may remove the photoresist on the surface which is exposed to the plasma. Then, holding the wafer in EKC solution for a shorter time might remove the photoresist without attacking the polyimide layer too much. A wafer with the support arms formed by nitride RIE is held in O_2 plasma for 2 minutes. Then, it is held in EKC solution for 10 minutes. The photoresist is completely removed. However, polyimide layer is etched more than the previous method. Figure 3.22 shows an SEM image of an anchor and a support arm after holding the process wafer in O_2 plasma for 2 minutes and in EKC solution for 10 minutes.

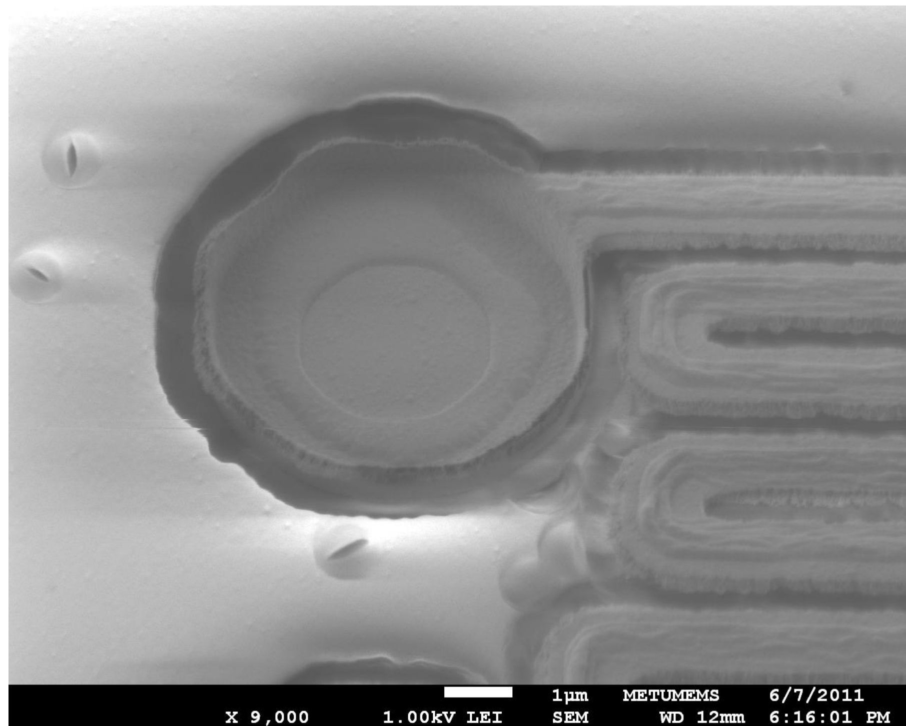

Figure 3.22: SEM image of an anchor and a support arm after holding the process wafer in O_2 plasma for 2 minutes and in EKC solution for 10 minutes.

The last method performed is holding the process wafer in O_2 plasma for 2 minutes just after the nitride RIE process. This may remove the photoresist on the surface which is exposed to the plasma like in the previous case. Then, the wafer is held in PRS1000 solution at 80 °C for 30 minutes. The photoresist is completely removed with almost no etching of the polyimide layer. Figure 3.23 indicates an SEM image of an anchor and a support arm after holding the process wafer in O_2 plasma for 2 minutes, and then in PRS1000 solution for 30 minutes. It is observed that there is no photoresist left, and the polyimide layer under the support arms is intact.

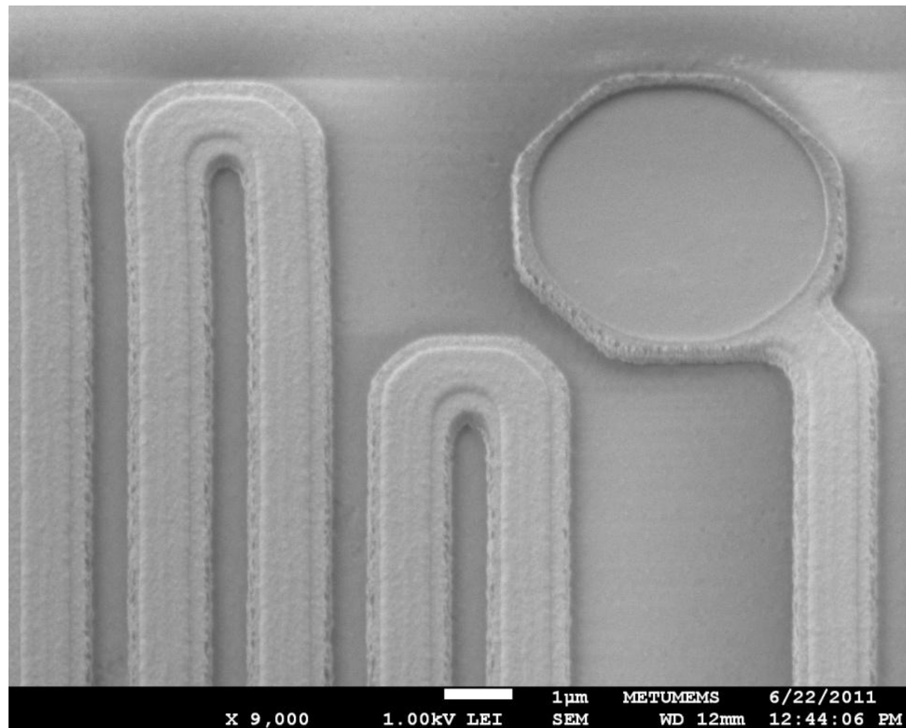

Figure 3.23: SEM image of an anchor and a support arm after holding the process wafer in O_2 plasma for 2 minutes, and then in PRS1000 solution for 30 minutes.

3.2.7 Second Sacrificial Layer

The second sacrificial layer is spin-coated after the formation of the support arms. Since the thickness of the second sacrificial layer is equal to that of the first one, there is no need to optimize the thickness again. The key point in this step is to adjust the time of the polyimide RIE for the formation of the anchors connecting the support arms to the second level. Contact opening for these anchors is explained in Section 3.2.5. The polyimide opening areas are placed in the middle of these contact openings. If the process continues even after the etching of the polyimide is completed, the titanium is exposed to the O_2 plasma in RIE chamber. The oxidation of the titanium layer may cause contact problems with the bottom electrodes of the resistor structure. Therefore, the polyimide RIE process is divided into a number of short process steps to obtain the time duration at which the polyimide is completely

etched. It is observed that the polyimide RIE is completed in 25 minutes. Figure 3.24 shows an SEM image of a completed polyimide opening for the anchor formation to connect the first and second levels.

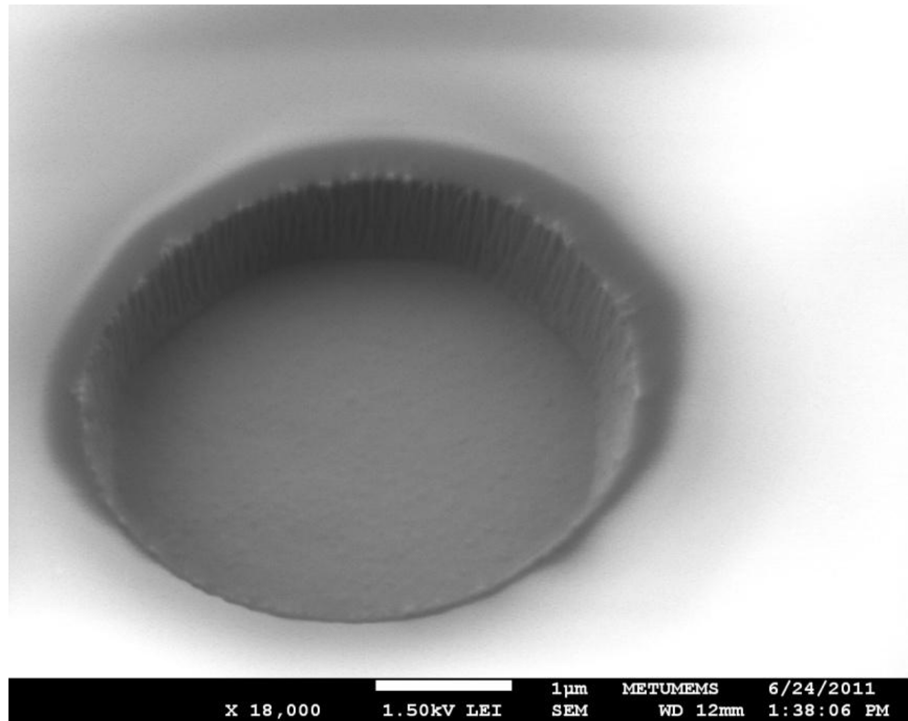

Figure 3.24: SEM of a polyimide opening for the anchor formation to connect the first and second levels.

3.2.8 First Structural Layer of the Second Level

The first structural layer of the second level is deposited after the patterning of the second sacrificial layer. The contact openings for the anchors are formed in the middle of the polyimide openings. Figure 3.25 shows an SEM image of a contact opening for the anchor connecting the first and second levels.

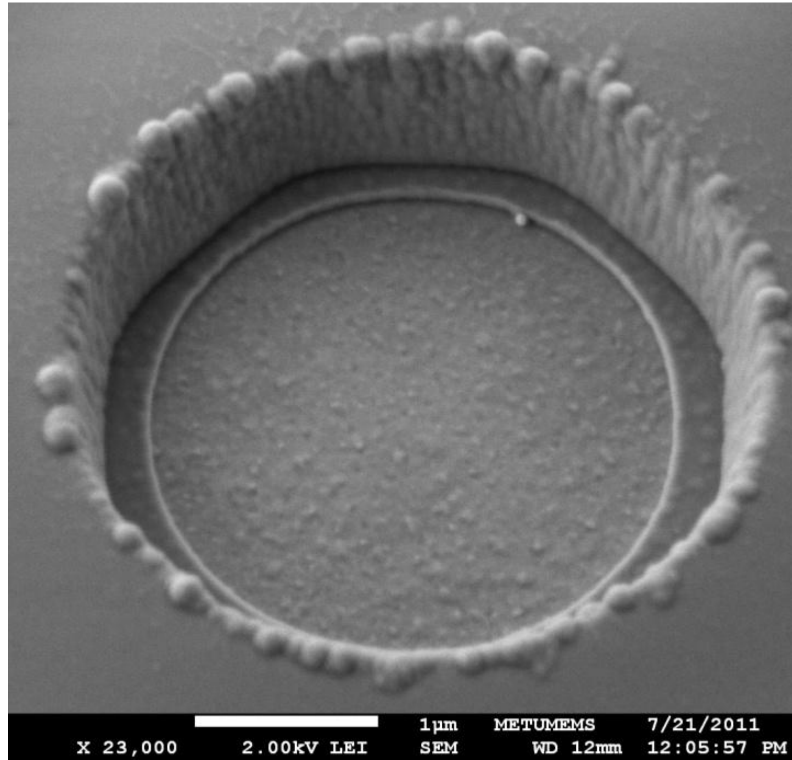

Figure 3.25: SEM image of a contact opening for the anchor connecting the first and second levels.

3.2.9 Formation of the Bottom Electrodes

The bottom electrode is the first step of the resistor structure. A Cr/Au layer stack is used to form the bottom electrodes. Although these electrodes are designed with the safety margins, the process must be handled cautiously since the topology underneath may cause problems in the lithography and etching steps. The thickness of this layer must be adjusted high enough to obtain well-established step coverage in the anchor openings. On the other hand, it must be kept in mind that the etching of this layer is carried out by wet etching technique which may cause undesired undercut levels for relatively thick layers. Therefore, the thickness must be optimized to meet both the step coverage requirement and the undercut margin. Figure 3.26 indicates an SEM image of a bottom electrode. The step coverage inside the anchor is shown in this figure.

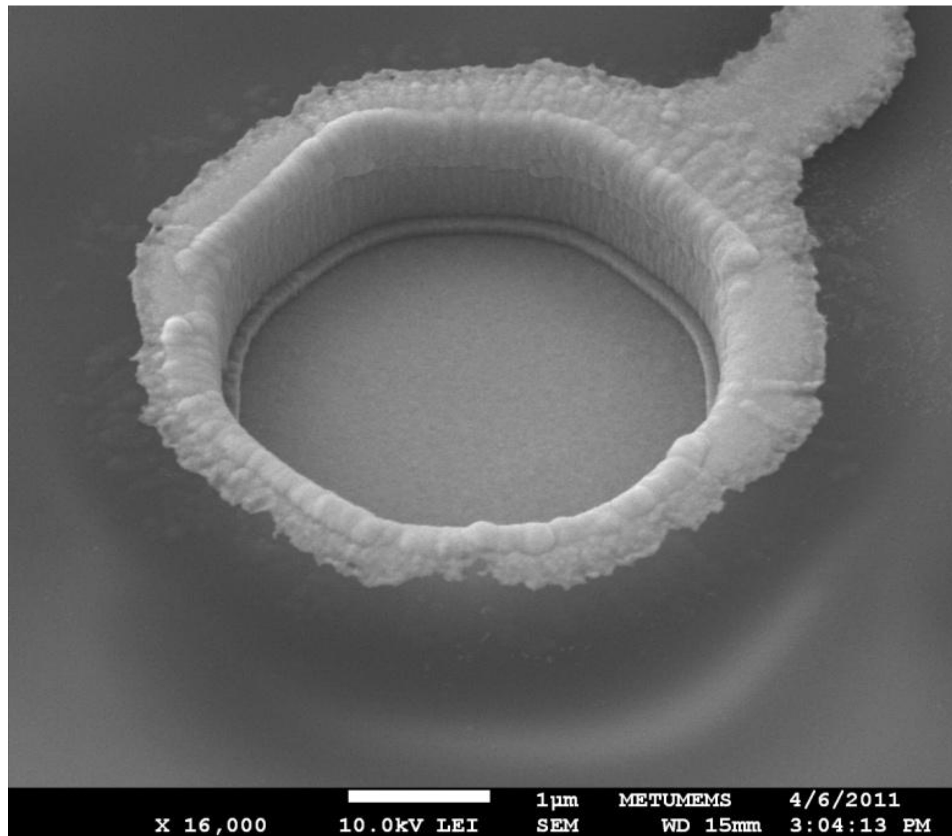

Figure 3.26: SEM image of a bottom electrode. The step coverage inside the anchor is good enough.

Figure 3.27 shows an SEM image of a bottom electrode pair. There are gold and chromium particles left in the pixel body just above the anchors of the first level. These particles are caused by the lithography problem due to the topology. These particles have almost no effect on the performance of the pixel. Therefore, the rest of the processes are also completed for this wafer. However, the problem must be solved by the optimization of a CMP process for the second sacrificial layer.

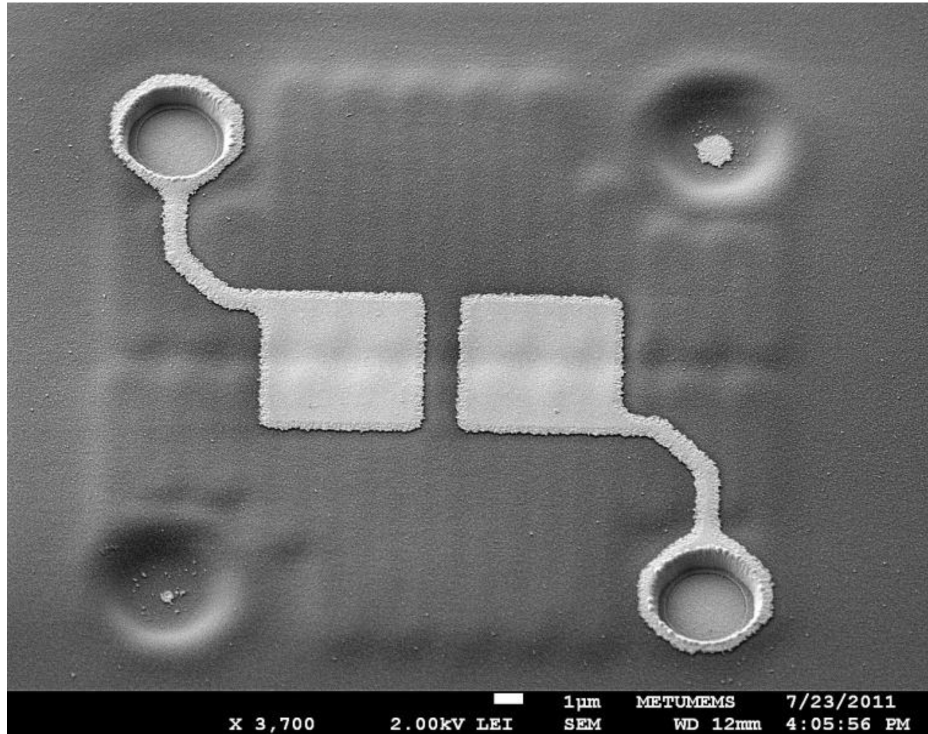

Figure 3.27: SEM image of a bottom electrode pair.

3.2.10 Resistor Openings in the Second Structural Layer of the Second Level

The last structural layer is deposited on the bottom electrodes. Then, this structural layer is etched in order to get contact from the bottom electrodes to the active material. The optimization of the nitride RIE has been conducted in the previous steps. There is no additional optimization conducted for this layer. Figure 3.28 shows an SEM image of the resistor openings above the bottom electrodes.

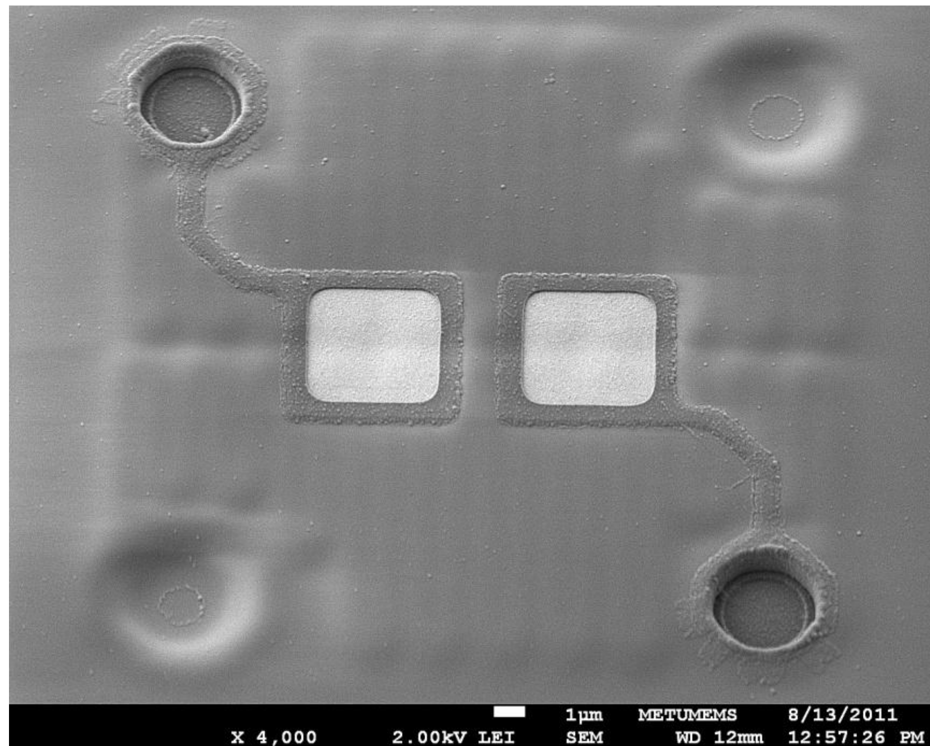

Figure 3.28: SEM image of the resistor openings above the bottom electrodes.

3.2.11 Active Material and Top Electrode Deposition

After the formation of the resistor openings, the active material, YBCO, and the top electrode layer stack, Au/Ti are sputtered consecutively for in situ deposition. The top electrode is formed using the inverse sputtering method. The etch step of the YBCO is performed after the cover YBCO deposition. Figure 3.29 shows an SEM image of a top electrode on the YBCO layer

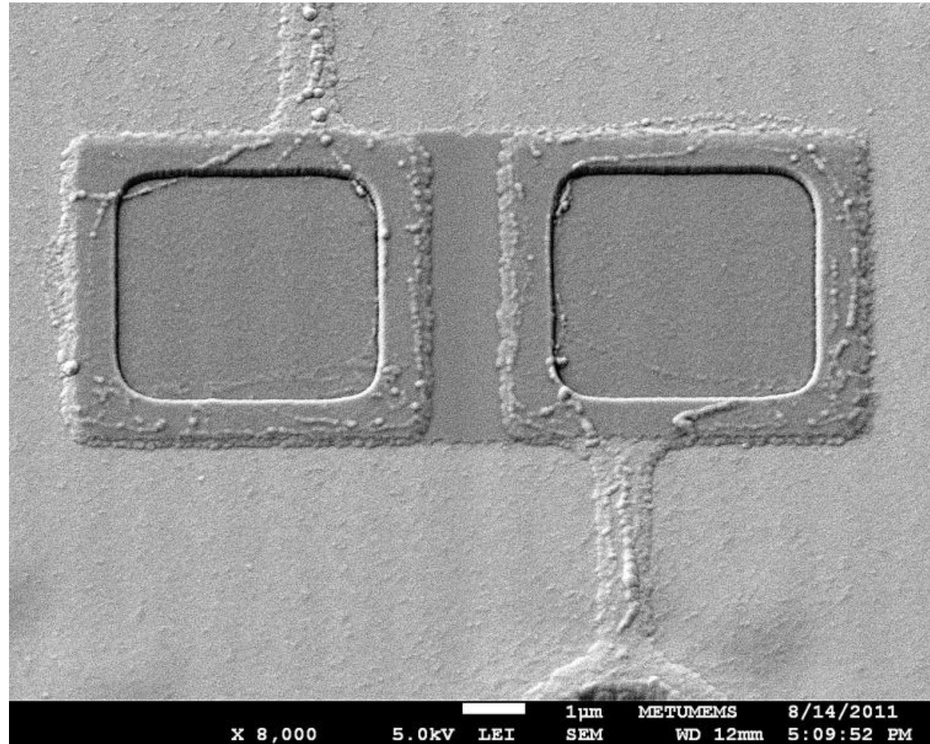

Figure 3.29: SEM image of a top electrode on the YBCO layer.

3.2.12 Deposition and Patterning of Cover YBCO

As explained in Chapter 2, the active YBCO layer is covered with another YBCO layer to prevent the resistivity change in the YBCO during the release of the pixels in O_2 plasma. Since the thickness of the total active material gets higher after cover YBCO deposition, the probability of the undercut during the etching process of YBCO becomes higher as well. Therefore, wet etching of the YBCO must be handled carefully to prevent the undercut of this layer more than the safety margins drawn in the design layouts. Figure 3.30 indicates an SEM image of a pixel after YBCO etch. The masking layer used in the photolithography step is the same as the pixel body of the second level in order to prevent the undercut problems.

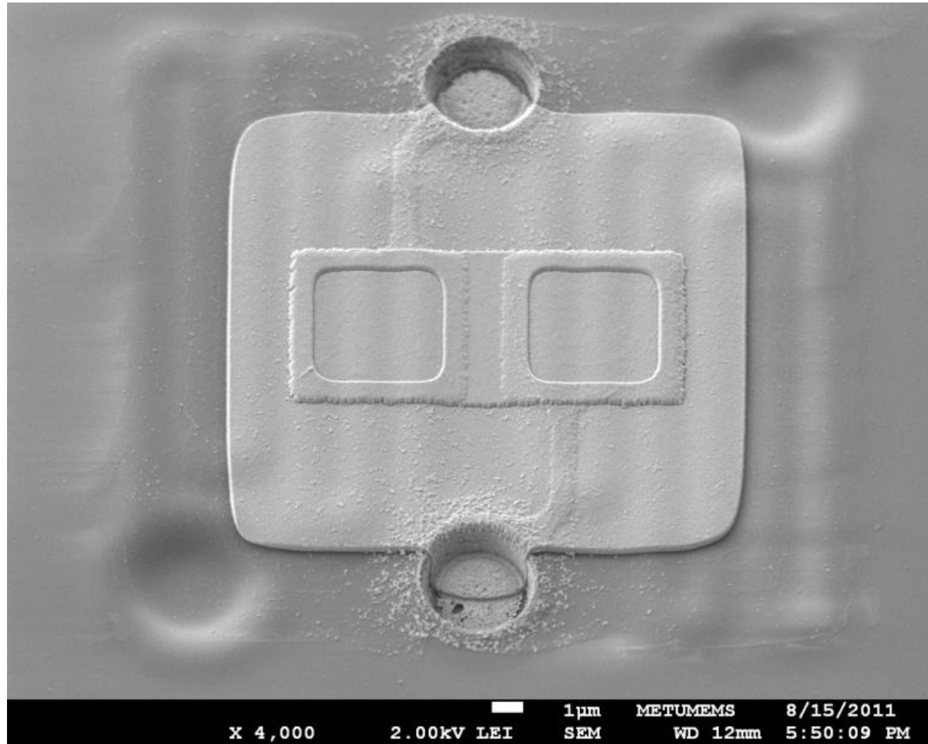

Figure 3.30: SEM image of a pixel after YBCO etch.

3.2.13 Absorber Layer

The absorption is maximized by adjusting the sheet resistance of the absorber layer between 300-500 Ω/□ as explained in Chapter 2. The absorber layer used at METU MEMS Center is NiCr. After the optimization of the sheet resistance, the absorber layer is deposited and patterned on the process wafer. Figure 3.31 shows an SEM image of a pixel after the patterning of the absorber layer. Since the absorber layer is deposited very thin, a few nm, it looks like a shadow.

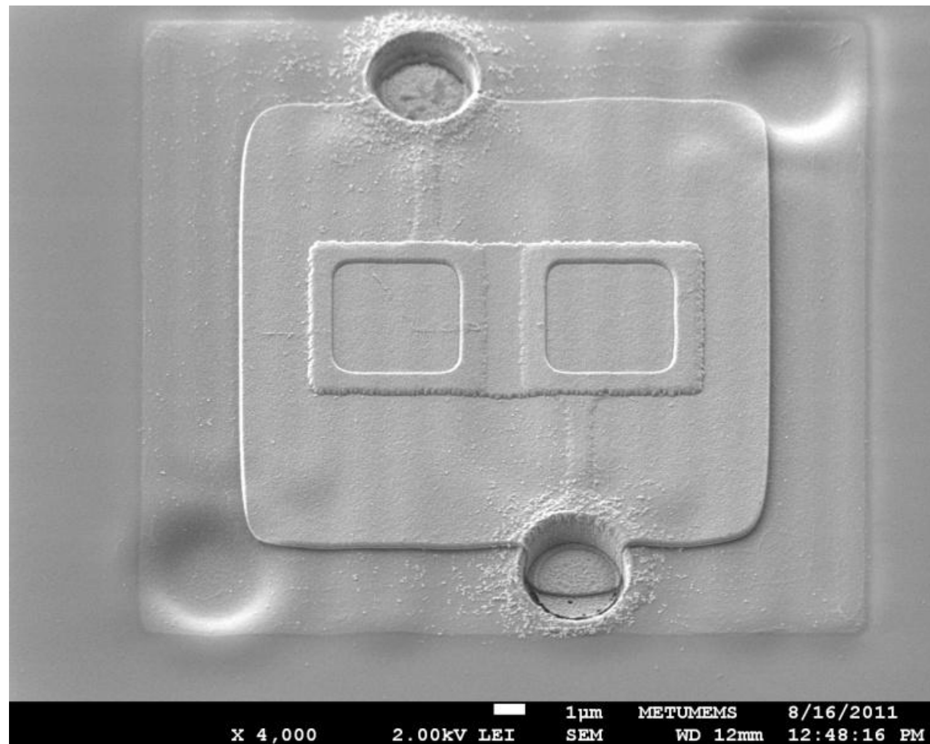

Figure 3.31: SEM image of a pixel after the patterning of the absorber layer.

3.2.14 Pixel Body Formation and Release of the Pixels

Last step of the process flow before releasing the pixels is the formation of the second structural layer. S1805 is used in the lithography step since it is observed that the etching profiles are better with S1805 than S1813 as explained before.

Once the pixel formation of the second structural layer is completed, the pixels can be released in O_2 plasma. In order to prevent the stiction problems due to the charging of the pixels in the plasma, the time required for the completion of the pixel release must be investigated, and holding the dice in O_2 plasma more than the desired amount of time must be avoided.

The major problem in the release step of the pixels is the buckling of the pixel body or the support arms. In the first suspension trials, buckling problem is encountered for the pixel body. Figure 3.32 shows an SEM image of a buckled pixel.

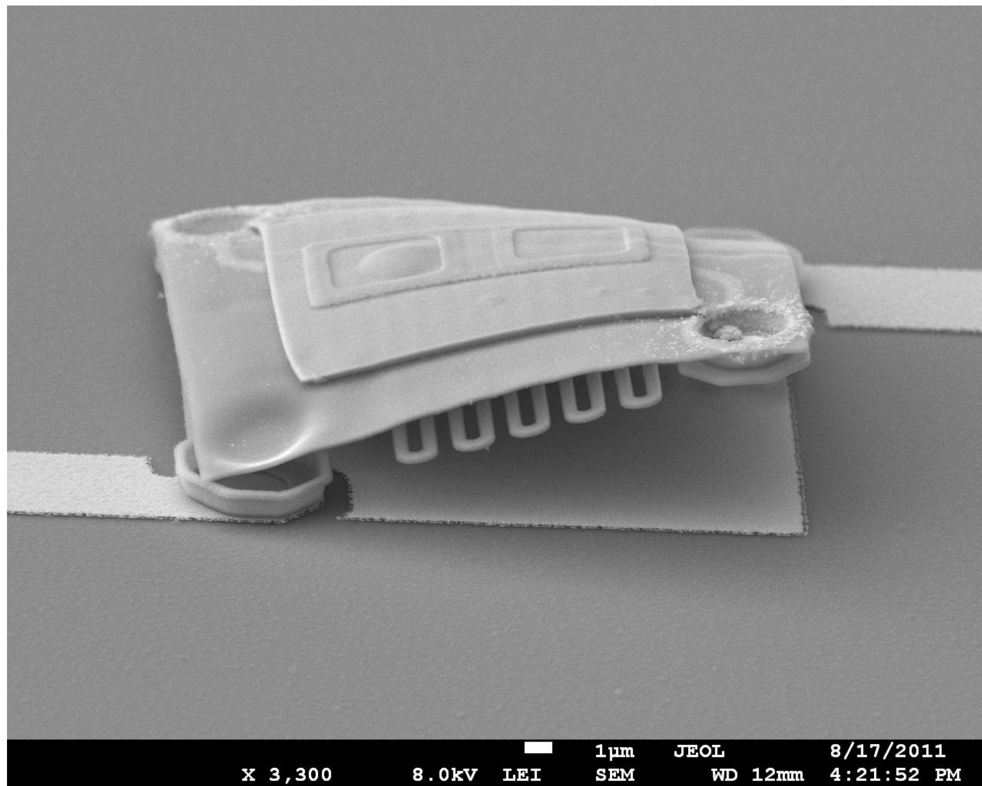

Figure 3.32: SEM image of a pixel buckled after the suspension.

This buckling problem is tried to be solved by the change of the release procedure of the pixels. The pixels are first exposed to O_2 plasma in RIE chamber for a relatively short time period. Due to the nature of the directional etching of polyimide in this plasma, the polyimide in the field is etched away. The remaining polyimide layer under the pixel body is etched in Nanoplas chamber using regular oxygen plasma. However, this method used for the suspension causes the formation of sidewalls between the pixel body and the support arms. These walls might be some kind of polymer left inside the RIE chamber. These sidewalls prevent the buckling of the pixel; however, they increase the thermal conductance of the pixels. Figure 3.33 shows an SEM image of a pixel with the sidewalls remaining between the support arms and the pixel body.

The effect of the YBCO layer on this buckling problem is also observed. The YBCO layer of the pixels on a die is completely etched away, and then the suspension of the pixels is conducted. It is observed that the pixels on this die do not buckle. Therefore, it is concluded that the cause of the buckling problem is the internal stress of YBCO layer. Figure 3.34 shows an SEM image of a pixel suspended after stripping the YBCO layer.

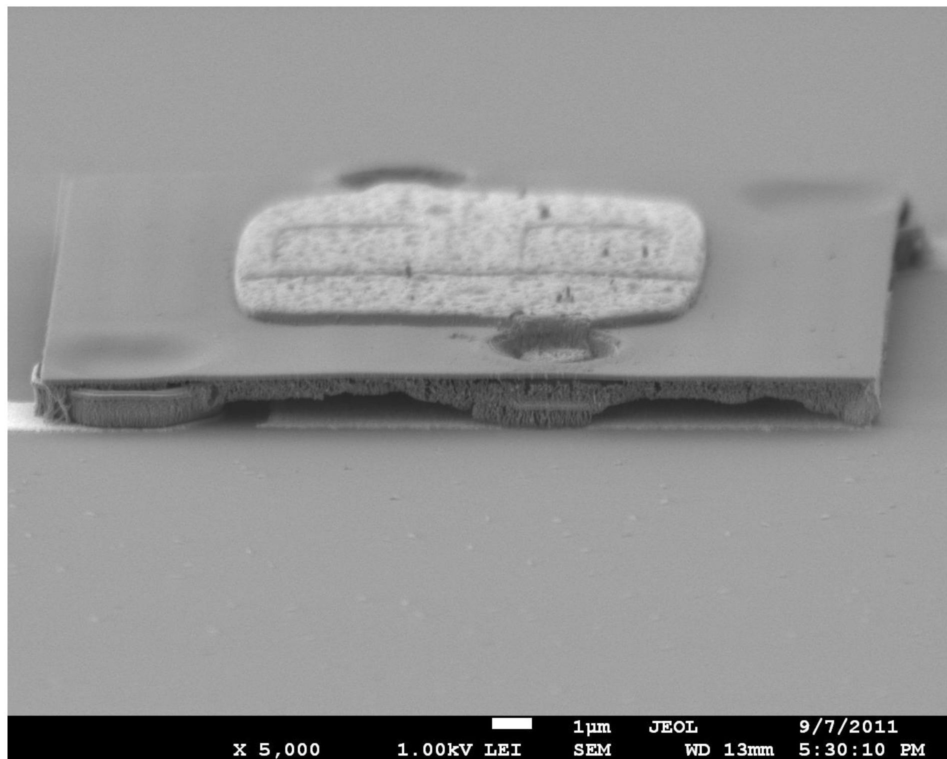

Figure 3.33: SEM image of a pixel with the sidewalls remaining between the support arms and the pixel body.

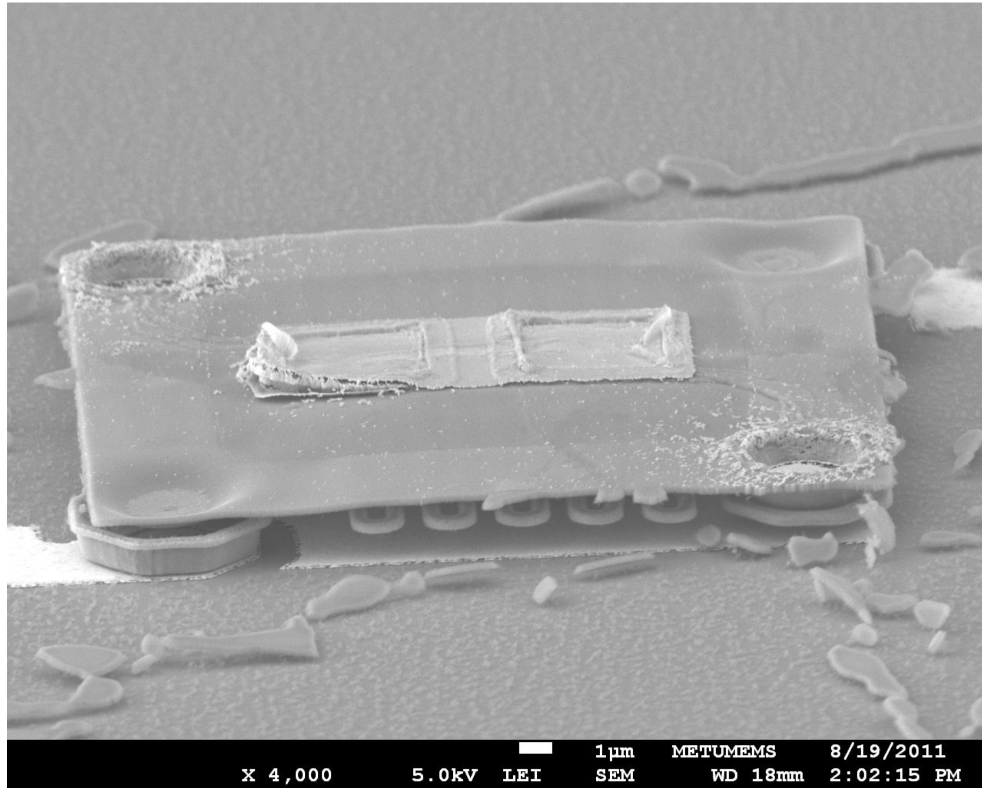

Figure 3.34: SEM image of a pixel suspended after the strip of YBCO layer.

The importance of the YBCO etch step becomes clearer after the observation of the buckling problem. Hence, the etching of the YBCO is observed more carefully to obtain this layer in smaller dimensions while protecting the YBCO layer on the active resistor area. Figure 3.35 shows an SEM image of a successfully suspended pixel while Figure 3.36 (a-c) indicates the successfully released pixels in the array forms. Moreover, Figure 3.37 shows an SEM image of a pixel with 17 µm pixel pitch. This figure states that METU MEMS facility is capable of fabricating smaller pixel sizes such as 17 µm. However, optimization for some of the process steps is needed.

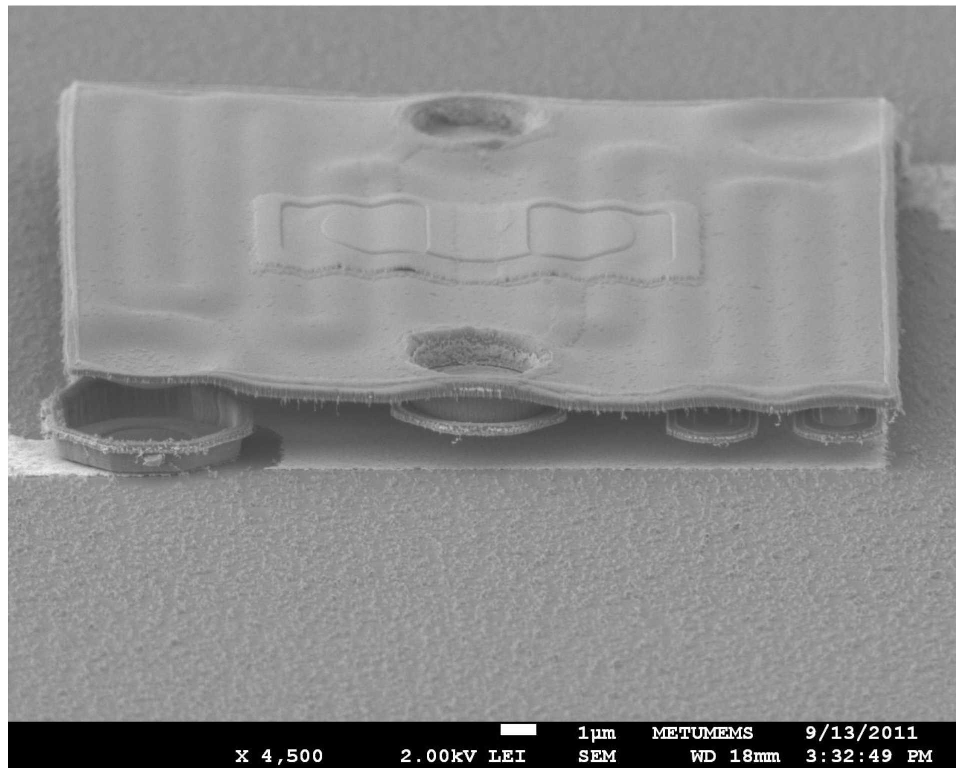

Figure 3.35: SEM image of a successfully suspended pixel.

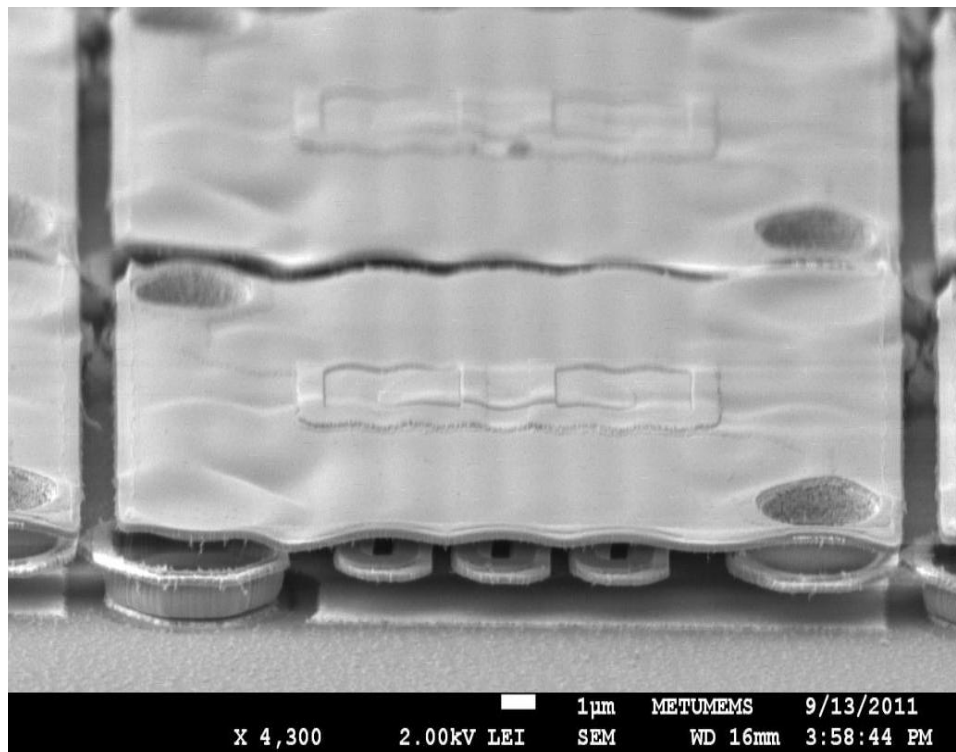

(a)

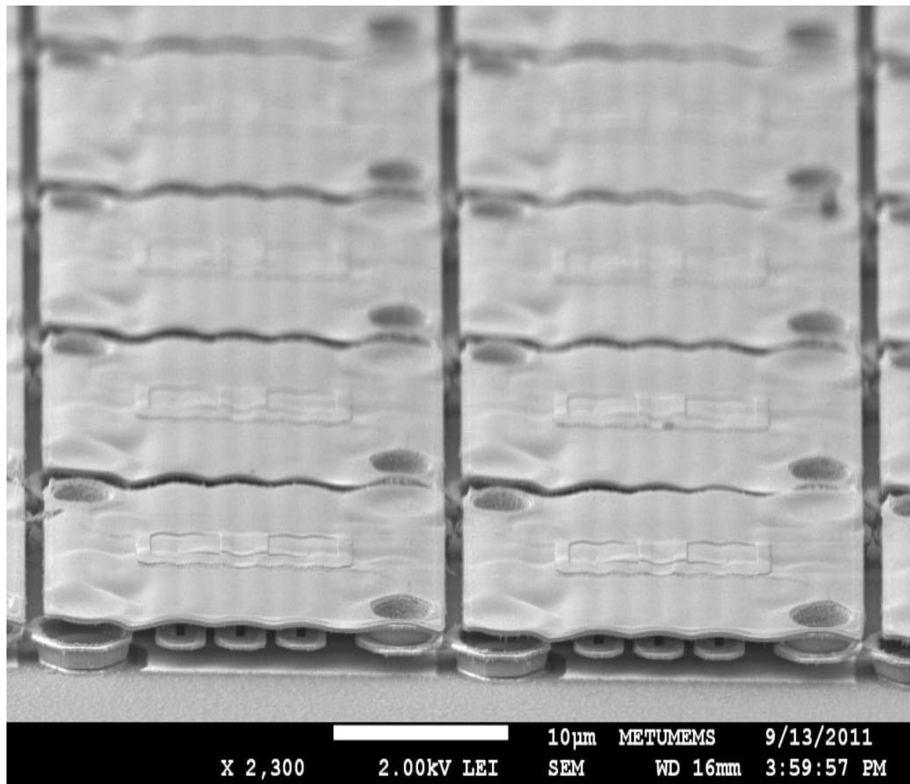

(b)

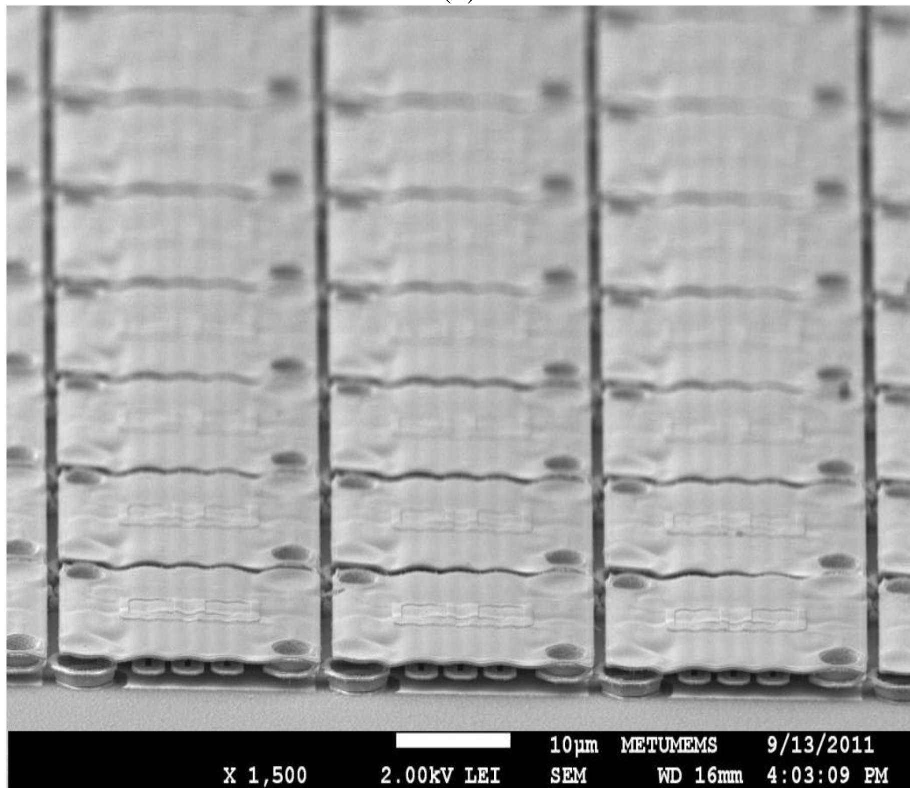

(c)

Figure 3.36: SEM images of successfully suspended pixels in array forms.

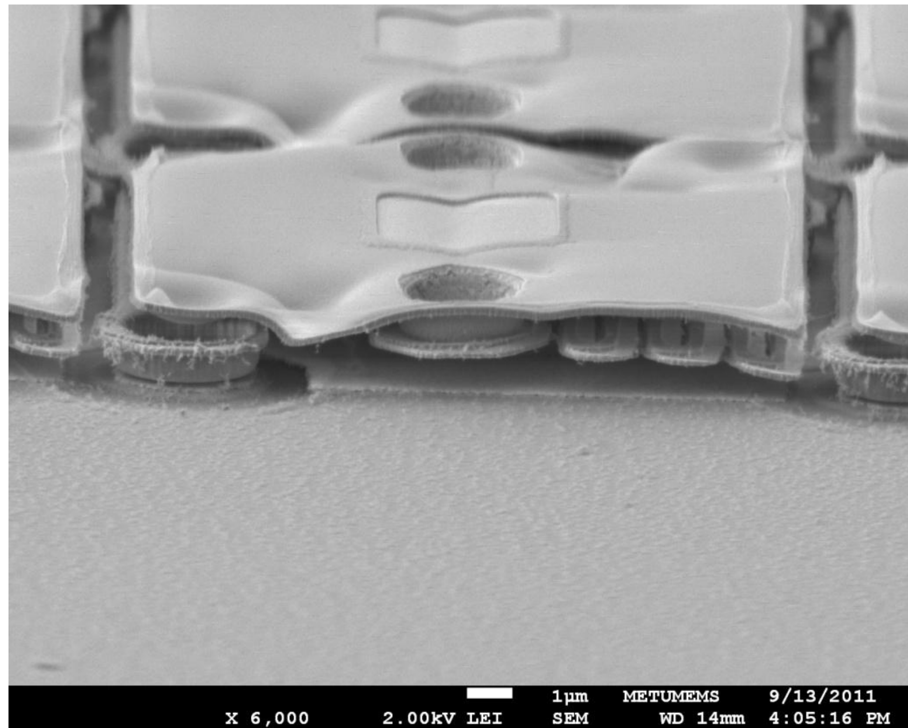

Figure 3.37: SEM image of a pixel with 17 µm pitch.

3.3 Conclusion

This chapter summarizes the design of the process flow for the proposed pixel structures and the optimization of the process steps individually. All of the process steps are CMOS compatible so that the pixels can be fabricated on FPAs. The designed pixels are successfully fabricated and suspended. The following chapter gives the test results for the characterization of these pixels.

CHAPTER 4

TEST RESULTS

This chapter gives the results of the tests performed using a specific fabricated pixel in the scope of this thesis. The pixel is chosen according to the thermal conductance and thermal time constant value. Section 4.1 gives the results of the TCR measurements. Section 4.2 explains the noise measurement method and gives the results. Section 4.3 expresses the thermal conductance measurement results, while Section 4.4 gives the responsivity results and the parameters calculated from these results. Finally, Section 4.5 summarizes the characterization of the fabricated pixel and compares the expected performance of the pixel and arrays to be fabricated using this pixel with the previous study at METU MEMS Center and the literature.

4.1 TCR Measurements

TCR is one of the most important parameters that affect the performance of the detector pixels. For the case of long and thin support arms, effective TCR gains additional importance since the resistance value of the support arms becomes comparable with the detector resistance value as explained in Section 1.3.1.

The TCR measurements are conducted in Tenney environmental chamber which is used for controlling the temperature and humidity. The pixels that have the sacrificial layer underneath are used in the TCR measurements. It takes a long time to complete the measurement; therefore, the self-heating would affect the

measurement results if the pixels were suspended. A temperature sensor, AD590 from Analog Devices, is placed right next to the test die in order to obtain the temperature value of the pixel as precisely as possible. The temperature of the chamber changes from 14°C to 34°C with a rate of 0.5 °C/min. The pixel is biased with a current of 10 μA, and the voltage on the detector is measured at the output. The temperature data obtained from the output of the AD590 and the total resistance values changing by the temperature are plotted in a graph and fitted to a polynomial. The TCR value of the detector is calculated using this polynomial. The result gives the effective TCR value of the pixel since both the detector and the support arm resistances are included in the measurements. Figure 4.1 shows the resistance change with respect to the temperature while Figure 4.2 indicates the effective TCR value of the pixel with respect to the temperature. Effective TCR is -2.8 % K^{-1} at room temperature, 25°C. The resistance value of the support arms is measured as 8 kΩ from a test pixel which is included in the same mask as the pixel. Since the TCR value of titanium is much lower than the TCR value of YBCO, the change in the resistance with respect to the temperature can be assumed as a result of the TCR of the active material, YBCO. Therefore, the TCR of the active material can be calculated using Equation (1.8)

Estimated detector resistance is calculated by subtracting the support arm resistance that is measured using the test pixels. Effective TCR value at the room temperature is calculated as -3.3 % K^{-1} using this detector resistance. This value is in good agreement with the previous TCR measurements at METU MEMS Center [49].

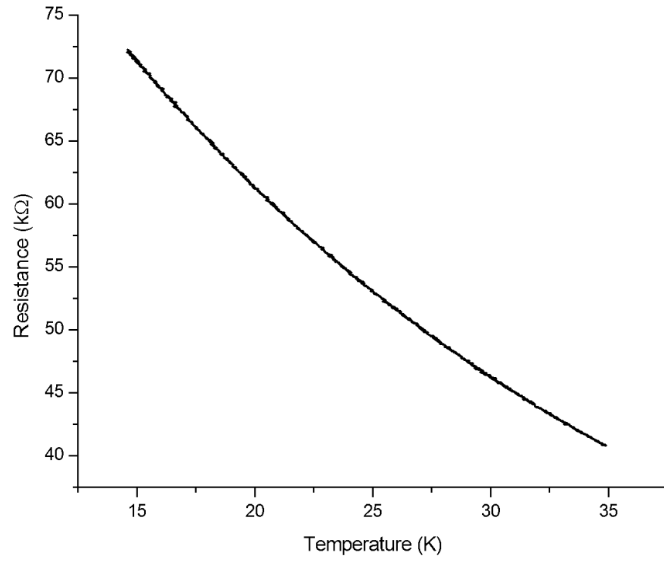

Figure 4.1: Measurement result of the resistance change with respect to the temperature

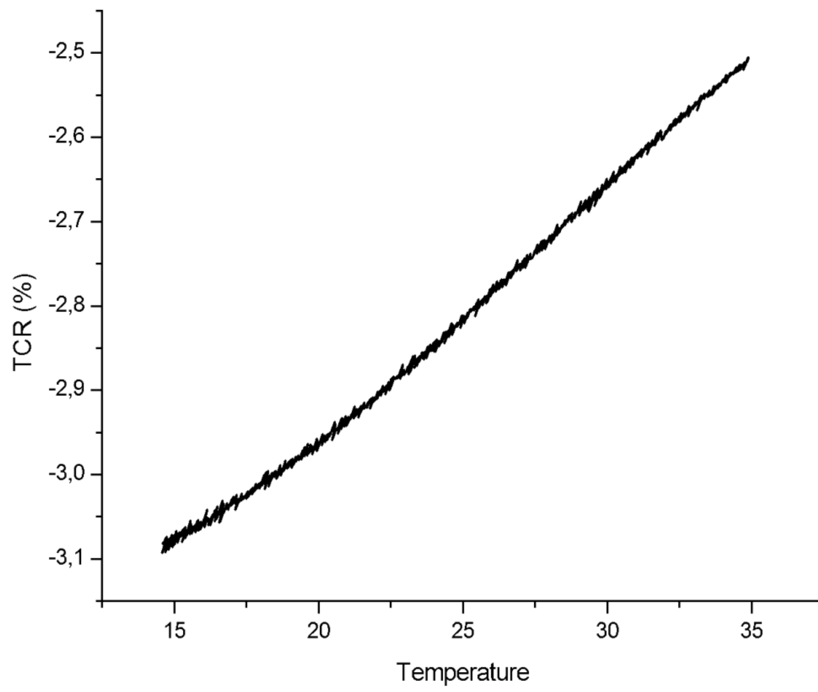

Figure 4.2: Measurement results of the effective TCR value of the pixel with respect to the temperature.

4.2 Noise Measurements

The NETD of the microbolometer pixels is directly proportional to the noise level of the pixel and electronics. Therefore, the noise of the detector pixel is a key parameter for the minimum resolvable temperature difference.

There are two dominant noise sources in microbolometer pixels: thermal noise and 1/f noise. The other noise sources are neglected as a result of low contribution compared to these two. The thermal (Johnson, Nyquist) noise originates from the random motion of the carriers in a conductive material. The power spectral density of thermal noise is calculated as:

$$S_I(f) = \frac{4kT}{R} \tag{4.1}$$

where k is Boltzmann's constant, T is the absolute temperature in K, R is the resistance of the material, and $S_I(f)$ is the power spectral density in A^2/Hz. Thermal noise is white noise since there is no frequency dependence on Equation 4.1.

There is no exact equation for the power spectral density of 1/f noise. However, a typical power spectral density expression for 1/f noise can be defined as [13]:

$$S(f) = \frac{KI^{\alpha}}{f^{\beta}} \tag{4.2}$$

where K is a constant depending on the process parameters of the resistor material, I is the current flowing through the material, α is a constant such that $1.25 < \alpha < 4$, and β is a constant which $0.8 < \beta < 3$. α is usually taken as 2 while β is 1 [13]. However, these constants are material specific and they mainly depend on the process conditions. 1/f noise is dominant at the lower frequencies. The comparison between the dominances of thermal and 1/f noise sources can be made by using the corner frequency. Corner frequency is defined as the frequency where the thermal

and 1/f noise levels are equal. Therefore, the total noise spectral density of the detector is twice the thermal noise spectral density at the corner frequency.

Earlier studies on the dependence of the 1/f noise on the active resistor area have verified that the 1/f noise decreases when the active resistor area increases. It has been also proposed in [50] that the 1/f noise can be decreased by increasing the volume of the resistor. Figure 4.3 shows the measurement results of the noise spectral densities of the resistors fabricated at METU MEMS Center with different resistor opening areas. The resistors have been fabricated on the same wafer; therefore, the process conditions are identical. The resistance value is inversely proportional to the resistor area; thus, the thermal current noise spectral density (A^2/Hz) is directly proportional to the resistor area. However, the total current noise spectral density of the resistor with smaller resistor opening area is the highest since the 1/f noise is dominant at lower frequencies as seen in Figure 4.3. Therefore, the resistor with the highest resistor area has the lowest total rms noise.

Table 4.1 summarizes the noise measurement results of the resistors having different resistor opening areas.

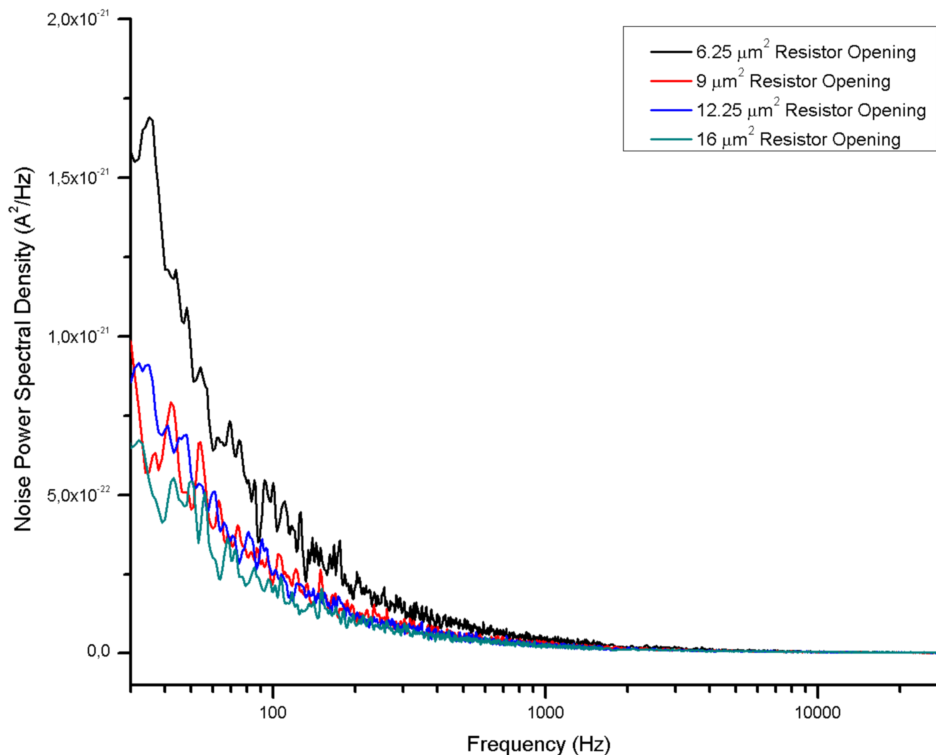

Figure 4.3: Measurement results of the noise spectral densities of the resistors fabricated at METU MEMS Center with different resistor opening areas.

Table 4.1: Summary of the noise measurement results of the resistors having different resistor opening areas.

Opening Area of the Resistor Structure (μm^2)	6.25	9	12.25	16
Resistance Value (kΩ)	62.2	40.9	29.7	21.8
Thermal Noise Spectral Density (A^2/Hz)	5.33e-25	8.1e-25	1.1e-24	1.52e-24
RMS Noise at 8.4 kHz Bandwidth (pA)	565	457	444	407

In the view of this information on 1/f noise characteristics, the resistor opening area of the pixels is designed as 16 μm^2 for both sandwich and enhanced sandwich type resistors. Since the resistance values of the sandwich type resistors are lower than the desired value, only the noise measurements of the enhanced sandwich type resistor are conducted. Figure 4.4 shows the schematic view of the noise measurement setup.

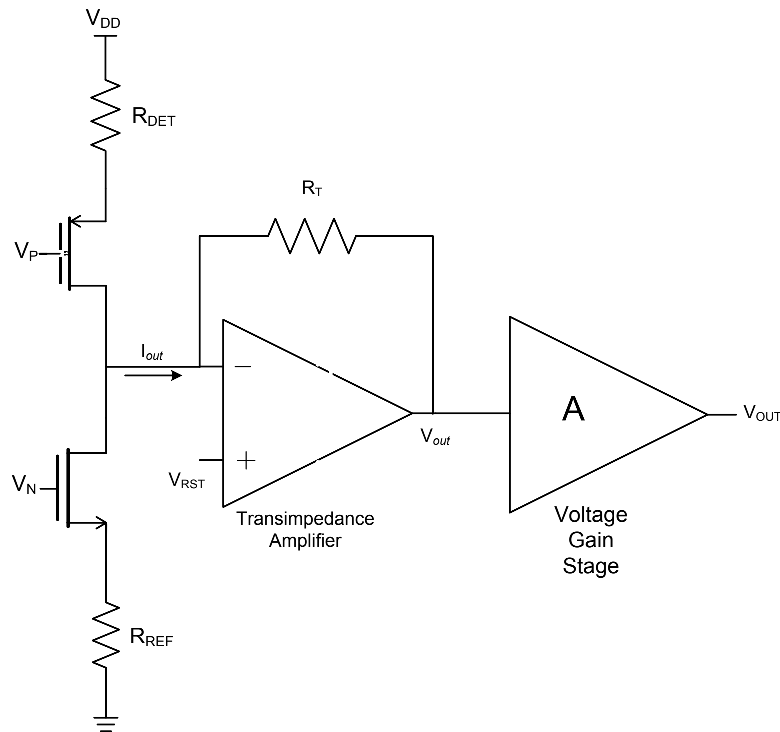

Figure 4.4: Schematic view of the noise measurement setup.

Reference detectors are used in the readout circuit designed at METU MEMS Research Center in order to cancel the self-heating effect on the detector pixels. Therefore, the noise of the reference detector must be included in theoretical NETD calculations. Thus, the noise of a pair of resistors is measured. The resistance values of the reference detectors can be assumed to be equal to the resistance values of the active detector pixel; therefore, a pair of resistors having equal resistance values is used in noise measurements.

The resistors are connected to two injection transistors as indicated in Figure 4.4. These transistors are used to adjust the value of the current flowing through the reference and detector resistors. Relatively small differences between the resistance values of the detector and the reference can be compensated by changing V_N or V_P. It is vital to adjust the voltages on R_{DET} and R_{REF} such that the current sourced by the upper circuit is sunk by the lower portion. No DC current must flow through the transimpedance amplifier. The noise current of the resistor pair flows through R_T

which converts this current, I_{out}, to voltage V_{out}. Then, the voltage is amplified by a voltage gain stage. The setup noise is measured by disconnecting the V^- input of the transimpedance amplifier from the transistor pair. This measured noise is subtracted from the detector noise. A pair of single pixels with the enhanced sandwich type resistor having 55 kΩ resistance value is used in the noise measurements. The resistors are biased with three different current values, 10 µA, 20 µA, and 30 µA. The corner frequencies are calculated using the following equation:

$$S(f) = P_1 + \frac{P_2}{f^{P3}} \tag{4.3}$$

where P_1 is the thermal noise contribution, P_2 is equal to KI^{α} constant in equation 4.2, f is the frequency, and P_3 is a process dependent parameter, β in Equation 4.2. The input referred noise data is fitted into Equation 4.3 using Origin software. P_1 is calculated using Equation 1 and set as constant in the software. P_2 and P_3 are process dependent parameters; therefore, they are set as variable and calculated by the software after a number of iterations. The corner frequency is calculated using the fact that the thermal and 1/f noise are equal at this frequency. Figure 4.5 shows the noise power spectral densities of single pixels with 55 kΩ resistors under 10 µA, 20 µA, and 30 µA bias current values and the corresponding corner frequencies which are 1.4 kHz, 9.5 kHz, and 23.5 kHz respectively.

Table 4.2 summarizes the noise measurement results of the single pixels with the enhanced sandwich type resistor structure having a resistance value of 55 kΩ..

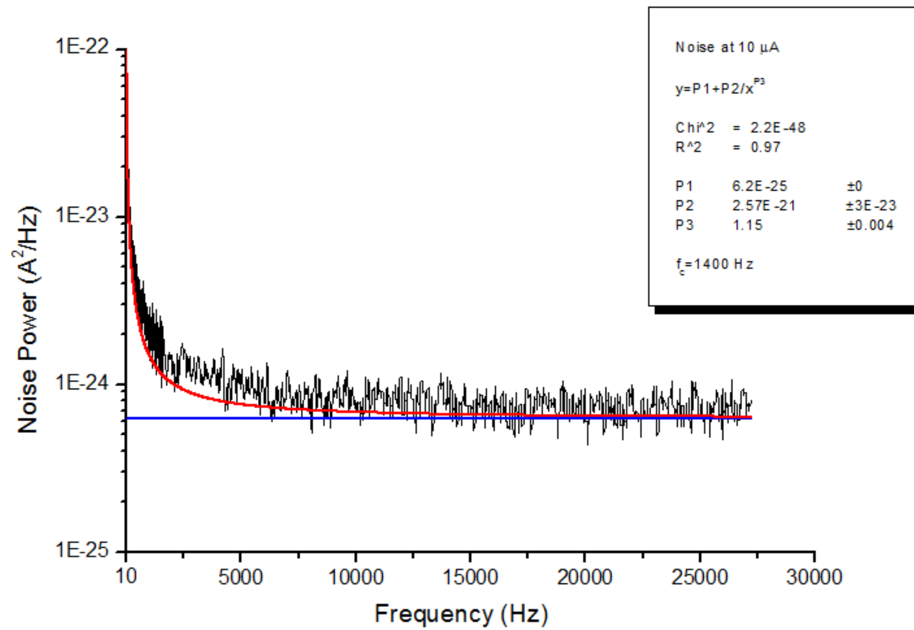

(a)Measurement results of the noise power spectral density of a pixel in the scope of this thesis. The resistance value is 55 kΩ, current bias is at 10 µA, and the corner frequency is calculated as 1.4 kHz.

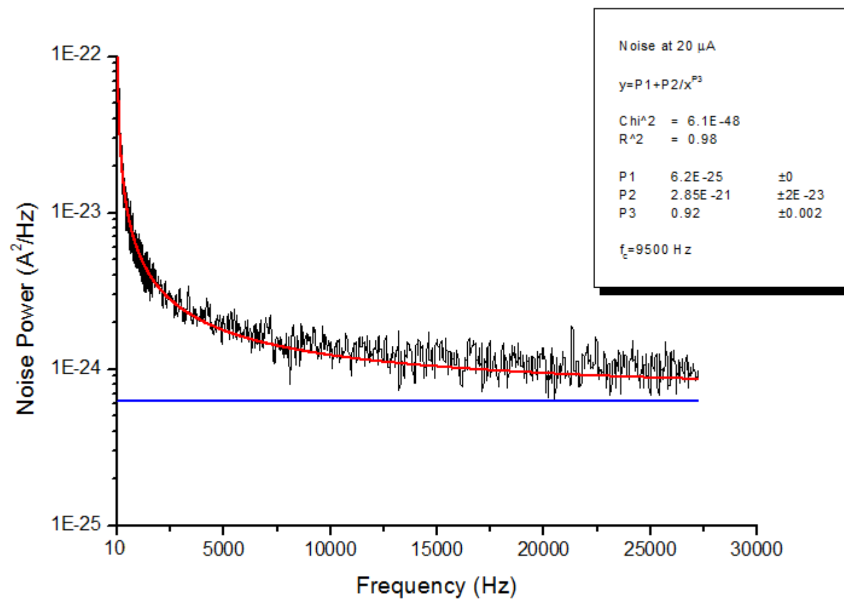

(b) Measurement results of the noise power spectral density of a pixel in the scope of this thesis. The resistance value is 55 kΩ, current bias is at 20 µA, and the corner frequency is calculated as 9.5 kHz.

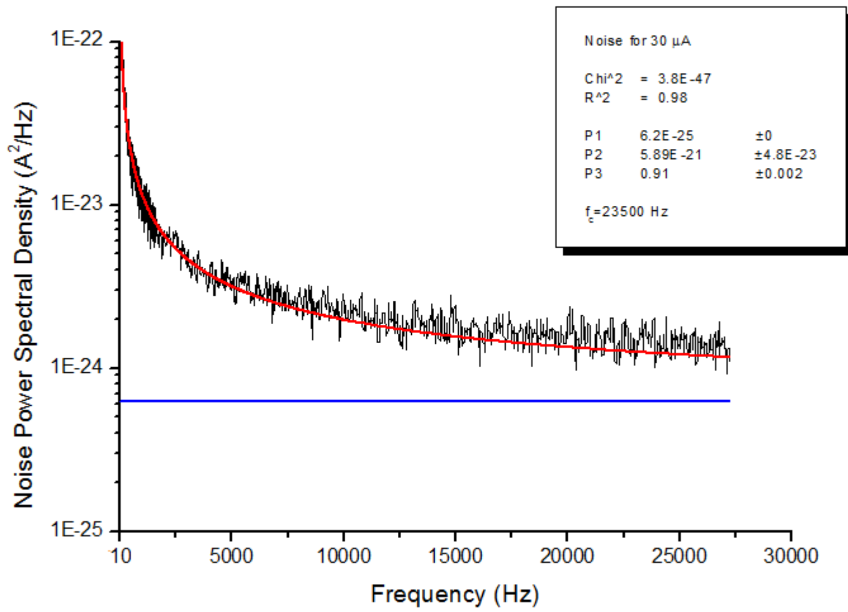

(c) Measurement results of the noise power spectral density of a pixel in the scope of this thesis. The resistance value is 55 kΩ, current bias is at 30 µA, and the corner frequency is calculated as 23.5 kHz.

Figure 4.5: Noise power spectral densities of 55 kΩ resistors under 10 µA, 20 µA, and 30 µA bias currents and the corresponding corner frequencies.

Table 4.2: Summary of the noise measurement results of single pixels with enhanced sandwich type resistors.

Bias Current (µA)	10	20	30
Resistance Value (kΩ)	55	55	55
Corner Frequency (kHz)	1.4	9.5	23.5
RMS Noise in 8.4 kHz Bandwidth (pA)	125	192	270
RMS noise in 16.8 kHz Bandwidth (pA)	149	218	299

4.3 Thermal Conductance Measurements

Thermal conductance is the most important performance parameter of the microbolometer pixels defining the thermal isolation of the pixel. Thermal conductance measurements must be carried out in vacuum to prevent the heat losses due to the molecules in air. The measurements are conducted in an automatic probe station at METU MEMS facility. The test pixels are sourced by a current source and the voltages on the pixels are measured. Measurements are repeated for different current values and the thermal conductance is extracted from [32]:

$$G_{th} = \frac{I^2 R \alpha}{\ln\left(\frac{R}{R_0}\right)} \tag{4.4}$$

where I is the bias current, R is the resistance under vacuum, α is the effective TCR of the detector, and R_0 is the initial resistance of the detector. Initial resistance of the detector is calculated from the measurements taken under very close current biases assuming that the thermal conductance values are equal.

High current biases may result in an excessive heating of the pixel, and TCR value used in the calculations may not be valid since TCR depends on the temperature. On the other hand, decreasing the bias current also decreases the sensitivity of the measurement. Therefore, the values of the current biases must be selected carefully.

The measurements are performed for a specific pixel. The specifications of the pixel in terms of the support arm parameters are given in Table 4.3. The thermal conductance value of the pixel is measured as 17.4 nW/K. This value is compatible with the simulation result obtained using CoventorWare software. The simulation result is found as 16.8 nW/K. This small difference can be explained by the nonideality of the process steps, such as undesired undercut in a process or deposition of a layer thicker than the design value.

Table 4.3. The spesifications of the pixel used in the thermal conductance measurements.

	pixel_1
Width of the metal layer in the support arms	0.8 μm
Width of the nitride layers in the support arms	0.8 μm
Spacing between the arms	0.8 μm

4.4 Responsivity Measurements

The responsivity of the pixel is another important parameter needed to be measured for the characterization of the pixel. It expresses the output voltage change of the pixel for incident infrared radiation. The responsivity measurements are carried out using the automatic probe station at METU MEMS facility. Figure 4.6 shows the measurement setup used in the responsivity measurements. The pixel is placed in the chamber, which is under vacuum. Then, the pixel is exposed to infrared radiation sourced by the blackbody shown in Figure 4.6, and this radiation is chopped in the range of 10 Hz to 100 Hz. The incident radiation is filtered by a silicon wafer that is coated with an anti-reflective material. Figure 4.7 shows the transmission of this silicon wafer measured using the FTIR mode of the ellipsometer at METU MEMS Center. The detector pixel is sourced with a constant current, and the output is measured as a voltage using a dynamic signal analyzer for the frequency that the incident radiation is chopped at. AC responsivity of the pixel is calculated by dividing this output to the incident radiation sourced by the blackbody of the system.

Figure 4.6: Measurement setup used in the responsivity measurements.

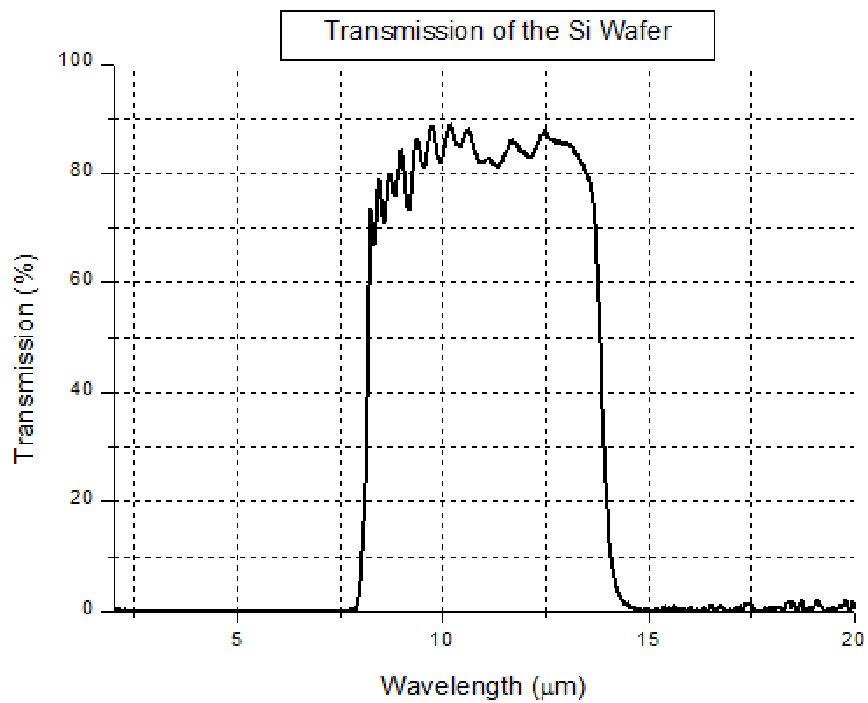

Figure 4.7: Measured transmission of the Si wafer used in the responsivity measurements.

The AC resposivity, $\Re_{AC}$, of the detector pixel can be expressed as:

$$\Re_{AC} = \frac{\Re_{DC}}{\sqrt{(1+(\omega\tau)^2}} \tag{4.5}$$

where $\Re_{DC}$ is the DC responsivity of the pixel, ω is the modulation frequency of the incident radiation, and τ is the thermal time constant of the pixel. By combining Equations 1.19 and 4.5 DC responsivity, $\Re_{DC}$, of the detector pixel can be found as:

$$\Re_{DC} = \frac{\eta I_d \alpha R_d}{G_{th}} \tag{4.6}$$

where η is the absorptance of the detector pixel, I_d is the bias current, α is the TCR of the detector pixel, which is measured as -2.8 %/K, R_d is the detector resistance (55 kΩ), and G_{th} is the thermal conductance of the pixel, which is measured as 17.4 nW/K.

Measured AC responsivity is drawn and fitted using Equation 4.5. Then, DC responsivity and the thermal time constant are calculated using the data fitted. After calculating the DC responsivity of the pixel, absorptance can be estimated using Equation 4.6. Figure 4.8 shows the measured responsivity values together with the fitted responsivity curve. DC responsivity of the pixel is calculated as 84.5 kV/W while the thermal time constant is found as 17.5 ms. The time constant calculated in the simulations is 19.3 ms which is close to the measured one. The difference between these two may be due to the undercut amount of the active material, YBCO. The layout of active material layer for the proposed pixels is drawn considering the undercut problems, and the simulations are conducted using this layout. However, the YBCO layer on the fabricated pixel is thinner because of the undercut as predicted. The simulation is repeated using the YBCO dimensions obtained in the fabrication. The thermal time constant of the pixel is found as 16.8 ms. There is still difference between the simulation and measurement results. However, this difference may be expected due to the process variations.

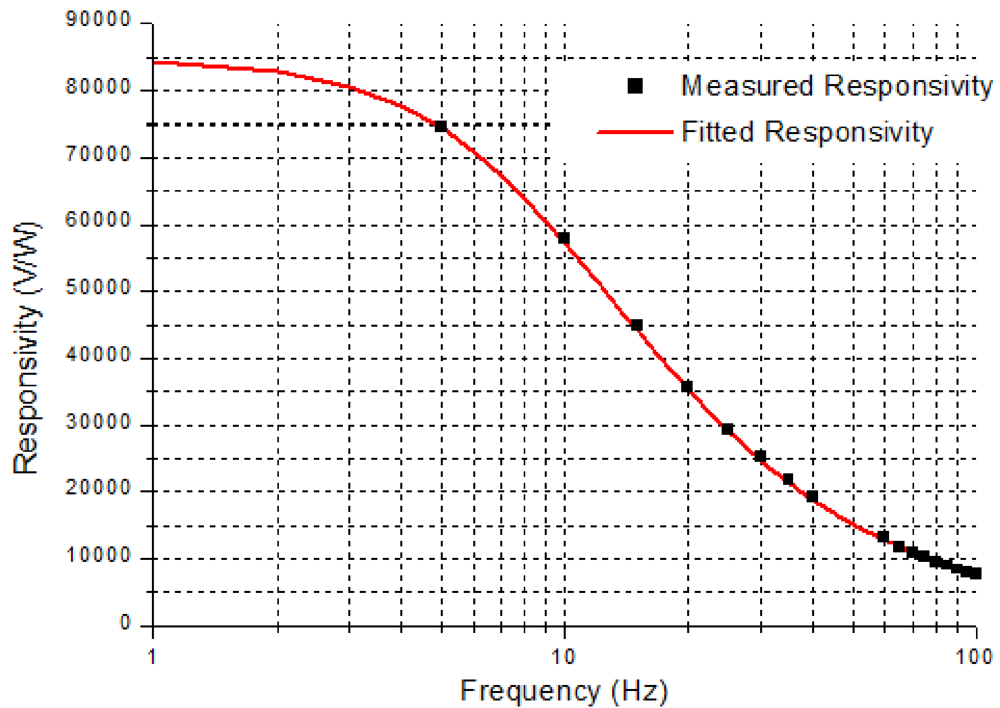

Figure 4.8: Measured responsivity values together with the fitted responsivity curve

The thermal time constant of the pixel is measured by heating the pixel using pulsed current bias. The output voltage change of the pixel is measured, and the thermal time constant is calculated using this measurement. The same value, 17.5 msec, is obtained using this method. Therefore, the thermal time constant value of the pixel is verified. Table 4.4 summarizes the comparison of the thermal simulation and measurement results.

Table 4.4: The comparison of the simulation and measurement results for the thermal conductance and the thermal time constant of the pixel.

	Thermal Conductance	Thermal Time Constant
Simulation	16.8 nW/K	16.8 ms
Measurement	17.4 nW/K	17.5 ms

4.5 Conclusion

This chapter gives the results of the test conducted for the characterization of the designed pixels. The effective TCR of the detector pixel is -2.8 % K^{-1}, which correspond to a TCR value of -3.3 % K^{-1} for the active material itself. 1/f noise of the resistor structure under 20 μA bias current has a corner frequency of 9.5 kHz, which can be considered as relatively high. The total rms noise of the detector is 192 pA for 8.4 kHz bandwidth for a bias current of 20 μA. The thermal conductance value of the pixel is 17.4 nW/K, with a time constant of 17.5 ms. These values are in a good agreement with the simulation results. This shows that the design parameters are met after the fabrication. Table 4.5 summarizes the performance parameters of the fabricated pixel and expected NETD values of the pixels for two different array sizes. The results show that the performance parameters of the fabricated pixel are comparable with the reported values in the literature [21]. Besides, the expected NETD value of this pixel can reach the reported value.

Table 4.5: Summary of the performance parameters of fabricated pixel and expected NETD values

	This Study	Previous Study at METU MEMS [31]	Raytheon [21]
Pixel Dimension	25 μm	25 μm	25 μm
Fill Factor	92%	92%	>70 %
Resistance	55 kΩ	72 kΩ	20-200 kΩ
TCR	-2.8 %/K	-3.4 %/K	>2.2 %/K
Detector Bias	1.5 V	1.5 V	-
Integration Time	60 μs	-	-
Absorption Efficiency	54 %	16 %	>80 %
Corner Frequency of 1/f Noise	9.4 kHz	-	-
Thermal Conductance	17.4 nW/K	50 nW/K	35 to 75 nW/K
Time Constant	17.5 ms	19 ms	<12 ms
NETD (640x480 FPA)	36 mK*	311 mK	<50 mK
NETD (388x284 FPA)	33 mK*	-	-

*Estimated NETD values calculated using the performance parameters measured in the characterization step of the pixel.

CHAPTER 5

CONCLUSION AND FUTURE WORK

This thesis reports the design and fabrication of multilevel microbolometer detector pixels using MEMS surface micromachining techniques. The pixels are designed in two levels. The first level is allocated for the support arms to decrease the thermal conductance value of the pixel; therefore, to increase the NETD value for high performance. The second level is composed of the pixel body containing the resistor structure and the absorber layer. The resistor structure is designed such that it occupies a relatively small area considering the absorption characteristics and it has a resistance value around 60 kΩ to fulfill the readout requirements. The fabrication and tests of the pixels are carried out in the scope of this study.

The achievements obtained during this study can be listed as follows:

1. A suitable active material, YBCO, is selected considering the TCR and noise characteristics together with the process compatibility with the other steps. The resistor structure is determined as the enhanced sandwich type resistor since it provides the desired resistance value, and it has low noise characteristics.

2. The pixel structure is designed such that it is applicable to high-resolution FPAs. Two-level microbolometer pixel structure is chosen with 25 μm pixel pitch. The allocation of the first level to the support arms gives the liberty to design them with a wide range of thermal conductance values. The second

level is optimized to have high absorption characteristics while maintaining the mechanical stability.

3. The absorption characteristics of the pixels are examined. Optimum sacrificial and structural layer thicknesses are obtained in order to have the maximum absorption coefficient. The absorption coefficient of a pixel is calculated as 69.5 %.

4. The thermal simulations are carried out using CoventorWare software. The thermal conductance value of a pixel with the 0.8 μm-wide support arms is simulated as 16.8 nW/K, and the corresponding time constant is 19.3 msec.

5. A CMOS compatible process flow is designed to fabricate the pixels. The process flow is composed of 14 masking layers. The individual optimization of the process steps is conducted. Then, the pixels are fabricated using these steps.

6. The test and the measurements are performed on the fabricated pixels. An effective TCR value of -2.8 % K^{-1} is obtained, which corresponds to a TCR value of -3.3 % K^{-1} for the active material. The noise of the fabricated pixels is also examined. The resistor structure of the detector has 1/f noise with a 9.5 kHz cutoff frequency at 20 μA bias. The cutoff frequency decreases down to 1.4 kHz if the pixel is biased with a current of 10 μA. The thermal conductance value of pixel is measured as 17.4 nW/K, with a time constants of 17.5 ms. The absorptance of the pixel is also measured as 54.6 %. Expected NETD values with the measured performance parameters are 33 mK and 36 mK for 384x288 and 640x480 format FPAs, respectively

Although the results obtained in this study are promising for the high performance and high resolution imaging, there is still remaining work to be done for the improvement of the performance. The future work to be done can be listed as follows:

1. The RIE process for the etching of the YBCO should be optimized. This can solve the undercut problem of YBCO.

2. New deposition conditions for the YBCO layer should be tried to minimize the noise level of YBCO. While doing this the thickness of the YBCO layer must remain relatively thinner to prevent undercut problems unless the RIE system is optimized to etch YBCO.

3. The pixel body can be redesigned to decrease the thermal capacitance of the pixel. The time constant can be decreased by this way.

4. The planarization of the second sacrificial layer by using CMP should be tried. Then, the topology under the pixel body would not affect the body formation. Therefore, the stiction problems between the support arms and pixel body can be decreased.

5. Au RIE for the bottom electrodes can be optimized. Then, smaller structures can be implemented which results in an increase on the absorption coefficient and decrease on the thermal capacitance of the pixel.

6. The optimum pixel designed and fabricated should be applied to an FPA.

REFERENCES

[1] A.Rogalski, “Infrared detectors: status and trends,” *Progress in Quantum Electronics,* Vol. 27, pp. 59–210, 2003.

[2] http://www.theses.ulaval.ca/2005/23016/apb.html, Last Access: 26.06.2011.

[3] http://en.wikipedia.org/wiki/Infrared, Last Access: 26.06.2011.

[4] G. D. Boreman, *Basic Electro-Optics for Electrical Engineer*s, SPIE Press, 1998

[5] P. W. Kruse and D. D. Skatrud, *Uncooled Infrared Imaging Arrays and Systems,* Semiconductor and Semimetals, Vol. 47, Academic Press, 1997.

[6] T. J. Seebeck, “Magnetische Polarisation der Metalle und Erze durch Temperatur-Differenz,” *Abhandlung der deutschen Akademie der Wissenschaften zu Berlin,* pp. 265–373, 1822.

[7] M. C. Foote, T. R. Krueger, J. T. Schofield, D. J. Mccleese, T. A. McCann, E. W. Jones, and M. R. Dickie, “Space Science Applications of Thermopile Detector Arrays”, *Proc. of SPIE, Infrared Technology and Applications XXIX,* Vol. 4999, pp. 443-447, 2003.

[8] M. C. Foote, “Progress Towards High-Performance Thermopile Imaging Arrays”, *Proc. of SPIE, Infrared Technology and Applications XXVII,* Vol. 4369, pp.350-354, 2001.

[9] A. Graf, M. Arndt, M. Sauer, and G. Gerlach, “Review of Micromachined Thermopiles for Infrared Detection”, Measurement Science and Technology, Vol.18, pp. 59-75, May 2007.

[10] R. L. Byer and C. B. Roundy, “Pyroelectrıc Coeffıcient Direct Measurement Technique and Applicatıon to a nsec Response Time Detector,” *IEEE Trans. Sonics & Ultrasonics*, Vol. 3, pp. 333-338, 1972.

[11] P. Muralt, “Micromachined Infrared Detectors based on Pyroelectric Thin Films”, *Reports on Progress in Physics,* Vol. 64, pp. 1339-1388, September 2001.

[12] A. Hossain and M. H. Rashid, "Pyroelectric Detectors and Their Applications", IEEE Transactions on Industry Applications, Vol. 27, No. 5, pp. 824-829, October 1991.

[13] J. M. Palmer and B. G. Grant, *The Art of Radiometry*, SPIE Press, 2009.

[14] S. Eminoğlu, M. Y. Tanrıkulu, and T. Akın, "Low-Cost 64×64 Uncooled Infrared Detector Arrays in Standard CMOS," *The 12th International Conference on Solid-State Sensors and Actuators (TRANSDUCERS'03)*, Vol. 1, pp. 316-319, June 2003.

[15] S. Eminoğlu, D. Sabuncuoğlu Tezcan, M. Y. Tanrıkulu , and T. Akın, "Low-Cost Uncooled Infrared Detectors in CMOS Process," *Sensors and Actuators A*, Vol. 109/1-2, pp. 102-113, December 2003.

[16] Selim Eminoglu, Mahmud Yusuf Tanrikulu, and Tayfun Akin, "A Low-Cost 128 × 128 Uncooled Infrared Detector Array in CMOS Process," *Journal Of Microelectromechanical Systems,* Vol. 17, No.1, February 2008.

[17] T. Ishikawa, M. Ueno, Y. Nakalci, K. Endo, Y. Ohta, J. Nakanishi, Y. Kosasayama, H. Yagi, T. Sone, and M. Kimata,"Performance of 320 x 240 Uncooled IRFPA with SOl Diode Detectors," *Proc. of SPIE, Infrared Technology and Applications XXVI,* Vol. 4130, pp. 152-159, April 2000.

[18] M. Ueno, Y. Kosasamaya, T. Sugino, Y. Nakaki, Y. Fujii, H. Inoue, K. Kama, T. Seto, M. Takeda, and M. Kimata, "640 x 480 pixel uncooled infrared FPA with SOI diode detectors," *Proc. of SPIE, Infrared Technology and Applications XXXI*, Vol. 5783, pp. 566-577, March 2005.

[19] D.Takamuro, T. Maegawa, T. Sugino, Y. Kosasayama, T. Ohnakado, H. Hata, M. Ueno, H. Fukumoto and K. Ishida, H. Katayama, T. Imai, and M. Ueno, "Development of new SOI diode structure for beyond 17μm pixel pitch SOI diode uncooled IRFPAs," *Proc. of SPIE, Infrared Technology and Applications XXXVII*, Vol. 8012, pp. 80121E-1–80121E-10, March 2005.

[20] R. A. Wood, "Use of Vanadium Oxide in Microbolometer Sensors," US. Patent No. 5450053, 1995.

[21] D. Murphy, M. Ray, J. Wyles, C. Hewitt, R. Wyles, E. Gordon, K. Almada, T. Sessler, S. Baur, D. Van Lue, and S. Black, "640 x 512 17 μm Microbolometer FPA and Sensor Development," *Proc. of SPIE, Infrared Technology and Applications XXXVII,* Vol. 6542, pp. 65421Z-1–65421Z-10, April 2007.

[22] C. Li, G. D. Skidmore, and C.J. Han, "Uncooled VOx Infrared Sensor Development and Application," *Proc. of SPIE, Infrared Technology and Applications XXXVII,* Vol. 8012, pp. 80121N-1–80121N-8, April 2011.

[23] U. Mizrahi, L. Bikov, A. Giladi, N. Shiloah, S. Elkind, T. Czyzewski, I. Kogan, S. Maayani, A. Amsterdam, I. Vaserman, Y. Hirsh, and A. Fraenkel, "New Developments in SCD's 17µm VOx µ-Bolometer Product Line," *Proc. of SPIE, Infrared Technology and Applications XXXVII,* Vol. 7660, pp. 76600W-1–7660W-6, April 2010.

[24] R. Blackwell, G. Franks, D. Lacroix, S. Hyland, and R. Murphy, "Small Pixel Uncooled Imaging FPAs and Applications," *Proc. of SPIE, Infrared Technology and Applications XXXVI,* Vol. 7660, pp. 76600Y-1–76600Y-7, April 2010.

[25] S. H. Black, T. Sessler, E. Gordon, R. Kraft, T Kocian, M. Lamb, R. Williams, T. Yang, "Uncooled Detector Development at Raytheon," *Proc. of SPIE, Infrared Technology and Applications XXXVII,* vol. 8012, pp. 80121A-1–80121A-12, April 2011.

[26] C. Li, C.J. Han , and G. D. Skidmore, "Overview of DRS Uncooled Vox Infrared Detector Development," *Proc. of SPIE, Optical Engineering,* Vol. 50(6), pp. 061017-1–061017-7, June 2011.

[27] A. Fraenkel, U. Mizrahi, L. Bikov, A. Giladi, N. Shiloah, S. Elkind, I. Kogan, S. Maayani, A. Amsterdam, I. Vaserman, O. Duman, Y. Hirsh, F. Schapiro, A. Tuito, and M. Ben-Ezra, "SCD's Uncooled Detectors and Video Engines for a Wide Range of Applications," *Proc. of SPIE, Infrared Technology and Applications XXXVII,* Vol. 8012, pp. 801204-1–801204-8, April 2011.

[28] J. L. Tissot, S. Tinnes, A. Durand, C. Misassian, P. Minassian, P. Robert, M. Vilain, and J.J. Yon, "High-performance uncooled amorphous silicon video graphics array and extended graphics array infrared focal plane arrays with 17-μm pixel pitch," *Proc. of SPIE, Optical Engineering,* Vol. 50(6), pp. 061006-1–061006-8, June 2011.

[29] C. M. Hanson, S. K. Ajmera, J. Brady, T. Fagan, W. McCardel, D. Morgan, T. Schimert, A. J. Syllaios, M. F. Taylor, "Small Pixel a-Si/a-SiGe Bolometer Focal Plane Array Technology at L-3 Communications," *Proc. of SPIE, Infrared Technology and Applications XXXVI,* Vol. 7660, pp. 76600R-1–76600R-8, April 2010.

[30] H. Wada, T. Sone, H. Hata, Y. Nakaki, O. Kaneda, Y. Ohta, M. Ueno, and M. Kimata, "YBaCuO Uncooled Microbolometer IRFPA," *Proc. of SPIE, Infrared Technology and Applications XXVII,* Vol. 4369, pp. 297-304, April 2001.

[31] C. M. Travers, A. Jahanzeb, D. P. Butler, and Z. Çelik-Butler, "Fabrication of Semiconducting YBaCuO Surface-Micromachined Bolometer Arrays," *Journal of Microelectromechanical Systems,* Vol. 6, No. 3, pp. 271-276, September 1997.

[32] M. Y. Tanrıkulu, "An Uncooled Infrared Microbolometer Array Using Surface Micromachined MEMS Technology," *Ph.D. Dissertation,* Middle East Technical University, August 2007.

[33] F. Civitci, "Development of High Fill Factor Uncooled Infrared Detector Pixels," *M.Sc. Thesis*, Middle East Technical University, February 2008.

[34] S. U. Senveli, "Development Of High Thermal Performance Uncooled Infrared Detector Pixels With Enhanced Resistor Structures," *M.Sc. Thesis*, Middle East Technical University, February 2010.

[35] S. Eminoglu, "Uncooled Infrared Focal Plane Arrays with Integrated Readout Circuitry Using MEMS and Standard CMOS Technologies," *Ph.D. Dissertation*, Middle East Technical University, July 2003.

[36] C. Li, G. Skidmore, C. Howard, E. Clarke, and C. J. Han, "Advancement in 17 Micron Pixel Pitch Uncooled Focal Plane Arrays," *Proc. of SPIE Infrared Technology and Applications XXXV,* Vol. 7298, pp. 72980S-1–72980S-11, 2009.

[37] H.-K. Lee, J.-B. Yoon, E. Yoon, S.-B. Ju, Y.-J. Yong, W. Lee, and S.-G. Kim, "A high fill-factor infrared bolometer using micromachined multilevel electrothermal structures," *IEEE Trans. Electron Devices,* Vol. 46, pp. 1489–1491, 1999.

[38] C. Li, G. D. Skidmore, C.r Howard , C.J. Han, L. Wood , D. Peysha , E. Williams, C. Trujillo, J. Emmett, G. Robas, D. Jardine C-F. Wan, and Elwood Clarke, "Recent Development of Ultra Small Pixel Uncooled Focal Plane Arrays at DRS," *Proc. of SPIE, Infrared Technology and Applications XXXIII,* Vol. 6542, pp. 65421Y-1 65421Y-12, April 2007.

[39] D. Murphy, M. Ray, J. Wyles, J. Asbrock, C. Hewitt, R. Wyles, E. Gordon, T. Sessler, A. Kennedy, S. Baur, and D. Van Lue, "Performance Improvements for VOx Microbolometer FPAs," *Proc. of SPIE, Infrared Technology and Applications XXX,* Vol. 5406, pp. 531-540, April 2007.

[40] M. Tepegoz, "A Monolithic Readout Circuit for Large Format Uncooled Infrared Detector Focal Plane Arrays", *Ph.D. Dissertation*, Middle East Technical University, 2010.

[41] N. Eroglu, "Development Of High Performance Active Materials For Microbolometers," *M.Sc. Thesis*, Middle East Technical University, August 2011.

[42] Moon Sung, "Novel Infrared Absorbing Material Coupled Uncooled Microbolometer," *Proceedings of IEEE Sensors*, Vol. 2, pp. 658-660, 2004.

[43] M. Y.Tanrikulu, F. Civitci, and T. Akin, "A New Method to Estimate the Absorption Coefficient for Uncooled Infrared Detectors," Proc. of SPIE, Vol. 6940 (2008).

[44] D. M. Pozar, Microwave Engineering, Wiley, 1998.

[45] D. K. Cheng, Fundamentals *of Engineering Electromagnetics*, Addison-Wesley Reading, 1993.

[46] H. Bosman, Y. Y. Lau, and R. M. Gilgenbach, "Microwave Absorption on a Thin Film," *Applied Physics Letters*, Vol. 82, pp. 1353-1355, 2003.

[47] S. E. Kucuk, M. Y. Tanrikulu, and T. Akin, "A Detailed Analysis for the Absorption Coefficient of Multilevel Uncooled Infrared Detectors," *Proc. of SPIE Infrared Technology and Applications XXXVII,* Vol. 8012, pp. 80121R-1–80121R-8, April 2011

[48] A. H. Z. Ahmed and R. N. Tait, "Characterization of an Amorphous $Ge_xSi_{1-x}O_y$ Microbolometer for Thermal Imaging Applications," *IEEE Trans. on Electron Devices,* Vol. 52, pp. 1900-1906, 2005.

[49] E. Canga, "Development And Charecterization Of High TCR Material For Surface Micromachined Microbolometers", *M.Sc. Thesis*, Middle East Technical University, January 2010.

[50] F. N. Hooge, T. G. M. Kleinpenning, and L. K. J. Vandamme, "Experimental studies on 1/f noise," *Reports on Progress in. Physics*, Vol. 44, No. 5, 1981.

APPENDIX A

SUMMARY OF THE THERMAL SIMULATION RESULTS OF THE TYPE 1 PIXELS

Width of the Nitride Layer of the support Arm	Width of the Metal Layer of the Support Arm	Spacing Between the Arms	Thermal Conductance	Thermal Time Constant
0.5 µm	0.5 µm	0.6 µm	6.8 nW/K	51.7 ms
0.5 µm	0.5 µm	0.8 µm	8.1 nW/K	41.3 ms
0.5 µm	0.5 µm	1.0 µm	9.2 nW/K	35.4 ms
0.8 µm	0.8 µm	0.6 µm	13.8 nW/K	23.8 ms
0.8 µm	0.8 µm	0.8 µm	16.8 nW/K	19.3 ms
0.8 µm	0.8 µm	1.0 µm	18.7 nW/K	17.7 ms
1.0 µm	1.0 µm	0.6 µm	19.7 nW/K	16.2 ms
1.0 µm	1.0 µm	0.8 µm	23.1 nW/K	15.1 ms
1.0 µm	1.0 µm	1.0 µm	23.1 nW/K	14.8 ms